RESPONSE OF THE D0 CALORIMETER TO COSMIC RAY MUONS

by

Jonathan Kotcher

A dissertation submitted in partial fulfillment

of the requirements for the degree of

Doctor of Philosophy

Department of Physics

New York University

October, 1992

AC02-76CH03000

Approved:

Professor Peter Nemethy, Advisor

ABSTRACT

RESPONSE OF THE D0 CALORIMETER TO COSMIC RAY MUONS

Jonathan Kotcher

New York University

October, 1992

Advisor: Professor Peter Nemethy

The D0 Detector at the Fermi National Accelerator Laboratory is a large multi-purpose detector facility designed for the study of proton-antiproton collision products at the center-of-mass energy of 2 TeV. It consists of an inner tracking volume, hermetic uranium/liquid argon sampling calorimetry, and an outer 4π muon detector.

In preparation for our first collider run, the collaboration organized a Cosmic Ray Commissioning Run, which took place from February – May of 1991. This thesis is a detailed study of the response of the central calorimeter to cosmic ray muons as extracted from data collected during this run.

We have compared the shapes of the experimentally-obtained pulse height spectra to the Landau prediction for the ionization loss in a continuous thin absorber in the four electromagnetic and four hadronic layers of the calorimeter, and find good agreement after experimental effects are folded in.

We have also determined an absolute energy calibration using two independent methods: one which measures the response of the electronics to a known amount of charge injected at the preamplifiers, and one which uses a carry-over of the calibration from a beam test of central calorimeter modules. Both absolute energy conversion factors agree with one another, within their errors. The calibration determined from the test beam carry-over, relevant for use with collider physics data, has an error of 2.3%. We believe that, with further study, a final error of $\approx 1\%$ will

be achieved.

The theory-to-experiment comparison of the peaks (or most probable values) of the muon spectra was used to determine the layer-to-layer consistency of the muon signal. We find that the mean response in the 3 fine hadronic layers is $(12 \pm 2)\%$ higher than that in the 4 electromagnetic layers. These same comparisons have been used to verify the absolute energy conversion factors. The conversion factors work well for the electromagnetic sections.

This thesis is dedicated to my parents

ACKNOWLEDGEMENTS

I would first and foremost like to thank my advisor, Peter Nemethy, for his help and guidance not only with this thesis, but in other matters (both scientific and professional) as well. He has given me many valuable intellectual insights over the past 6 years, and his insistence on intellectual rigor has helped sharpen my thinking on numerous occasions. He has been an extremely helpful and trusted mentor.

I would also like to thank John Sculli for his help and support in general, but especially during the building of D0. I like to believe that the many long conversations we had concerning the building, testing, and installation of the calorimeter electronics are a key reason why the device works as well as it does. He was a pleasure to work with and learn from. Both he and Peter helped make my tenure as a student on D0 a personal as well as intellectual experience that I will fondly remember.

Thanks also go to both John and Qiang Zhu for their work on the data-taking for the test beam calibration carry-over. John's development of our approach to the calibration problem was an invaluable template, upon which all of the subsequent work was based.

The success of the Cosmic Ray Run, and in many respects the existence of this thesis, owe alot to Harry Weerts of Michigan State University. His concern and guidance helped make a cohesive unit out of the many disparate factions that participated in the run. I am certainly not alone in expressing my gratitude for his substantial contribution to D0.

Wlodek Guryn of Brookhaven National Laboratory was quite helpful during the calorimeter commissioning and cosmic ray data-taking – his frank and honest counsel during the past few years, in many matters, has also been much appreciated.

I would also like to thank James Kourlas, for his helpful conversations on the calorimeter electronics, and for his presence in general. And, of course, Kristine Dalman, for putting up with both me and LATEX in her efforts to make this thesis

a presentable finished product.

A thesis of this kind is inevitably based, to varying degrees, on the labors of many talented and industrious people. My thanks go to all of the D0 collaboration members who helped make it possible and, in particular, to our spokesperson, Paul Grannis of the State University of New York at Stony Brook.

TABLE OF CONTENTS

LIST OF FIGURES

LIST OF TABLES

CHAPTER I

INTRODUCTION

The D0 Detector, located at the Fermi National Accelerator Laboratory in Batavia, Illinois, is a large hermetic detector designed for the study of proton-antiproton collisions at the center-of-mass energy of 2 TeV. The physics for which it has been designed includes the study of jets, properties of the intermediate vector bosons, the search for the top quark, and searches for new and exotic phenomena in this heretofore unexplored energy regime.

In the late winter and spring of 1991, the collaboration organized a Cosmic Ray Commissioning Run, in which the response of a major portion of the detector to cosmic ray muons was studied. The primary goals of the run were to exercise the major detector elements in concert for the first time, and to study in detail the performance of the individual subdetectors. The run provided us with the opportunity to prepare for our first collider run, which began this spring.

The response of the central calorimeter to cosmic ray muons will be the focus of this thesis. The extent to which the calorimeter's performance can be characterized by its response to minimum-ionizing muons is a stringent test of the device: minimum-ionizing signals are at the very low end of the dynamic range of the system that has been designed, and exhibit a small signal-to-noise ratio. Extracting quantitative information from such signals presents a significant challenge which, in many respects, provides a benchmark against which we can evaluate the overall performance of the detector. Adequate performance is critical for achieving the goals of the D0 physics program.

After presenting an overview of the full detector and the physics for which it has been optimized, a discussion of the general principles of calorimetry is presented, along with the specific design features of the D0 calorimeters. A brief chapter on cosmic rays comes next, followed by a discussion of the theory of energy loss (by ionization) of charged particles in matter. Landau's theory of the energy loss in

thin absorbers [39] is expected to describe the visible energy loss of muons due to ionization in our calorimeter: one of the primary goals of this thesis is the test of this hypothesis.

The operation and performance of the calorimeter during the Cosmic Ray Run is discussed in Chapter VI, followed by a chapter describing the run itself: the data-taking, trigger, the detectors that were commissioned, and other issues. Our final criteria for event selection are discussed in Chapter VIII, along with our method of treating the data.

We obtained values for the conversion from ADC counts, our digitized unit of calorimeter readout, to energy deposited in the calorimeter, using two independent methods. Chapter IX discusses these methods, and presents the conversion factors so obtained. One of the important goals of the thesis is the verification of these calibration factors, which is obtained by comparison of the experimentally-determined muon pulse height distributions with those obtained from the Landau theory. These comparisons, along with the results of our calibration verification, are presented in Chapter X. We also present in that chapter our results on the layer-to-layer consistency of the muon signal throughout the calorimeter. Chapter XI summarizes our conclusions.

CHAPTER II

PHYSICS AT 2 TeV: THE D0 DETECTOR

The D0 Detector at the Fermi National Accelerator Laboratory is a multi-purpose facility designed for the study of products of high energy proton-antiproton collisions. The physics for which the detector has been optimized, along with the design features intended to enhance the detection of the relevant physics signatures, are described below.

Physics Goals

The discovery of the W and Z bosons at CERN in 1982 [12] was a striking verification of the Glashow-Weinberg-Salam model [11], the gauge theory unifying electromagnetism and weak interactions. In this theory, the W and Z mediate the charged- and neutral-current weak interactions, respectively, while the photon mediates the electromagnetic force. Exact local gauge invariance of the theory would require all 4 gauge bosons (W^{+-}, Z^o, γ) to be massless: experiment, however, has definitively eliminated this possibility. The process by which the W and Z are thought to acquire mass is the Higgs mechanism [14], in which a massive scalar boson (Higgs boson) is produced in association with the breaking of the electroweak symmetry. The photon remains massless in the theory. The four gauge bosons couple to the fundamental fermions, leptons and quarks. The left-handed fermions appear as doublets of weak isospin, while the right-handed ones appear as singlets. Right-handed neutrinos are assumed not to exist.

The most widely accepted theory of the strong interactions is Quantum Chromodynamics (QCD). The gluons are the gauge bosons of the theory and, due to the exact nature of the gauge symmetry, are massless. The basic unit of "charge" intrinsic to strong interactions is called color, which is carried by the gluons. (This is in contrast with the photon in electrodynamics, which does not carry electronic charge). There are 8 gluons (corresponding to the $3^2 - 1$ generators of the SU(3) symmetry of the theory), that couple to quarks, which are colored, and to each

other. The coupling "constant" of QCD, α_s, scales with distance, approaching zero at small distances (or, more relevant experimentally, high momentum transfers), a phenomenon known as asymptotic freedom. This allows the theory to be perturbatively expanded in this energy regime. Since free quarks and gluons have not been observed experimentally, it has been postulated that color is confined: that is, that the potential that describes the interaction between free gluons and/or free quarks increases monotonically with distance, at distances large compared to the scale parameter, Λ_{QCD}. Observable strongly-interacting particles are therefore thought to be colorless combinations of bound quarks and/or antiquarks. Both confinement and asymptotic freedom, as will be discussed later, have important consequences for high energy experiments.

The two above theories, taken together, form the Standard Model, a description of three of the four basic forces of nature (gravity is not included). It contains 19 free parameters (9 of which are the masses of the quarks and leptons) and predicts 37 fundamental particles, with the fermions appearing in repeated units called generations (see Table II.1). All particles but the tau neutrino, the top quark, and the Higgs boson have been seen experimentally.

The model has survived quite ably all tests to which it has been subjected. It is hoped that future collider measurements of Standard Model parameters will be made with increasingly high precision, which will enable more exacting tests of the model. Precision measurements should also guide the way toward viable extensions of the theory, if they are needed. Measurements of improved accuracy in the electroweak sector and large momentum-transfer tests of QCD are a major portion of the physics program for which D0 has been designed.

Searches for new particle states and phenomena, both predicted and unpredicted by theory, are the other significant part of the physics agenda for D0. The search for the top quark will be one of the more important parts of the experimental program at Fermilab during the next few years.

Table II.1

The Standard Model

(after [2])

fundamental fermions			
leptons			Q
$\begin{pmatrix} \nu_e \\ e \end{pmatrix}$	$\begin{pmatrix} \nu_\mu \\ \mu \end{pmatrix}$	$\begin{pmatrix} \nu_\tau \\ \tau \end{pmatrix}$	$\begin{pmatrix} 0 \\ -1 \end{pmatrix}$
quarks (times 3 colors)			
$\begin{pmatrix} u \\ d \end{pmatrix}$	$\begin{pmatrix} c \\ s \end{pmatrix}$	$\begin{pmatrix} t \\ b \end{pmatrix}$	$\begin{pmatrix} +\frac{2}{3} \\ -\frac{1}{3} \end{pmatrix}$

bosons

Interactions are mediated by bosons:

γ	photon	M = 0
$W^{\pm}$	IVB	M $\approx$ 80 $\frac{GeV}{c^2}$
Z^o	IVB	M $\approx$ 91 $\frac{GeV}{c^2}$
G	gluon (8 colored)	M = 0
Higgs	Higgs boson	M = ?

The discovery of the top quark would complete the last fermion doublet of weak isospin – its discovery would be a spectacular addition to the experimental evidence supporting the Standard Model. Current limits on its mass [4], derived from relations among the parameters in the model and using measured masses of the W and Z bosons as input, place it within reach of the Fermilab collider in the

next few years. A direct mass measurement of the top quark, in conjunction with high-precision W and Z mass measurements, could place very strict limits on the Higgs mass. It is likely that direct sighting of the Higgs, particularly if it is heavy ($2M_w <\sim M_{Higgs} < 1\ TeV$), will require machines of higher energy. Its predicted preferential coupling to heavier fermions and bosons, which are produced with relatively small cross-sections at Tevatron energies, result in small Higgs production cross-sections at existing machines. A top quark mass measurement at Fermilab would provide the mass window for future searches for the Higgs at the Superconducting Super Collider, should direct Higgs searches in Tevatron data yield a null result.

The model itself makes no prediction as to the number of generations of fermions that exist, helping to motivate the search for new heavy quarks and leptons. An outgrowth of the attempts to unify QCD and Electroweak Theory into gauge-invariant theories of higher symmetry (Grand Unification) is the introduction of new heavy vector bosons. One can search for higher-mass analogues of the W and Z, for example, assuming decay-modes similar to their lighter-mass cousins. Supersymmetry theories predict bosonic partners of fermions (and vice-versa), with some well-defined decay signatures. Technicolor introduces objects (leptoquarks) whose modes of decay may also be quite distinctive. Finally, new, unpredicted particles and interactions may manifest themselves in unexpected ways. It is hoped that their event topologies will approximate in some way those for which the detector has been optimized.

Physics Signatures

Much of the physics in the above processes is most readily extracted from the background by consideration of events containing one or more of a few basic characteristics. The momentum component of collision products in the direction transverse to the incoming $\bar{p}p$ beams, called transverse momentum (P_t), is the major kinematic variable of interest. Much of the analysis of $\bar{p}p$ collider data is restricted to reaction products of high-P_t primarily for the following two reasons:

(1) The forward (or beam) direction is dominated by leftover debris from hadronic collisions, generally containing little interesting new physics. These backgrounds tend to obscure the processes of value;

(2) The presence of neutrinos and other non-interacting particles, which are important physics signatures, can only be inferred from the overall event momentum – they are "seen" as an imbalance in missing momentum. In practice, much of the event momentum is invariably lost along the beam directions, and hence escapes undetected. Considering only the momentum component transverse to the beam axis greatly reduces the importance of fluctuations in this undetected momentum.

Much of the potentially interesting physics lies in events containing one or more of the following: high-P_t charged leptons (predominantly electrons and muons), photons, jets of hadrons, and large missing transverse momentum (MP_t). A few of the underlying processes are described below.

The parton model [9] was created to explain the point-like constituents of the proton, which were seen by experiments [10]. The partons are now generally equated with the quarks, antiquarks, and gluons of QCD. Large angle scattering of two incident partons, each containing a large fraction of their parent hadron's longitudinal momentum, results in two outgoing partons of high-P_t that are back-to-back in the center-of-momentum frame of the incident partons. At distances large compared to the hadron size, the two high-P_t partons undergo hadronization, in which the confining properties of the color force induce the production of colorless bound states of hadrons, with momentum components primarily in the direction of the parent parton. The result is two well-collimated jets of hadrons of high-P_t, which contain "memory" of the original direction of the parent parton (the jet axis). Jets of high-P_t are signatures of a collision of large q^2 (momentum transfer), where a description of the interaction between the parent partons within the framework of perturbative QCD is feasible.

The study of jets has become a major portion of the physics menu at hadron colliders. The dijet invariant mass distribution can reveal new particle states, or reveal properties of known states (as, for instance, in the decay of the W or Z bosons to quark-antiquark pairs). The ratio of the cross-section of 2- to 3-jet events allows for a quantitative measure of $\alpha_s(q^2)$, as does the ratio of W + 1-jet to W + no-jets events. The high center-of-mass energy at the Tevatron will allow for studies of the scaling of α_s at higher q^2 than ever before. The spectra of inclusive 1- and 2-jet cross-sections as a function of P_t, as measured at the CERN $Sp\bar{p}S$ [8] at center-of-mass energies of 540 and 630 GeV, give good agreement with lowest-order QCD calculations. Quark compositeness (or substructure) would imply a deviation from the expected inclusive jet cross-section (usually as a function of P_t). The higher Tevatron energy will allow an extension of this probe into underlying parton structure. As some (hopefully predictable) combination of jets is likely to accompany new particle states at higher energies, the quantitative understanding and characterization of jet properties is extremely important.

Another means of studying the scaling of α_s is through direct photon production. Cross-section calculations have been done to next-to-leading order, allowing comparison at this level to measurements. Unlike jets, the analysis of direct photon data is not complicated by uncertainties in fragmentation functions. (Fragmentation functions are empirically obtained functions describing the hadronization process). The cross-section, however, is significantly smaller (it scales with the ratio of α_{EM} to α_s), and the backgrounds can be difficult to deal with. In particular, π^0's decaying to 2 photons with a small opening angle can mimic the direct photon signal.

Precision measurements of W and Z properties (including their masses, widths, and distributions in transverse momentum) are made predominantly through their decays to electrons or positrons:

$$\bar{p}p \longrightarrow W - X$$

$$\downarrow$$

$$e, \nu$$

$$\bar{p}p \longrightarrow Z^o + X$$

$$\downarrow$$

$$e, e$$

where:

W, Z^o = boson produced from quark/antiquark collision;

e = electron or positron produced from boson decay;

ν = (anti)-neutrino produced in W decay;

X = low-P_t fragments from spectator quark interactions in the underlying event.

The Z mass is derived directly from the invariant mass of the 2 electrons. The transverse mass is the distribution from which the mass of the W is determined. and is given by:

$$M_T^2 = 2P_t^e P_t^\nu (1 - cos\theta_{e\nu})$$

where:

M_T = transverse mass of the W;

P_t^e = transverse momentum of the electron:

P_t^ν = transverse momentum of the neutrino:

$\theta_{e\nu}$ = the angle between the electron and the neutrino in the plane transverse to the incoming beam.

The P_t of the charged lepton is measured directly, while the P_t of the neutrino is inferred from the measurement of the electron P_t and the remaining P_t in the event:

$$P_t^{\nu} = -(P_t^{e} + P_t^{X}) = -(\textit{visible}\ P_t).$$

It is clear from both of these cases that the overall electron energy resolution is of major importance in measuring the boson masses. In the case of the W, the resolution in MP_t also contributes significantly. The hadronic energy resolution, on which the resolution in MP_t depends, is also important, especially in the determination of the W transverse momentum. Measurements of W and Z properties of increasing precision during the coming decade will help to provide more exacting tests of the Standard Model.

Constraints between various Standard Model parameters allow for the determination of other quantities of interest from vector boson mass measurements. For example, using the renormalization scheme of Sirlin [13]:

$$sin^2\theta_w \equiv 1 - (M_w/M_z)^2$$

where:

θ_w = the Weinberg angle;
M_w = mass of the W;
M_z = mass of the Z^o.

The current value for $sin^2\theta_w$ derived from world-average W and Z mass measurements obtained from hadron collider data is 0.2275 ± 0.0052 [4]. The top quark mass is now constrained, through measurements of the W (again, obtained from hadron collider data) and Z masses (obtained from the LEP experiments at CERN) to $128^{+40}_{-48}\ \frac{GeV}{c^2}$ for a 100 $\frac{GeV}{c^2}$ mass Higgs [4].

Having been shown by direct experimental evidence to have a mass greater than that of the W ($M_{top} \geq 89\ \frac{GeV}{c^2}$ at the 95% confidence level [5]), the top quark is most accessible through the channel:

$$q\bar{q} \longrightarrow t\bar{t} \longrightarrow W^+ + W^- + b\bar{b}$$

Since the b-quarks result in jets (of generally low P_t), the final states resulting from $t\bar{t}$ production that offer the most promise for top quark detection are those wherein one or both W's decay to leptons:

$$W^+, W^-, b, \bar{b} \longrightarrow l, \nu + \text{jets} \quad (1) \quad (\text{branching ratio} \approx 30\%)$$
$$\longrightarrow l,\ l', \nu, \bar{\nu}' + \text{jets} \quad (2) \quad (\text{branching ratio} \approx 5\%).$$

In both cases, one or more high-P_t charged leptons, missing energy, and jets are the outstanding detectable event components. Process (2) is likely to hold more promise, despite its reduced branching ratio, as the backgrounds are less difficult to deal with. In particular, process (1) has to compete with the background QCD process:

$$p\bar{p} \longrightarrow W + \text{jets}$$
$$\downarrow$$
$$l, \nu$$

For a top mass not very much higher than the mass of the W, the P_t spectrum of the jets produced in the two cases is appreciably different (jets resulting from top production are, on average, of higher P_t than those produced in the above case), and should allow for an appropriate cut to increase the signal-to-noise. Good energy resolution to aid in jet-P_t measurements will be of benefit here. Two primary sources of background for the dilepton channel are:

$$(1)\quad p\bar{p} \longrightarrow Z^o + \text{jets}$$

with either

$$\text{(a)}\ \ Z^o \longrightarrow e, e \text{ or } \mu, \mu$$

or

$$\text{(b)}\ \ Z^o \longrightarrow \tau, \tau \longrightarrow e, \mu + \text{neutrinos}$$

and

$$\text{(2)}\ \ p\bar{p} \longrightarrow W^+ + W^- + \text{jets},$$

with both W's decaying leptonically. In (1a), a cut on the invariant mass of the dilepton pair reduces the background significantly. Studies (limited to a top mass $\leq 2M_w$) have suggested [7] that process (1b) is the primary source of background for a final top state containing a high-P_t electron and a high-P_t muon. Monte carlo simulations indicate [7] that an appropriate cut on the azimuthal angle between the leptons enhances the signal-to-noise considerably. It is this distinctive e, μ channel that is believed to hold the most promise for the discovery of the top quark at the Tevatron. Superior lepton identification and coverage and good energy resolution for jet-P_t and MP_t measurements will clearly help in searching for the top quark in all of the above decay channels.

The D0 Detector

The D0 Detector consists of three major subdetectors: central tracking, calorimetry, and the muon system. It stresses good electron identification, 4π muon coverage, and hermetic highly-segmented calorimetry with excellent energy resolution. The central tracking detectors provide tracking information on charged particles produced from the collisions. Precision measurements of both electromagnetic and hadronic energy are provided by the calorimeters, while the outlying muon system provides momentum measurements and additional tracking information on the muons produced.

The detector contains no central magnetic field. The philosophy is that, at Tevatron energies, direct calorimetric measurements of jet and lepton energies is

more important than momentum determination obtained from track curvature. An emphasis on calorimetric measurements treats neutral and charged particles (at the core of jets, for instance) in very much the same way. A central magnetic field would require a more complicated, and larger, tracking system, hence expanding the overall dimensions (and cost) of the detector. An inner magnetic system also places a large amount of material between the collision region and the calorimeter, degrading calorimeter resolution and performance. Physics expectations dictate the importance of good measurements of MP_t and overall event energy at the Tevatron – D0 has opted for a compact, non-magnetic design in order to accomplish these goals within reasonable size and cost constraints. Figure (1) shows a cutaway drawing of the detector. The components of the various subdetectors are described below.

Coordinate Systems

There are a number of relevant geometrical variables and coordinate systems used by the different subdetectors. The incident proton-antiproton beams travel along the Z-axis, with +Z pointing south. +X points due east, and the +Y axis points vertically upward. The r and ϕ coordinates are analogous to those in cylindrical coordinates:

r = perpendicular distance to the beam axis;

ϕ = the angle (measured in the clockwise direction when looking south along the Z-axis) with respect to the +X axis ($0 - 2\pi$).

The angle θ is the usual polar angle, subtending $0 - \pi$. The pseudorapidity, given the symbol η, has become a fundamental variable in high-energy physics. Its utility is related to the fact that the charged-particle multiplicity distribution in hadronic collisions, as a function of η, is flat for a large η range. It is defined by:

$$\eta = -ln\left[tan\left(\frac{\theta}{2}\right)\right].$$

The most commonly used set of variables is (r, ϕ, η). The others above are presented for completeness.

Central Tracking

The D0 central tracking system consists of an inner vertex chamber, a transition radiation detector, forward-backward drift chambers, and a central drift chamber (see Figure (2)). References [19-22] contain more detailed descriptions of the different D0 tracking subdetectors. Immediately surrounding the beampipe is the vertex chamber. It was designed for the precise spatial measurement of charged particle tracks that occur close to the intersection region, with the goal of being able to reconstruct both primary and secondary decay vertices. (Primary vertices are important for overall event reconstruction; secondary vertices aid in the identification of heavy quark mesons and leptons that decay some distance from the interaction point.) The chamber also provides $\frac{dE}{dx}$ measurements of charged particle tracks, which enables one to distinguish unopened e^+e^- pairs (which result from photon conversions) from single electrons. Beam tests of a prototype in 1987 gave 50μm spatial resolution at 8 mm drift distance, and two-track discrimination of better than 90% for track separations exceeding 700μm [20].

D0 employs a transition radiation detector (TRD), located just outside the vertex detector, in order to aid in electron identification. The detector measures the energies of X-rays that are produced as charged particles cross the boundary between materials of two different dielectric constants. The intensity of the X-rays produced is proportional to γ, the Lorentz factor, of the incident particle. Particles of different mass (electrons and charged pions, for example) but of the same momentum will have different Lorentz factors, providing the basis for particle identification. The X-rays are produced in radially concentric sets of polypropylene foils, and create photoelectrons in conversion zones of the detector which are filled with xenon gas. The resulting ionization charge drifts radially outward to a proportional wire chamber region, where it is amplified and collected. The TRD provides excellent electron identification to $\eta \approx 1.0$. A 50:1 pion rejection factor at 90% electron detection

efficiency was measured in tests of the D0 TRD at Saclay in France [19].

The central drift chamber (CDC) lies in the next radial region (51.8 to 71.9 cm). It provides further tracking information, and offers additional $\frac{dE}{dx}$ measurements to aid in the identification of unopened e^+e^- pairs. Photons that convert prior to the TRD (which will still be identified as electrons therein) will be identified by $\frac{dE}{dx}$ measurements and/or the lack of a charged particle track in the vertex chamber. Those that convert in the TRD, but pass its electron selection criteria, will be identified by both the lack of a track in the vertex chamber, and $\frac{dE}{dx}$ measurements of the e^+e^- pair in the central drift chamber. π^o's are another copious source of background, as they can mimic electrons through their rapid decay to 2 photons. The tracking system will help reject the background from this source as well.

The CDC consists of sets of 32 drift cells in each of 4 concentric layers, with each cell containing 7 radially displaced sense wires that run the length of the chamber. The $r-\phi$ coordinates are obtained from knowledge of the wire position and measurement of the drift time of the signal produced on the sense wire by ionization of the drift gas (an argon/methane/carbon-dioxide mixture). The axial position is obtained from signals induced on delay lines, located at the inner- and outermost radius of each drift cell. Time information at both ends of each delay line gives a measurement of the axial coordinate to 3 mm. Each of the 4 layers is rotated 1/2 of a cell width from that of its neighboring layer, in order to resolve the left-right ambiguity within a cell, enhance two-track separation, and aid in calibration. Figure (3) shows an end-on view of a section of the CDC.

The characteristics and design goals of the forward/backward chambers are similar to that of the central drift chamber. They consist of a phi module, which measures the $r-\phi$ coordinate using wires that run axially, situated between two theta chambers, which measure the η coordinate. The forward/backward drift chambers, together with the central drift chamber, give full tracking and $\frac{dE}{dx}$ information to $\eta \approx 3.5$.

D0 Calorimetry

The heart of D0 is uranium/liquid argon sampling calorimetry for the measurement of incident particle and jet energies. Particles incident on a material of high atomic number (high-Z) initiate a cascade or "shower" of low energy secondary particles. In sampling calorimetry, layers of high-Z absorber are alternated with active material, where the energy of these secondaries is measured via charge collected from the resulting ionization of the active medium. The D0 calorimetry is housed in 3 separate cryostats: one central (CC) and two end (EC) calorimeters. Each calorimeter is subdivided into three sections: the electromagnetic, fine hadronic, and coarse (or outer) hadronic sections. Figure (4) shows a cutaway view of the D0 calorimeters.

The physics at D0 calls for calorimetry with good energy resolution, a high degree of segmentation to enhance electron identification and resolve jets, and hermeticity for good missing transverse momentum measurements to allow for the "detection" of neutrinos and other non-interacting particles. Fine longitudinal and lateral segmentation helps to distinguish electrons from hadrons on the basis of the shapes and development of the showers they create: electron showers develop earlier, and are more finely collimated, than hadronic ones. Such segmentation also helps distinguish single photons from overlapping pairs resulting from meson decay. Uranium/liquid argon calorimetry for D0 has been chosen with the above goals in mind. It is hermetic (full coverage to 2 degrees of the beam axis), easily segmented, and homogeneous in response (offering signal uniformity and relative ease of calibration). The fact that it is operated as a unit-gain ionization chamber makes its response stable over time. It offers excellent energy resolution, and it is approximately compensating (response to electrons = response to hadrons), a crucial factor in calorimetric measurements. The high density of uranium also allows for a compact detector that will contain shower energy while reducing cost.

Beam tests of calorimeter modules performed in 1987 at the Fermi National Accelerator Laboratory [29] found the response of the CC electromagnetic modules

to be linear to better than 1% over the energy range from 10 to 150 GeV. The deviation from linearity of the EC middle hadronic modules in the same energy range was less than 2%. The average $\frac{e}{\pi}$ ratio (response to electrons/response to pions) was measured to be 1.03, and varied from 1.08 at 10 GeV to 1.00 at 150 GeV. The measured energy resolution was $\frac{16\%}{\sqrt{E}}$ for the electromagnetic modules, and $\frac{49\%}{\sqrt{E}}$ for the hadronic. Further details about the calorimetry can be found in Chapters III and VI.

Muon System

Muons do not shower and, as a result, are very penetrating and deposit little energy in matter. Because muons deposit a small fraction of their energy in the calorimeter, sufficiently accurate measurements of overall event P_t must include a non-calorimetric determination of the muon P_t. A separate system to provide both muon momentum and position information, situated furthest from the interaction region, is part of the D0 design. Some combination of a reconstructed track in the outer muon system, associated minimum-ionizing energy deposition in the calorimeters, and correlation of muon tracking information with that from the central tracking detectors, is the experimental signature for muon production.

The D0 muon system gives full muon coverage down to 5 degrees from the beam axis. It consists of sets of proportional drift tubes (PDT's) both inside and outside either a central or 2 end iron-filled toroidal magnets, magnetized to $\approx$ 2 Tesla. The azimuthal field causes deflections in the $r-Z$ plane, which are measured via reconstruction of the tracking information (and hence the bend angle) from both the 1 inner and 2 outer chambers. The muon exit direction is obtained from the 2 outer chambers (which are 1 to 2 meters apart), and information from both the primary interaction vertex and the central drift chamber aids in determination of the entry direction. The Z-information of the track is obtained from induced signals on chevron-shaped vernier pads that are capacitively-coupled to the PDT wires. Cosmic ray tests of proportional drift chambers gave drift time resolutions of $\approx$ 200 μm, and resolution from the vernier pad information in Z of $\approx$ 3 mm. The

momentum resolution, for muon P_t below about 300 $\frac{GeV}{c}$, is limited by Coulomb scattering in the toroid, and is approximately given by $\frac{\delta p}{p} \approx 18\%$ [17].

The full thickness of the D0 detector (toroids plus calorimeters) is about 13.3 λ_{INT} at 90 degrees and 18 λ_{INT} at 11 degrees, which helps eliminate punchthrough of hadronic shower energy and its possibility of simulating muon tracks. (λ_{INT}, the nuclear interaction length, sets the scale for the longitudinal development of hadronic showers). The number of interaction lengths required to contain 99% of the shower energy increases only slightly with energy, and approximately 9 λ_{INT} are required to contain 99% of the energy deposited by 210 GeV pions [26]. While resolving electrons within jets of high multiplicity can be difficult, the thickness of the D0 toroids has been designed to enhance the detection of muons in this environment. This feature, combined with its hermeticity, will allow D0 to exploit as fully as possible the complementary characteristics of this other important lepton channel.

CHAPTER III

CALORIMETRY IN HIGH ENERGY PHYSICS: THE D0 CALORIMETER

With the increase of available center-of-mass energy in high energy collisions came the capability to probe deeper into particle substructure. Much of the emphasis in high-energy experiments has shifted from the detection of individual particles to the accurate measurement of overall event energy characteristics (e.g., missing transverse energy and momentum, total event energy, transverse momentum), quark-antiquark interactions, and the resulting event topologies (jets, etc.), have become the processes of interest. Calorimetry provides a technically viable means of performing such measurements, with intrinsic characteristics (resolution, size requirements, triggering capability) that are well-suited to the goals of high energy experiments.

Calorimetric Processes

A particle entering a block of matter loses energy by a number of different processes. The overall evolution of the energy loss can in most cases be described by a cascade of lower energy secondary particles, of transverse and longitudinal dimensions and other characteristics that are now reasonably well understood. The calorimetric technique involves measuring the energy of these secondaries, and inferring the energy of the incident particle(s) that created them. In essence, calorimeters are used in high energy physics to contain, localize, and measure the energies of particles and jets.

The "showers" can be separated into 2 distinct types: electromagnetic and hadronic, named for the primary particles that initiate them. Each is discussed separately below. The energy loss of minimum ionizing particles (which do not shower) will be discussed in Chapter V.

Electromagnetic Showers

A qualitative description of electromagnetic shower development that adequately

illustrates many of its essential quantitative features has been presented by Heitler [25] (see Figure (5)). A high-energy ($\gtrsim$ GeV) electron of energy E_0 incident on a material will, after traversing ≈ 1 radiation length (to be defined shortly), radiate a photon, resulting in an electron and a photon each of average energy $\frac{E_0}{2}$. In the second radiation length, the photon produces an e^+e^- pair (each of energy $\frac{E_0}{4}$), while the electron radiates another photon. After 2 radiation lengths, then, there exist 4 particles – 2 electrons, 1 positron, and 1 photon – each containing approximately $\frac{1}{4}$ of the energy of the original (primary) electron. (Electrons and positrons are treated on an equal footing with respect to energy loss in the model).

The electromagnetic cascade develops in such a manner until the mean energy of the secondary particles reaches the critical energy ϵ, which is the point where particle multiplication no longer occurs. Energy loss after this point is dominated by ionization losses (for electrons and positrons) and Compton scattering and the photoelectric effect (for photons). For energies above the critical energy, electrons and positrons lose energy predominantly through the creation of a photon, and photons lose energy through the creation of 2 charged particles (e^+e^- pair). Below the critical energy, electrons produce no new photons, and photons create a new electron, concomitantly being absorbed (photoelectric effect) or scattered (Compton scattering). The electron produced via these soft photon processes are below the critical energy, and are not energetic enough to cascade further. At the critical energy, therefore, the number of particles in the shower has reached its maximum.

The model assumes that electrons and positrons above the critical energy lose their energy through radiation only, and by ionization only for energies below the critical energy. Photons above the critical energy are assumed to lose energy through pair production only, and by Compton scattering and the photoelectric effect below the critical energy.

A simple mathematical description of electromagnetic shower development can be deduced from the model. The number of particles present in the shower after t

radiation lengths, $N(t)$, increases exponentially with t:

$$N(t) = 2^t = e^{t(ln2)}. \tag{1}$$

Their average energy is:

$$E_{av}(t) = \frac{E_0}{2^t}. \tag{2}$$

Solving for t in equation (2) gives the depth at which the average energy of a shower particle is equal to some energy E':

$$t(E') = \frac{ln\left(\frac{E_0}{E'}\right)}{ln2}. \tag{3}$$

The shower maximum occurs at $E' = \epsilon$:

$$t_{max}(\epsilon) \propto ln\left(\frac{E_0}{\epsilon}\right), \tag{4}$$

implying that the depth in radiation lengths of the maximum of the shower in a given material goes like the logarithm of the incident energy. This can be used to crudely set the scale for the increase of electromagnetic calorimeter size that would be necessary to contain shower energy, with increasing energy of the primary particles.

The number of particles in the shower at the critical energy is proportional to the incident energy:

$$N(t_{max}) = e^{t_{max}ln2} = \frac{E_0}{\epsilon}. \tag{5}$$

Since in this model electrons, positrons, and photons are present in equal numbers at energies above the critical energy [25], the integrated number of charged particle tracks that have been present in the material up to the point when the average particle energy is equal to the critical energy is given by:

$$N_{tot} = \frac{2}{3}\int_0^{t_{max}} N(t)dt. \tag{6}$$

For $E_0 \gg \epsilon$ (which holds for collider energies), this beomes:

$$N_{tot} = \frac{2E_0}{3\epsilon ln2}. \tag{7}$$

The total track length, then, is proportional to the incident energy. Since it is assumed in the model that no more multiplication occurs at particle energies below the critical energy, N_{tot} is the total number of tracks produced by the cascade. (It is important to note that all of the above presumes a homogeneous medium.) If we assume that the charged particle tracks produce the measurable signal by ionization of the medium, the statistical error in that measurement is equal to $\sqrt{\frac{N_{tot}}{2}}$ (the factor of $\sqrt{2}$ arises from the fact that the electrons and positrons are produced in pairs, making the statistical fluctuations of their numbers correlated). It follows that:

$$\sqrt{\frac{N_{tot}}{2}} \propto \sqrt{E_0} \tag{8}$$

and the resolution becomes:

$$\frac{\sigma(E)}{E} = \frac{\sqrt{\frac{N_{tot}}{2}}}{N_{tot}} = \frac{\kappa}{\sqrt{E_0}}, \tag{9}$$

where

$$\kappa = \sqrt{\frac{3(ln2)\epsilon}{4}}. \tag{10}$$

Equation (9) contains a fundamental feature of calorimetric measurements of electromagnetic energy: the contribution to the resolution that results from the statistically-governed fluctuations in the number of charged particle tracks is proportional to $\frac{1}{\sqrt{E_0}}$. For properly designed calorimeters, therefore, the fractional resolution can be expected to improve with increasing energy. Note also (from Equation (7)) that the measurable signal is linear in the incident energy; this is another significant feature of calorimetric measurements. These characteristics have helped make calorimeters the detector of choice at colliders, where the importance of energy determinations and associated resolutions is of paramount importance. The constant

κ given by Equation (10) is proportional to $\sqrt{\epsilon}$, implying that lowering the critical energy can help improve the resolution. (This is not surprising, as Equation (7) says that lowering the critical energy will, for a given incident energy, result in the increase of the total number of tracks produced. The resolution will, therefore, improve.) For many homogeneous calorimeters, where the number of charged-particle tracks is large, the statistical fluctuations in their numbers is not the dominant factor in determining the energy resolution. Energy resolutions of $\approx \frac{1\%}{\sqrt{E_0}}$ have been obtained, for example, in homogeneous calorimeters made of bismuth germanium oxide crystal (BGO) [28]. In sampling calorimetry, however, where passive (high-Z absorber) layers are interleaved with active (lower-Z readout) material, the smaller number of tracks detected in the readout layers is often the factor that dominates the energy resolution. More will be said about this below.

Electromagnetic shower development depends primarily on the electron density, and hence Z, of the material. Many of its features can therefore be described, with the proper choice of units, in an approximately material-independent way. The radiation length, defined as the amount of material that a high-energy ($\gtrsim$ GeV) electron traverses in losing 63.2% ($1 - \frac{1}{e}$) of its energy to radiation, allows for such a description, and is given approximately by:

$$X_0 \approx \frac{180A}{Z^2} \left(\frac{g}{cm^2}\right). \tag{11}$$

The critical energy, described above and defined as the energy at which electrons lose equal amounts of energy to ionization and bremsstrahlung, is given approximately by:

$$\epsilon \approx \frac{550}{Z} \text{ (MeV)}. \tag{12}$$

The lateral spread of an electromagnetic shower is caused by the finite angle of emission of bremsstrahlung photons and by multiple scattering of the electrons by the absorber. In the latter stages of shower development, the radius of the shower scales with the Moliere radius, defined as the average lateral deflection of an electron

Material	Z	X_0(cm)	ϵ(Mev)	ρ_m(cm)	$\frac{\lambda_I N T}{X_0}$
Al	13	10.65	42	5.4	3.66
Cu	29	1.52	19	1.7	10.69
Pb	82	0.49	7	1.6	42.74
Ur	92	0.27	6	1.0	49.83

Table III.1: Shower parameters for aluminum, copper, lead, and uranium.

of energy ϵ after it traverses one radiation length. An approximate mathematical formula is given by:

$$\rho_m = \frac{21 X_0}{\epsilon} \approx \frac{7A}{Z} \left(\frac{g}{cm^2} \right). \tag{13}$$

Approximately 90 to 95% of the shower energy is contained in 2.5 ρ_m. Table III.1 shows a list of important shower parameters for 4 different materials, as obtained from Equations (11−13) and (22).

The design of a calorimeter allows for a choice among many different materials. Because the low- and high-energy processes that contribute to electromagnetic shower development are treated as two quite distinct regimes with very different characteristics, the Z-dependence (which is the most relevant variable) of these processes is of both practical and theoretical interest. Figure (6) shows the results of calculations of the cross-sections for (or energy loss by) various mechanisms, as a function of incident energy for three different materials, for photons and electrons, respectively. The critical energy for electrons and the energy for photons at which the losses due to Compton scattering dominate those from pair production are seen to roughly scale as $\frac{1}{Z}$. Figure (7) shows the longitudinal development of 10 GeV electromagnetic showers in 3 different materials. The shift of the maximum energy loss to higher radiation lengths for materials of larger Z is because multiplication continues to lower energies; the slower decay for high-Z media is because lower energy electrons still radiate. Both effects are attributable to the lowering of the critical energy with increasing Z, as seen in Figure (6) and Equation (12). Figure (6) also

illustrates the Z-dependence of the contribution from the photoelectric effect, an important reaction in shower development. In carbon, the process plays practically no role at all, while in uranium it dominates at photon energies below ≈ 0.7 MeV. The Z^5 cross-section dependence of the photoelectric effect, and its dominance at the highly-populated low photon energies, has important consequences for sampling calorimetry, as will be discussed later.

Readout substances, in which charged-particle tracks are detected, are generally materials of low Z. A calorimeter designed to contain showers of a given energy and composed entirely of such a material would have to be prohibitively large in order to contain all of the shower energy. (Such shower containment is important, as fluctuations in the measured energy introduced by incomplete containment can significantly degrade the resolution.) A pure liquid argon calorimeter of a depth of 25 radiation lengths (which gives $\approx 95\%$ containment of electron showers at Tevatron energies) would require a depth of about 3.5 meters. This is far too large, and quite costly.

Sampling calorimetry, which alternates high-Z absorber material (in which showers develop) with lower-Z readout material (in which the charged-particle tracks produce measurable signal through ionization of the readout medium), helps to restrict the longitudinal dimension of the shower. The size of the calorimeter is thus held in check, but at a price: only a portion of the energy is actually sampled, since the energy lost by shower particles as they traverse the absorber is invisible. The mean energy of shower particles at the shower maximum (see Equations (2–4)) is equal to the critical energy, which is ≈ 6 MeV for uranium. The range of a 6 MeV electron in uranium is ≈ 3 mm. Thus, for uranium absorber layers of $\lesssim 3$ mm, the charged shower particles of energy ϵ can be expected to escape the absorber layers for detection in the active material. Such considerations are important in detector design.

The ultimate quantity of interest is the total energy lost by the incident particle as it traverses the calorimeter, which in most cases is equal to the incident energy. In

order to correct for the energy lost in the absorber plates, (i.e., to convert measured readout to total energy loss), the sampling fraction is defined:

$$SF = \frac{< \frac{dE}{dx} >^{mip}_{active} \cdot dx_{active}}{< \frac{dE}{dx} >^{mip}_{absorber} \cdot dx_{absorber} + < \frac{dE}{dx} >^{mip}_{active} \cdot dx_{active}} \qquad (14)$$

where $< \frac{dE}{dx} >^{mip}$ is the mean $\frac{dE}{dx}$ value for a minimum ionizing particle in the absorber or active layer, and dx is the thickness of material. This number gives the fraction of the energy deposited in the active layers by a minimum ionizing particle traversing the calorimeter. Dividing a given signal (obtained from the readout of the charge collected from the ionization of the active material) by the sampling fraction gives the amount of total energy (i.e., energy lost in both the absorber and readout layers) that a minimum ionizing particle, producing an identical signal in the readout layers, would lose in the calorimeter. Since the large majority of particles that ionize the active medium in the electromagnetic cascade are soft and hence minimum ionizing (in fact, the Heitler model assumes that all energy deposited is minimum ionizing), this number applies, with a modification, to electromagnetic showers as well.

The low-energy regime is where the photoelectric effect begins to dominate the photon cross-section in high-Z materials (see Figure (6)). The cross-section for the photoelectric effect goes as $\approx Z^5$, implying that, for absorbers of very high Z, the soft photon component will interact almost exclusively in the absorber. The electrons produced are generally of insufficient energy to escape the passive layer, and hence are not sampled. This effect begins to dominate the energy resolution in practical electromagnetic sampling calorimeters: for materials of increasing Z, the degradation in energy resolution due to the behavior of the soft photon component dominates the improvement in the resolution resulting from the increase in the total number of tracks produced (i.e., the lowering of the critical energy). One would therefore expect the energy resolution to be worse in calorimeters of increasing Z, for active layers of the same thickness and material. This has in practice been found to be true [26].

Monte carlo simulations have shown that for 10 GeV electron showers in either uranium or lead, approximately 40% of the detectable energy is deposited by particles of energy below 1 MeV [26]. If one were to build a calorimeter capable of containing both an electron and a minimum-ionizing muon, measure the response to each at equal energies, and correct for the sampling fraction, the response for electrons would, in general, be lower. This is because of the large fraction of soft tracks in electron showers that are not energetic enough to emerge from the absorber plates, and so do not contribute to the signal. Minimum ionizing particles, which do not shower, deposit all of their visible energy by ionization in the readout gap; there is little or no contribution to the signal that results from reactions (or showering) in the absorber plates. In general, then, the fraction of the visible energy seen in electron showers is smaller than that fraction seen for a minimum-ionizing particle; the ratio of these two fractions is known as the $\frac{e}{mip}$ ratio.[1] A typical value, obtained from monte carlo simulations [31], is:

$$\frac{e}{mip} \approx 0.65. \tag{15}$$

Analysis of the muon response in a detector calibrated with electrons requires careful application of this number. The use of the $\frac{e}{mip}$ ratio in this study will be discussed in a later chapter.

For the D0 calorimeter, the sampling fraction in the electromagnetic section is $\approx$ 12%, and the critical energy for uranium is $\approx$ 6 MeV. Altering Equation (7) to apply to sampling calorimeters gives:

$$N_{tot} = \frac{2E_0}{3\epsilon ln2} \cdot \mathrm{SF} \tag{16}$$

and the resolution becomes:

$$\frac{\sigma(E)}{E} = \frac{\kappa'}{\sqrt{E_0}}, \tag{17}$$

[1] We note the distinction between the energy-dependent quantity $\frac{e}{\mu}$, and the idealized, energy-independent quantity $\frac{e}{mip}$. For a more complete discussion of this, see [31].

where

$$\kappa' = \frac{\kappa}{\sqrt{SF}}. \tag{18}$$

Using the above numbers, we obtain:

$$\frac{\sigma(E)}{E} = \frac{16.1\%}{\sqrt{E_0}} \tag{19}$$

where E_0 is expressed in GeV. This is to be compared to the resolution for electrons measured in portions of the D0 electromagnetic calorimeter in the 1987 test beam at Fermilab [29]:

$$\frac{\sigma(E)}{E} = \frac{(16.2 \pm 1.1)\%}{\sqrt{E_0}}. \tag{20}$$

The predictions derived from this semi-quantitative model agree quite well with the measurements.

Hadronic Showers

The basic features of hadronic calorimetry are similar to those of electromagnetic calorimetry, but the larger number of processes contributing to the development of the shower result in a more complicated description. To date, no monte carlo exists that completely and successfully describes hadronic shower development.

A high-energy hadron incident on a block of material will eventually interact with a nucleus of the medium via the strong interaction. The most probable result is the production of mesons ($\pi^{\pm}, \pi^{0}, K^{\pm}, K^{0}, \eta$), with an excited nucleus produced in the process. The nucleus releases its energy by the production of nucleons, photons, and mesons, in addition to losing some of its kinetic energy via ionization from recoil in the medium. The resulting particles produced (mesons, nucleons, and photons) either lose their energy by ionization, or interact further in the material, or decay. Hadronic particles thus initiate showers, conceptually similar to their electromagnetic counterparts, but with dimensions characterized by the nuclear interaction length, λ_{INT}:

$$\lambda_{INT} = 35A^{\frac{1}{3}} \left(\frac{g}{cm^2}\right), \tag{21}$$

where A is the atomic number of the material. As with the radiation length, the longitudinal and transverse profiles of the shower scale with λ_{INT} for hadronic showers, in an approximately material- independent way. The depth of material needed to contain showers of a given energy increases only slightly with energy, with $\approx 6\lambda_{INT}$ needed for 99% containment of 5 GeV showers, and $\approx 9\lambda_{INT}$ for such containment of 210 GeV showers [26]. From Equations (11) and (21), it follows that:

$$\frac{\lambda_{INT}}{X_0} \approx 0.12\, Z^{\frac{1}{3}}. \tag{22}$$

Equation (22) is the basis for particle identification in calorimeters: the higher the Z of the absorber, the greater the difference between the spatial profiles of electromagnetic and hadronic cascades. Identification of the primary particle is made possible by cuts on such shower shapes, and is facilitated in high-Z materials. The size of the calorimeter necessary for containment of hadronic shower energy is dictated by λ_{INT}.

The nuclear binding energy released during the breakup of the nuclei, which can account for as much as 25% of the energy of the incident hadron, is invisible to most existing calorimeters, and is the source of significant fluctuations in the detected hadron signal. Neutrons produced do not interact electromagnetically (in the context relevant to this discussion), and hence deposit directly no detectable energy in the form of ionization: they deposit energy exclusively by strong interactions, with additional associated binding energy that remains undetected. In addition to these losses, the production of secondary particles that deposit little or no energy in the calorimeter contributes to the increased fluctuations in the measured hadron signal. Muons/neutrinos (from charged pion or kaon decay, for example) deposit little/no energy in the calorimeter, and thus escape only (at best) marginally detected. K_L^0 produced (with a lifetime of $c\tau \approx 15$ meters) can also escape. Effectively, then, containment of hadron showers is a harder problem than containment of electromagnetic ones. The aforementioned processes give rise to 2 basic effects:

(1) the fluctuations in the energy that escapes undetected significantly broadens

the distribution of the hadronic shower, making the attainable energy resolution significantly worse in hadron calorimeters than electromagnetic ones; and

(2) because of such undetectable shower components, the intrinsic energy deposition in an infinite, homogeneous calorimeter will generally be greater for electrons than for hadrons, at the same incident energy.

The hadronic shower can be thought of as consisting of two components: an electromagnetic and non-electromagnetic component. π^0's and η's, which readily decay to photons, will result in an electromagnetically-induced component of the hadronic shower, which behaves as described in the beginning of this chapter. The portions of the shower that do not result in π^0 or η production will behave as a hadronic shower, with its characteristic large fluctuations in energy loss and generally reduced response. Figure (8) shows a monte carlo simulation of the signal resulting from a hadron incident on a material, normalized to the incident energy. The two distinct shower components are shown, with their characteristic differences in width and mean energy.

The overall hadronic signal, in general, is a convolution of the two curves. The fraction of the hadronic shower that results in π^0 or η production (f_{em}) exhibits large, non-Gaussian fluctuations at a fixed incident hadron energy, and its mean value grows logarithmically with the energy ($< f_{em} > \approx 0.1\ ln(E(\mathrm{GeV}))$). If the response of the calorimeter to electromagnetic showers is not the same as that for hadronic showers, ($\frac{e}{h} \neq 1$), the signal no longer scales linearly with the energy and, in general, the resolution will not scale as $\frac{1}{\sqrt{E_0}}$. The visible energy distribution for mono-energetic hadrons will also be non-Gaussian. Equalizing the response of the calorimeter to the two shower types ($\frac{e}{h} = 1$) eliminates the contribution to the energy resolution of the fluctuations in f_{em}, and restores linear. Gaussian response to hadronic showers. A calorimeter with $\frac{e}{h} = 1$ is said to be compensating. All of the above effects have been observed experimentally.

Figure (9) shows the results of a monte carlo study of the response of a hadron calorimeter for different values of $\frac{e}{h_{intr}}$, which is defined using the appropriate mean values from Figure (8). (h_{intr} is the response of a hadron calorimeter to the non-electromagnetic component of the hadronic shower.) The signal is significantly non-linear for $\frac{e}{h_{intr}} \neq 1$, while for $\frac{e}{h_{intr}} = 1$ it is linear over 3 orders of magnitude. Figure (10) shows the measured energy resolution, as a function of energy, for two different calorimeters: the CDHS calorimeter ($\frac{e}{h} \approx 1.4$) and the calorimeter for the HELIOS experiment ($\frac{e}{h} \approx 1$). The resolution scales with $\frac{1}{\sqrt{E_0}}$ in the latter case, but shows significant deviation from linearity in the former.

The energy resolution can be expanded in a power series in E:

$$\sigma^2(E) = \sigma_1^2 + \sigma_2^2 E + \sigma_3^2 E^2 + ... \tag{23}$$

and, dividing by E^2.

$$\left(\frac{\sigma}{E}\right)^2 = \frac{\sigma_1^2}{E^2} + \frac{\sigma_2^2}{E} + \sigma_3^2 + ... \tag{24}$$

At low energies, the first term on the right hand side will dominate – it is dominated by electronic noise. The second term on the right is the sampling term, which dominates the resolution in most practical sampling calorimeters, and reflects fluctations in the signal that are described by statistically-governed processes (such as the sampling fluctuations described above). At high energies, the so-called constant term (σ_3) will dominate: it includes calibration errors and other systematic contributions to the uncertainty in the overall energy scale.

The noise term σ_1 is in general negligible at GeV or higher energies. Typical values of σ_2 for hadron calorimeters range from $\approx 50\%$ to 100% (with E in GeV). At 1 TeV, the contribution to the resolution from the sampling term becomes $\frac{70\%}{\sqrt{1000}} \approx 1.6\%$. Figure (11) shows a plot of the constant term in the energy resolution as a function of $\frac{e}{h}$ (evaluated at 10 GeV). A deviation from unity of only $\approx 10\%$ in $\frac{e}{h}$ gives a constant term comparable to the sampling term above. At high energies, then, $\frac{e}{h}$ must be very close to 1 in order to prevent the constant term from dominating

the resolution. This problem is receiving much attention in Superconducting Super Collider detector design.

In the early days of the study of calorimetry, it was thought [26] that the most direct (and perhaps the only practical) way to achieve compensation was through the use of uranium absorber. The hadronic portion of the shower was thought to easily induce fission in the radioactive uranium nuclei, which prompted (primarily) the production of soft photons. This made some of the hadronic components of the shower visible in uranium calorimeters that were thought to remain invisible in calorimeters composed of other materials. It has been shown, however, that the photons so produced are of sufficiently low energy that their detection in uranium is significantly reduced (due to the magnitude of the cross-section for the photo-electric effect in high-Z materials at low energies), diminishing the importance of the above effect. Uranium has been shown to be neither necessary nor sufficient for compensation – approximate equalization of the electron and hadron response has been realized in detectors of, for instance, lead absorber (using scintillator readout) by the ZEUS collaboration [32].

It is interesting to note, however, that the preferential absorption of low-energy photons in materials of high-Z, and the fact that this low-energy component comprises a large portion of the electromagnetic signal, helps to reduce the overall response of the calorimeter to the electromagnetic component of the hadronic shower. This helps to equalize the electromagnetic and hadronic response by reducing e. The compensation of the D0 calorimeter ($< \frac{e}{\pi} > = 1.03$, for incident electrons and pions of 20 to 150 GeV), with its very high-Z absorber and low-Z readout material, is thought to be enhanced primarily through the effects of this process.

<u>Some Details on the D0 Calorimeters</u>

Uranium/liquid argon calorimetry is employed at D0. It is subdivided in angle into $\approx$ 5000 projective square towers that point to the interaction point, each subtending $\Delta\eta X \Delta\phi \approx$ 0.1X0.1. Each tower is further subdivided longitudinally into the electromagnetic (EM), fine hadronic (FH), and coarse (or outer) hadronic (CH)

sections, which provide information on the longitudinal shower development. The 3 separate cryostats contain modules that are designed and stacked in appropriate ways so as to preserve the projective geometry. These modules are independent structural units that are mechanically linked to maintain structural integrity and inter-module spacing. The readout electronics for all three calorimeters is identical, with each cryostat consisting of $\approx$ 15,000 channels of readout. The central calorimeter is the main subject of this study, and it is the primary focus of the discussion below.

The choice of uranium/liquid argon calorimetry for D0 was motivated by a number of factors. One of the more important reasons is that it is easily segmented. Position resolution of electromagnetic showers using calorimetric information, which is important for electron identification, is enhanced with fine transverse segmentation, while fine longitudinal segmentation aids in hadron/electron particle identification. Calorimeters using scintillators as readout material are limited in the amount of segmentation that can be achieved because of the large amount of space required at each tower boundary to route the signals out of the active volume (light guides, wave shifters, etc.); a high degree of segmentation would result in a prohibitively reduced active calorimeter area. Liquid argon readout does not have this complication, and thus also allows for a calorimetric volume that has a minimum number of dead spots. Homogeneity of response is another important advantage in liquid argon systems. The calorimeter contains uranium plates that lie in a bath of the argon liquid. Other than differences in density (or temperature) throughout the volume (which are small), the response in liquid argon should be uniform. In principle, the absolute calibration (the conversion factor relating units of readout (ADC counts) to energy deposited (in MeV)) can be determined for a finite portion of the detector, with knowledge of detector parameters (sampling fractions, capacitance, etc.) allowing the extrapolation to other portions. Liquid argon is also radiation hard. The detector is constantly bombarded by radiation during collider running (typical mean charged particle multiplicities can reach $\approx$ 30/event at Tevatron ener-

gies), which in detectors using scintillators can seriously degrade the response over time. Argon resists such damage due to radiation, with little or no accompanying change in detector performance. The calibration is, therefore, stable, and, once done, should be good (with minor corrections due to argon purity or temperature fluctuations) for the life of the detector. Scintillator must be repeatedly calibrated in test beams. Also, liquid argon calorimeters are operated as unit-gain ionization chambers, which allows for system stability over time. Fluctuations in the gain of devices run in proportional mode (such as gas calorimeters) can be difficult to characterize and control. Also, because such detectors rely on multiplication of a small number of primary ionization electrons, small fluctuations in the numbers of such primaries can have a large impact on the signal.[2] There is no such amplification of the signal in the argon in the D0 calorimeter: the number of primary electrons collected in the gap is comparatively large in liquid media, making such fluctuations in the number of primaries a relatively insignificant problem.

Uranium is a very high-Z material which, as discussed above, allows for a very compact detector that reduces both size and cost. Particle identification on the basis of longitudinal shower development is enhanced in calorimeters employing high-Z absorbers as well. As mentioned above, the use of uranium is neither necessary nor sufficient to ensure compensation, but its nuclear characteristics are believed to contribute to equalizing the response to electrons and hadrons.

The most obvious disadvantage of using liquid argon is the cryogenic environment that it requires. Particles emanating from the event vertex lose energy in passing through the stainless steel cryostat walls. Unless measures are taken to try to sample this energy, it is not detected, and corrections must be modelled and applied to the data. Building a hermetic calorimeter is a difficult technical challenge in cryogenic sytems as well; D0 uses three cryostats (one central, one forward, and one backward) to accomplish this goal. Because it is a unit-gain system, the ultimate

[2] Large fluctuations in the primaries can result, for example, from a small number of shower particles travelling far distances, parallel to the plates, within the gap of active material.

size of the signals is small ($\approx$ femto- or picocoulombs), which dictates that proper attention be paid to shielding the signals as they emerge from the cryostat, and to proper grounding. (More will be said about this later.) The speed of the charge collection can also be a problem: the full width of the liquid argon pulse at D0 is $\approx$ 400 nanoseconds. This is well below the 3.5 μsec crossing time (see below) used at present, but will become a difficulty for future experiments, where $\approx$ 150 nanosecond collection times (or less) will be required. Also, uranium has the disadvantage of being difficult to work with – it is radioactive, which requires that special care be taken in handling it, and it is difficult to machine.

The basic longitudinal unit in the calorimetry is the unit cell; Figure (12) shows a longitudinal section through a portion of a calorimeter module. It consists of one uranium (or, where applicable, copper) absorber plate, one liquid argon gap, and one signal board situated in the middle of the gap. All argon gaps are 4.6 mm (2.3 mm on either side of the signal boards), but the thickness of the absorber plates varies from section to section. The signal boards contain a copper plane sandwiched between two layers of G-10, onto which copper readout pads of appropriate size are etched. Most of the pads are of size $\Delta\eta X \Delta\phi \approx 0.1 X 0.1$, as described above, and therefore increase in size with radial distance from the beam axis. A layer of graphite-loaded resistive epoxy of $\approx$ .001 inches thickness is applied to the outside of the boards, which plays the role of the high voltage electrode; the uranium is at ground. Shower particles, upon traversing the gap, ionize the argon. Positive high voltage of 2.5 KV is applied to the resistive coat on both sides of the boards, which provides the drift field for this ionization. The ionization current is capacitively coupled from the resistive layer to the signal pads, which thus sample the charge.

The G-10 between the coat and the copper pad (called the blocking capacitor) decouples the high voltage from the preamplifiers, whose inputs are directly connected to the pad through copper traces that route the signals out of the cryostat. As negative electrons drift through the gap and collect on the resistive coat, there is a concomitant decrease in the local voltage at the pad. Positive charge collects

on the pad in response to the excess of negative charge at the resistive coat, which creates a current that is integrated by the preamplifier. The resistance-per-unit-area of the resistive coat is chosen so that the voltage change at the pad is in fact a local one: pad-to-pad coupling should be small to prevent cross-talk between neighboring cells. In addition, the resistance between the pads and the high voltage must be large enough so that the voltage drop upon charge collection is not immediately cancelled by the high voltage supply. To accomplish the above with individual resistors would require elements capable of withstanding steady-state liquid argon temperatures ($\approx$ 70 degrees Kelvin), as well as frequent cryogenic cycling from very low to room temperatures. The resistive epoxy, which is sprayed on to the readout boards, eliminates this aspect of the problem.

A unit cell consists of $\approx 1\ X_0$ of material in the electromagnetic sections, ≈ 0.06 λ_{INT} in the fine hadronic section, and $\approx 0.3\ \lambda_{INT}$ in the coarse hadronic. In general, a given readout signal consists of the output from more than one unit cell: cells of a fixed η and ϕ are locally ganged (longitudinally) before they are read out. An independent readout channel, then, is a sum of the signals in a number of different unit cells. At a fixed radius in the central calorimeter (called a layer), the number of unit cells contributing to the sum is the same for all ϕ and η.

The central calorimeter (CC) is composed of 64 trapezoidally-shaped modules oriented parallel to the incident beam axis. The innermost electromagnetic section is composed of 32 modules, each subtending 0.2 radians in ϕ, and is composed of 21 radiation lengths of material. The signal is sampled longitudinally 4 times, at 2, 4, 11, and 21 radiation lengths. The transverse segmentation is 0.1 X 0.1 in $\Delta\eta X \Delta\phi$, except in the third electromagnetic layer (near the maximum for electromagnetic showers) where it is 4-times as fine ($\Delta\eta X \Delta\phi \approx 0.05 X 0.05$). The fine segmentation at shower maximum helps in the position determination of the electron. The electromagnetic section uses uranium plates of 3 mm thickness, separated by the standard 4.6 mm gap for charge collection, and covers up to $|\eta| \lesssim 1.2$.

The CC fine hadronic section is similar in construction to the electromagnetic

section. The signal is read out three times (1.3, 2.3, and 3.1 λ_{INT}), and 6 mm uranium absorber is used. The longitudinal segmentation is dictated in part by the attempt to equalize the capacitance of the readout channels, which is proportional to both the pad area and the number of ganged cells that make up a readout channel. The increase in size of the copper pads with depth is compensated for by the associated decrease in the longitudinal segmentation. More will be said about the channel-to-channel capacitance variations, and its effect on the measurements made, in Chapter VI.

Shower energy is read out once in the coarse hadronic section (at 2.9 λ_{INT}). It employs copper absorber plates of 46.5 mm thickness. The coarse section provides the type of sampling that the name implies: lying at the outermost portion of the calorimeter (between 4 and 7 λ_{INT}), it samples the final portions of the hadronic shower. Resolution and longitudinal shower information is less important here than gross containment of the shower energy. This motivated the choice for a single longitudinal sampling of the energy (reducing the number of readout channels), and the choice of copper (which is cheaper, easier to work with, but of lower Z than uranium) as absorber. The transverse segmentation in both of the hadronic layers is $\Delta\eta X \Delta\phi \approx 0.1 X 0.1$ throughout. Table III.2 summarizes some of the more important parameters of the central calorimeter.

The endcap calorimeters are conceptuallv similar to the central calorimeter, and provide overall coverage to about 2 degrees of the beam axis, or $\eta \approx 5$. The fine hadronic section is separated into an inner (IH) and middle (MH) portion. The electromagnetic section in each endcap consists of one module, with plates oriented perpendicular to the beam axis, situated closest to the interaction point and subtending $|\eta| \approx 1.3$ to 4.2. Transverse segmentation throughout the endcaps is similar to that of CC for most η ranges.

The ganged signals for each η, ϕ tower in a given readout layer in the detector are brought to the ends of the module by copper traces in the readout boards. Approximately 12 feet of coaxial cable carries the signal to feedthrough ports located

Readout Layer	Absorber plates	No. unit cells per readout layer	Thickness per readout layer	Approx. η coverage	Transverse segmentation ($\Delta\eta X \Delta\phi$)
EM1	3 mm U	2	2 X_0	$\pm$ 1.2	0.1X0.1
EM2	3 mm U	2	2 X_0	$\pm$ 1.2	0.1X0.1
EM3	3 mm U	7	7 X_0	$\pm$ 1.1	0.05X0.05
EM4	3 mm U	10	10 X_0	$\pm$ 1.1	0.1X0.1
FH1	6 mm U	21	1.3 λ_{INT}	$\pm$ 0.9	0.1X0.1
FH2	6 mm U	16	1.0 λ_{INT}	$\pm$ 0.8	0.1X0.1
FH3	6 mm U	13	0.8 λ_{INT}	$\pm$ 0.7	0.1X0.1
CH	46.5 mm Cu	9	2.9 λ_{INT}	$\pm$ 0.5	0.1X0.1

Table III.2. A few parameters for the 8 readout layers of the central calorimeter. All liquid argon readout gaps are 2 X 2.3 mm (see text for details).

on the cryostat body. Twenty-seven-layer feedthrough boards map the signals from their natural coordinate system internal to the cryostat (that of a single depth for all η and ϕ) to the geometry relevant for triggering, called the trigger tower. The trigger tower, which is an η, ϕ cone of 0.2 X 0.2 (consisting of all depths), is the solid-angle unit in which rapid hardware and software calculations of total and transverse momentum are made in order to cull out those events containing the interesting physics. The signals are then routed via $\approx$ 10 feet of twisted pair cable to the preamplifier boxes, which live atop the cryostats. There are 12 preamplifier boxes that process the D0 calorimeter signals, 4 on each cryostat, with each servicing a quadrant of the calorimeter on which it sits.

The signals then travel down $\approx$ 80 feet of twisted pair cable to the baseline subtractors (BLS), which are housed in crates below the platform that supports the detector. The signal (i.e., the voltage) is sampled twice at the BLS: just before its rise (called the base sample) and $\approx$ 2.2 μsec later at its peak (peak sample). (The risetime of the amplified and shaped signal is about 2 μsec.) The base sample provides a reference voltage, or baseline, that exists in the absence of signals, and just prior to the particular crossing of interest: it thus accounts for overall drifts

of the system. The sampling of the collider signal itself is called the peak sample. The BLS's also slightly amplify the signal, do some signal shaping, and allow time-multiplexing of the signals. The difference between the peak and base is taken, and the signal is shipped to a Movable Counting House (MCH), in which the digitization is done.

The Tevatron produces counter-rotating bunches of protons and antiprotons, which are steered by superconducting magnets to collide at the interaction point (nominally, Z=0) of the detector. The bunches collide every 3.5 μsec, called the crossing time. The interaction rate at collider luminosity is:

$$L\sigma \approx \frac{10^{30}}{cm^2 - sec} \text{ (50 millibarns)} = 50 \text{ kHz}. \tag{25}$$

where σ is the total inelastic $\bar{p}p$ cross-section and L is the luminosity.

The sampling of the signal by the electronics is synchronized to the accelerator, with the base-to-peak sample time of 2.2 μsec smaller than the 3.5 μsec Tevatron crossing time. The 1.3 μsec difference is used for transporting and processing the signal after a given crossing, leaving enough time for our system to recover in order to acquire data on the following one.

Having received an appropriate signal from the Level 1 trigger indicating the presence of a potentially interesting event, the signals are digitized by 15-bit ADC's. (The Level 1 trigger is a hardware trigger that provides the first level of event filtering; it reduces the rate by about a factor of 500.) The multiplexing of the signals at the BLS allows for each ADC to digitize 16 calorimeter signals, reducing the number of ADC's needed for digitization. The signals are then shipped to one of 50 Level 2 nodes (a farm of Microvax computers), each containing the filtering code for the second level of event filtering. The rate into the Level 2 nodes is about 100 Hz. Since the data-writing capability is about 1-2 Hz, the Level 2 has been designed to reduce the data by about a factor of 100. The data is then shipped to our host computer, where the data is logged to tape. An event consists of $\approx$ 50 to 100 kbytes of data, gleaned from the $\approx$ 100,000 total channels of detector readout.

Of most interest in this study is the calorimeter front end electronics (preamplifiers, BLS, and ADC). The calorimeter calibration, a primary topic of this thesis, provides the energy scale to convert from ADC counts to energy deposited in the calorimeter, and requires a detailed understanding of the behavior of the front end electronics. More will be said about the properties of the calorimeter electronics, and the impact of its behavior on measurement, in the following chapters.

CHAPTER IV

COSMIC RAYS

It is useful to classify cosmic ray radiation into two categories: primary and secondary radiation. Primary cosmic rays consists of particles that exist outside of the earth's atmosphere, free from secondary production therein. Secondary radiation is created when a primary particle impinges upon the atmosphere to produce secondary reaction products from collisions with the air molecules.

Primary radiation just outside the earth's atmosphere consists primarily of nuclei whose electrons have been stripped off. Protons (hydrogen nuclei) are the dominant component, with helium nuclei providing the bulk of the remaining flux. A small fraction of the total radiation is composed of heavier nuclei, such as oxygen, carbon, nitrogen, etc. In general, the relation between the fluxes of the three components, normalized to the proton flux, is [34]:

$$\text{flux}_{proton} \ : \ \text{flux}_{\alpha} \ : \ \text{flux}_{other} \approx 1 \ : \ \frac{1}{7} \ : \ \frac{1}{60}. \tag{26}$$

The flux reaches a maximum at a kinetic energy of $\approx$ 300 MeV/ nucleon for all species. The spectrum falls monotonically at higher energies, following a power law at kinetic-energies-per-nucleon $\gtrsim$ proton mass:

$$N(E)dE = (\text{kinetic energy})^{-2.6}\, dE. \tag{27}$$

For this discussion, the contribution to the secondary radiation resulting from collisions of heavier nuclei ($> 2m_{proton}$) with molecules in the earth's atmosphere can be considered to be negligible.

The atmosphere acts, in essence, like a large calorimeter: incident primary particles (mainly protons) interact with nuclei in the atmosphere via the strong force, with secondary production dominated by creation of pions (both charged and neutral), but with strange particles (i.e., kaons of various species) and nucleons (secondary protons and neutrons) also being produced. These secondaries are produced

in a fairly collimated stream, with a large forward momentum component. The secondaries induce nuclear reactions of their own until their energy is $\approx$ 1 GeV (near threshold for multiple pion production). The axis of the resulting shower reflects the directionality of the incident primary, with its transverse and longitudinal dimensions characterized by the nuclear interaction length of air ($\approx 90 \frac{g}{cm^2}$, about half that of uranium), as described in the previous chapter. There is also, as previously described, a purely electromagnetic component to the hadronic shower: this cascade is started primarily by the decay of π^0's, produced in the hadronic shower, to two photons. The π^0 lifetime is very short ($\approx 8.4 \times 10^{-17}$ seconds), with its branching ratio to 2-photons close to 99%. Accordingly, the almost immediate decay of π^0's to photons results in the initiation of an electromagnetic cascade.

Charged pions, with a mean lifetime $\tau_{\pi^\pm} \approx 2.6 \times 10^{-8}$ seconds, decay more slowly to muons:

$$\pi^\pm \rightarrow \mu^\pm + \nu_\mu \qquad \text{(branching ratio} \approx 100\%). \tag{28}$$

Muons themselves decay with a lifetime $\tau_\mu \approx 2.2 \times 10^{-6}$ via:

$$\mu^\pm \rightarrow e^\pm + \nu_e + \nu_\mu \quad \text{(branching ratio} \approx 100\%). \tag{29}$$

Energetic charged pions that decay to muons at the top of the atmosphere can result in the production of muons of sufficient energy to reach the surface of the earth prior to decaying to electrons. A relativistic muon, travelling in its rest frame, decays in a time τ_μ. In the laboratory (stationary, or earth rest frame), it decays in a time $\approx \gamma\tau_\mu$. The Lorentz factor (γ) of a muon, produced with a purely vertical velocity component of magnitude v, that would be necessary for it to reach the earth before decaying can therefore be roughly estimated from:

$$\gamma v \tau_\mu \approx D_a, \tag{30}$$

where D_a is the depth of the atmosphere ($\approx 1030 \frac{g}{cm^2}$, or $\approx$ 10 km). This gives $\gamma \approx 15$, and the kinetic energy of such a muon is $\approx$ 1.5 GeV.

Pion energy varies with depth in the atmosphere: for the most part, the deeper within the atmosphere one goes, the less energetic the secondaries. Those muons that result from decay of pions of smaller kinetic energy (either at the top or deeper in the atmosphere) will have a larger probability to decay to electrons, which will induce electromagnetic cascades themselves. Figure (13) is a plot of the vertical flux of various components of cosmic rays as a function of depth within the atmosphere. The hard component is dominated by muons, while electrons comprise the bulk of what is called the soft component.

To establish an order-of-magnitude for the minimum energy with which a muon produced in the upper atmosphere must be produced in order to reach the earth, we must add ionization losses of the muons (which do not shower) in the atmosphere:

$$E = < \frac{dE}{dx} >_{mip}^{atmosphere} \cdot 1030 \frac{g}{cm^2} \approx 1.9 \text{ GeV}. \tag{31}$$

Therefore, muons must be produced of energy $\gtrsim$ 3.5 GeV at the top of the atmosphere in order to reach sea level intact.

Because muons lose energy primarily by ionization, the dominant component ($\approx$ 75%) of the cosmic ray flux at sea level is attributable to muons. Their mean energy at the earth's surface is $\approx$ 2 GeV, with a spectrum that falls like E^{-2} for muon energies below $\approx$ 1 TeV (where well over 99% of the flux is). The flux also falls like $cos^2\theta$, where θ is the angle the particle makes with the vertical. The total flux per unit solid angle per unit horizontal area about the vertical direction, at sea level, is $\approx 0.011/\text{cm}^2 - \text{sec} - \text{sterad}$ [70].

CHAPTER V

ENERGY LOSS OF CHARGED PARTICLES IN MATTER: IONIZATION LOSSES

The theory of energy loss has been developed by a number of investigators [36-40,42,45]. Bohr's initial classically-derived formula, found to provide a reasonable description of the energy loss of heavy nuclei and slow alpha particles, gave an overestimate of the energy loss for single particles (electrons, muons, protons), and even fast alpha particles. Bethe and Bloch [37,40] introduced a quantum-mechanical calculation that has survived as the most accurate description of $\frac{dE}{dx}$, with corrections attributable to the density effect described by Fermi [38], and investigated further by Sternheimer [46,48]. Fluctuations in the energy loss have been examined by a number of authors [36,39,42,45,49,50]. Of most interest here is the theory developed by Landau [39]. Since muons (the subject of interest in this thesis) lose most of their energy by ionization, the primary focus below is on this energy loss mechanism.

Average Energy Loss

A massive particle ($m \gg m_e$) of charge ze is incident on a material, with velocity v that is large compared to the orbital velocity of the electrons of the medium; the electrons in the medium are thus considered to be essentially at rest. It is further assumed that only small momentum transfers are involved, so that the material electron recoils only slightly, and the perturbation of the trajectory of the incident particle is also small.

The transverse component of the electric field seen by the collision electron from the incident particle is a function of time, and is given by [41]:

$$E_\perp(t) = \frac{\gamma z e b}{(b^2 + \gamma^2 v^2 t^2)^{\frac{3}{2}}}, \tag{32}$$

where b is the impact parameter, or point of closest approach, and γ is the Lorentz factor $\frac{1}{\sqrt{1-\beta^2}}$. By symmetry, only the transverse component of the field will contribute to the resulting momentum transfer imparted to the incident projectile (for small deflections, the longitudinal force felt by the particle on either side of the

target electron will be equal in magnitude and opposite in direction.) The incident particle reaches the point of closest approach at time t=0. With:

$$\Delta p = \int F dt = \int e E_{\perp}(t) dt,$$

the momentum transfer imparted to the electron is then given by:

$$\Delta p = \gamma z e^2 b \int \frac{dt}{(b^2 + \gamma^2 v^2 t^2)^{\frac{3}{2}}}. \tag{33}$$

This yields:

$$\Delta p = \frac{2ze^2}{vb}, \tag{34}$$

implying that the energy transferred to the electron in a single collision is given by:

$$\Delta E(b) = \frac{(\Delta p)^2}{2m_e} = \frac{2z^2e^4}{m_e v^2 b^2}. \tag{35}$$

It will be noticed that the energy transfer is proportional to b^{-2}, implying that the incident particle suffers the largest energy loss at close range.

It is instructive to calculate the relative contributions (within the limits of the assumptions made) from collisions with nuclei and those with the atomic electrons. For equal impact parameters and incident velocity, application of Equation (35) yields:

$$\frac{\Delta E(\text{electrons})}{\Delta E(\text{nuclei})} \approx 4000. \tag{36}$$

Thus, the energy loss due to collisions with the atomic electrons is far more significant than that due to nuclear collisions.

The total energy loss per unit length is determined by computing the number of electrons encountered by the particle in a cylindrical shell of radius $2\pi bdb$ in a length dx, and integrating Equation (35) over all possible impact parameters:

$$\frac{dE}{dx} = 2\pi N Z \int_{b_{min}}^{b_{max}} \Delta E(b) b db. \tag{37}$$

where N is the number of atoms per unit volume in the material, Z is the atomic number of the material, and b_{min} and b_{max} are the minimum and maximum allowable impact parameters, respectively. Performing the integration in Equation (37) gives:

$$\frac{dE}{dx} = 4\pi N Z \frac{z^2 e^4}{m_e v^2} \ln \frac{b_{max}}{b_{min}}. \tag{38}$$

It remains to obtain expressions for the minimum and maximum impact parameters: these will be estimated from physical arguments.

The minimum impact parameter, b_{min}, can reasonably be expected to correspond to the maximum allowable energy transfer, E'_{max}. Those interactions that result in a head-on collision between the target electron and the incoming particle transfer the maximum energy, which is given by (from momentum and energy conservation) [42]:

$$E'_{max} = 2m_e c^2 \frac{p^2 c^2}{m_e^2 c^4 + m^2 c^4 + 2m_e c^2 (p^2 c^2 + m^2 c^4)^{\frac{1}{2}}}. \tag{39}$$

If $m \gg m_e$, and a "low momentum" condition $p \ll \frac{m^2 c}{m_e}$ is met (for $m = m_\mu$, this results in p $\ll$ 20 $\frac{\text{GeV}}{\text{c}}$), this reduces to:

$$E'_{max} \approx 2m_e \gamma^2 v^2. \tag{40}$$

Equating the right hand side of Equation (40) with the right hand side of Equation (35), with the latter evaluated at b_{min}, gives:

$$b_{min} = \frac{ze^2}{\gamma m_e v^2}. \tag{41}$$

An expression for the maximum impact parameter, b_{max}, is obtained from consideration of the time duration of the collision. The derivations above assumed a free target electron, which, in the limit of small impact parameters, is a valid assumption (see below). The electron is, however, bound in the atom. If the collision time is short compared with the orbital period of the electron, the interaction can be assumed to be sudden enough for the electron to be considered free. If it is long compared to the period, the electron revolves about the atom many times during

the collision. Such an adiabatic collision is no longer described by the interaction of an incident particle with a free electron. The transverse component of the electric field, a function of time as given by Equation (32), is sharply peaked at t = 0. The full-width-at-half-maximum is a good measure of the time over which the field is appreciable, and is given approximately by:

$$\text{FWHM} \approx \frac{b}{\gamma v}. \tag{42}$$

Equating the above equation with the time of collision, we obtain:

$$\Delta t_{coll} \approx \frac{b}{\gamma v}. \tag{43}$$

The above expression explicitly shows the linear relation between the impact parameter and the time of collision, for fixed incident particle velocity. In view of the above arguments, it is reasonable to define b_{max} at the point where the time of collision is comparable to the inverse of the angular frequency of the bound electron (ω):

$$b_{max} \approx \frac{\gamma v}{\omega}. \tag{44}$$

Equation (44) gives the upper limit, within the limits described, of the impact parameter. Substituting Equations (41) and (44) into (38) gives an approximate expression for the energy loss, classically derived, that varies only slightly from that obtained by Bohr [36]:

$$\frac{dE}{dx} = 4\pi N Z \frac{z^2 e^4}{m_e v^2} ln \frac{m_e \gamma^2 v^2}{z e^2 \omega}. \tag{45}$$

Proper treatment of the electrons in the medium as harmonically bound charges gives the Bohr result:

$$\frac{dE}{dx} = 4\pi N Z \frac{z^2 e^4}{m_e v^2} \left[ln \frac{1.123 m_e \gamma^2 v^2}{z e^2 < \omega >} - \frac{v^2}{2c^2} \right], \tag{46}$$

where $< \omega >$ is an average angular frequency of the electrons. The difference between Equations (45) and (46) arises from the term $\frac{v^2}{2c^2}$, which results in a small

correction even at high velocities. For muons of energy $\approx$ 2 GeV, the mean cosmic ray muon energy, it accounts for $\approx$ 2% reduction in $\frac{dE}{dx}$.

As already mentioned, the Bohr result gives a good measure of $\frac{dE}{dx}$ for slow, heavy particles. The breakdown of this semi-classical result occurs for lighter particles of higher velocity. The primary quantum phenomena that cause the breakdown of the Bohr formula in such cases are (*i*) that the energy loss occurs in discrete amounts, and (*ii*) the limitations on the minimum impact parameter that the wave nature of quantum particles impose. From (*i*), it might be expected that the classical result should hold only at impact parameters that give an energy transfer that is large compared to atomic excitation energies. However, statistical interpretation of the energy loss allows the reconciliation of the classical and quantum results: over many interactions at large impact parameters, no energy is transferred. A few collisions, though, result in the exchange of a finite amount of energy. When computed on average, the energy loss in the quantum model can in such a way be reconciled with the loss resulting from the continuum of energy losses in the classical model. In the limit of small energy transfers (quantum-mechanically), then, application of Equation (44) for b_{max} is appropriate, provided the statistical interpretation of the resulting energy loss formula is kept in mind. Condition (*ii*) can be applied to give a quantum-mechanical limit for the minimum impact parameter. Use of the uncertainty principle gives the minimum quantum-mechanical impact parameter for which localization of the wave packet describing the particle is well-defined:

$$b^q_{min} = \frac{\hbar}{p} = \frac{\hbar}{\gamma m v}. \tag{47}$$

Substituting b^q_{min} for b_{min} in Equation (45) gives an approximate result for a quantum treatment of the energy loss:

$$\frac{dE_q}{dx} = 4\pi N Z \frac{z^2 e^4}{m_e v^2} \ln \frac{m_e \gamma^2 v^2}{\hbar < \omega >}. \tag{48}$$

This is to be compared with the Bethe result, which he derived using first order perturbation theory, treating the incident particle as a plane wave (first Born

approximation). The perturbing potential used was the interaction between the incident particle and the electrons in the medium; in the Coulomb gauge, this consists of a term describing the static interaction between the incident particle and the electrons of the medium, and a term describing the coupling between the particle currents and the free photon field. His result was:

$$\frac{dE}{dx} = 4\pi N Z \frac{z^2 e^4}{m_e v^2} \left[ln \frac{2m_e \gamma^2 v^2}{\hbar < \omega >} - \frac{v^2}{c^2} \right], \tag{49}$$

applicable to incident particles with velocities greater than the typical atomic electron velocity in the medium. Other than the factor of 2 in the logarithmic term and the $(\frac{v}{c})^2$ term (which, again, gives rise to a relatively small effect), the results are the same as those in the semi-classical formula, Equation (48).

Replacing the energy associated with the orbital frequency, $\hbar < w >$, with the mean ionization potential, I, of the atoms of the medium in Equation (49) gives the energy loss result of Bethe in its more often expressed form. It reflects a full quantum-mechanical treatment (to first order), and contains a number of interesting features. The loss depends only on the velocity: for particles of given charge and velocity, the energy loss in a given material is the same, independent of their mass. As the velocity increases from zero, the energy loss falls as $\sim \frac{1}{v^2}$. This sharp loss near the end of the particles' path is called the Bragg peak. A minimum is reached for all particles at some velocity, followed by a region where the $ln\gamma^2$ factor begins to dominate, with the energy loss slowly increasing accordingly. This is called the region of the relativistic rise. It is a manifestation of the deformation of the electric field of the incident particle at large velocities, and the associated increase of the maximum impact parameter. This expands the available range for which collisions can contribute to the energy loss.

Equation (49) is in need of two more ingredients, and an additional comment:

(A) The incident particle interacts with many atoms simultaneously – in general, b_{max} is much larger than the typical atomic dimension. Especially when the velocity of the incident particle is large (and b_{max}, as described above, increases)

and/or the material is very dense, its electric field polarizes the medium, perturbing its associated field from the free-field values to those characteristic of a dielectric. This in turn alters the interaction of the field with the electrons in the medium, and results in what is called dielectric screening. The result of this screening is to dampen the increase of the energy loss in the region of the relativistic rise to go as $ln\gamma$ instead of $ln\gamma^2$, with $\frac{dE}{dx}$ becoming nearly constant at very large γ. This screening and the resulting reduction in $\frac{dE}{dx}$ is called the density effect; the flattening out of the energy loss curve for very large velocities is called the Fermi plateau. This effect has been studied in detail by Sternheimer [46,48].

(B) The development of Equation (49) ignores the effect of the spin on the scattering between the projectile (a muon, for example) and the atomic electrons (i.e., magnetic electron-muon scattering.) This effect is appreciable only at higher energies (it comprises about a 0.1% effect at incident muon energies of 5 GeV in liquid argon), and it increases with increasing energy. A small fraction of the cosmic ray muons at sea level have energies higher than 10 GeV; however, the term is included below for completeness.

(C) A basic assumption used in the derivation of Equation (49) is that the velocity of the incident particle is much larger than that of the atomic electrons in the medium. This is uniformly true for energies we are concerned with in this report. It should be mentioned, however, that there is an additional term (not included in Equation (50) below) that corrects for such low velocity effects, that is not commonly used in the characterization of higher-energy phenomena. Since the electron velocity increases with decreasing radius (inner shells <=> higher velocity), the corrections are called shell corrections.

The full expression for the mean $\frac{dE}{dx}$ of a particle as it traverses matter, including the terms describing the density effect and the spin-dependent effects, can now be

written in full:

$$< \frac{dE}{dx} >= 4\pi N Z \frac{z^2 e^4}{m_e v^2} \left[ln \frac{2m_e \gamma^2 v^2}{I} - \beta^2 + \frac{1}{8} \left(\frac{E'_{max}}{E} \right)^2 - \frac{\delta}{2} \right]. \quad (50)$$

The third term in the brackets is the spin term, with E the incident energy of the muon, and δ is the density correction.[3]

Figure (14) shows the measured energy losses of pions and protons of various energies in propane gas at 3 different pressures. The curves show all of the characteristic features of the $\frac{dE}{dx}$ formula: the $\frac{1}{v^2}$ dependence at low velocities, followed by a minimum, and the subsequent relativistic rise. The rise is dampened by the density effect at large velocities: the Fermi plateau is apparent at $\beta\gamma \gtrsim 200$. The $\frac{dE}{dx}$ value at plateau is lower for gases at higher pressure: this is another manifestation of reduced overall $\frac{dE}{dx}$ in denser media.

A related result that has become useful is the mean range of a particle for a decrease in its energy from E to E':

$$R(E \rightarrow E') = \int_{E'}^{E} \frac{dE}{-dE/dx}. \quad (51)$$

Since Equation (50) describes an average energy loss, a monoenergetic beam of particles incident on a material will have a distribution of ranges about the mean range implied by Equation (51).

Equation (50) says nothing about fluctuations in the energy loss. This has been described by Landau, and is discussed in the next section.

Fluctuations in the Energy Loss by Ionization - Landau Theory

Let $\phi(W)dWdx$ be defined as the probability that a charged particle of incident kinetic energy E will experience an energy loss between W and $W + dW$ while traversing a thickness dx (in $\frac{g}{cm^2}$) of absorber. It can be expressed as:

$$\phi(W)dWdx = N \frac{d\sigma(W)}{dW} dWdx \quad (52)$$

[3] Equation (50) is the often-quoted form of the Bethe-Block formula for which the conditions leading to Equation (40) hold. Further details can be found in [48].

where $\frac{d\sigma}{dW}$ is the differential cross section for the incident particle to lose an energy W in a single collision and, as before, N is the number of atoms per unit volume in the target material. The total probability of collision in thickness dx, independent of the amount of energy transfer, is given by qdx:

$$qdx = N\int_0^\infty (d\sigma/dW)dWdx, \tag{53}$$

where it is understood that $\frac{d\sigma}{dW} = 0$ for $W > E'_{max}$.

Let $\chi(W,x)dW$ be the probability that a particle, having crossed a thickness x of absorber, loses energy between W and $W + dW$. For a beam of N_p particles that have traversed x $\frac{g}{cm^2}$ of material, the change in the number of particles that have lost a total energy between W and $W + dW$ after crossing an additional dx of material is influenced by the following two factors:

(1) The number of particles having lost energy between W and $W + dW$ increases in this infinitesimal interval dx, as those particles that had lost less than this amount after traversing x $\frac{g}{cm^2}$ will lose the right amount of energy in dx to place them in the W to $W + dW$ energy interval;

(2) The number of particles in this interval will decrease, as those whose energy loss was in the proper range at x will lose enough energy in dx to remove them from this interval.

The above two conditions can be used to provide a mathematical expression for $\chi(W,x)$. The overall change in the number of particles having an energy loss in the range W to $W + dW$, upon traversing a thickness dx at x, is given by:

$$N_p\chi(W,x+dx)dW - N_p\chi(W,x)dW = N_p\int_0^\infty \chi(W-u,x)\phi(u)dWdxdu - N_p\chi(W,x)dWqdx. \tag{54}$$

The probability function $\chi(W',x)$ is understood to be equal to 0 for $W' \leq 0$ and $W' > E'_{max}$. Equation (54) can be rewritten as:

$$\frac{\partial\chi(W,x)}{\partial x} = \int_0^\infty \phi(u)\chi(W-u,x)du - q\chi(W,x). \tag{55}$$

Equation (54) assumes that the energy loss of the particle is small compared to its incident energy. Landau solved Equation (55) for the regime of interest in this study: that of thin absorbers. An important quantity in his solution is ξ:

$$\xi = \frac{2\pi n_e z^2 e^4}{m_e v^2} x, \tag{56}$$

where n_e is the number of electrons per unit volume in the medium, z is the charge of the incident particle, x is the thickness of material traversed, and v is the incident particle's velocity. ξ is the energy above which, on the average, one delta-ray will be produced. (A delta-ray is a high-energy recoil electron emitted from the absorber after a collision of large energy transfer with the incident particle.)

Requiring that the typical energy loss be (a) large compared to the binding energy of the electrons in the medium, and (b) small compared to E'_{max}, Landau used the method of Laplace transforms to solve for χ in Equation (55). He used the classical free electron cross section in defining q in Equation (53).[4] Conditions (a) and (b) allow χ to be expressed in the factorized form:

$$\chi(W, x) = \frac{1}{\xi} f_L(\lambda) \tag{57}$$

where:

$$\lambda = \frac{1}{\xi}\left[W - \xi(ln\frac{\xi}{\epsilon'} + 1 - C_E)\right] \tag{58}$$

$$ln\epsilon' = ln\frac{(1-\beta^2)I^2}{2m_e v^2} + \beta^2 \tag{59}$$

and

$$C_E = \text{Euler's constant} = 0.577. \tag{60}$$

f_L is called the universal function, and is given by:

$$f_L(\lambda) = \frac{1}{\pi}\int_0^\infty exp[-u(lnu + \lambda)]\, sin(\pi u) du. \tag{61}$$

[4] The classical cross section for a particle of energy E to lose energy W is given by: $d\sigma/dW = 2\pi Z^2 z^2 e^4/m_e v^2 W^2$.

The most probably energy loss is given by:

$$W_{mp} = \xi \left(ln \frac{\xi}{\epsilon'} + 0.198 - \delta \right), \tag{62}$$

where δ is the density correction as given in Equation (50). ϵ' is the low energy loss cutoff value, and was chosen by Landau to make the mean energy loss in his theory agree with that from the Bethe-Bloch formula. (Landau's original expression for W_{mp} was numerically incorrect, and also did not include the density effect term. Later authors [52] improved the theory. An analogous shift due to the density correction should be applied when using Equation (58) to evaluate W.)

Common application of condition (b) dictates that $\xi/E'_{max} \leq 0.01$. In this regime, the probability to emit delta-rays having energy near E'_{max} is small but finite, implying that the distribution will be asymmetric toward higher energy losses: the most probable value (peak) of the distribution will in general be lower than the mean. Figure (15) shows a measured pulse height spectrum of 3 $\frac{GeV}{c}$ protons and 2 $\frac{GeV}{c}$ electrons in an argon-methane gas mixture, illustrating the characteristic skewed shape of the Landau distribution. As mentioned, high-energy delta rays which produce their own secondary ionization are responsible for this shape. A liquid argon gap in the D0 calorimeter can be considered a thin absorber, to which Landau's theory may aptly be applied. Using the appropriate parameters for the D0 liquid argon gaps in Equation (56), along with the mean muon energy for cosmic ray muons ($\approx$ 2 GeV) in Equation (39) for E'_{max}, $\xi/E'_{max} \approx 10^{-4}$, well below the required condition.

The Landau theory is the theory to which the experimental distributions obtained during the Cosmic Ray Run will be compared. Descriptions of the solutions for Equation (55) in other regimes may be found elsewhere [42,45,49,50].

Equations (50) and (56–62) thus give, in principle, a full description of the energy loss by ionization of a particle traversing a homogeneous thin absorber. There are other mechanisms, however, that contribute to the energy loss of muons. These are discussed briefly in the next section.

Other Energy Loss Mechanisms for Muons

The energy loss of high-energy muons in matter can be considered as a sum of the contributions from 4 mechanisms: ionization, muon bremsstrahlung, direct e^+e^- pair production, and photonuclear interactions, such that:

$$\left(\frac{dE}{dx}\right)_{tot} = \left(\frac{dE}{dx}\right)_{ion} - \left(\frac{dE}{dx}\right)_{brem} + \left(\frac{dE}{dx}\right)_{pp} - \left(\frac{dE}{dx}\right)_{n}. \tag{63}$$

Figure (16) shows a plot of the results of calculations of the relative contributions (and the sum) of the above 4 processes to the energy loss of muons in hydrogen, iron, and uranium. Table V.1 shows the contributions of the four processes, as a percentage of the total, to the energy loss for the same 3 materials. The contribution to $\frac{dE}{dx}$ from mechanisms other than ionization become significant at lower energies, the higher the Z of the material. For all media, the sum of the contributions from bremsstrahlung, pair production, and photonuclear reactions accounts for no more than 5% for muon energies below 10 GeV. (Roughly 85% of the cosmic ray muons are below 10 GeV.) In general, as the energy of the incident particle increases, the losses due to ionization increase slowly, while the contributions from the other processes increase more rapidly; their relative contributions at higher energies therefore comprise a significant fraction of the overall energy loss.

The above outline contains all of the significant dynamics regarding the energy loss of muons in matter at the energies we are considering here. The focus in the following chapters shifts to the performance and understanding of the detector, and the comparison of our experimental results with the theoreticai expectations.

	Incident Energy (GeV)	Ionization	Bremsstrahlung	Pair Production	Nuclear Interactions
Hydrogen:	1	100%	<0.1%	<0.1%	<0.1%
	10	99.8%	<0.1%	<0.1%	<0.1%
	100	97.3%	0.9%	1.0%	0.9%
	1000	75.6%	7.8%	10.4%	6.3%
Iron:	1	99.9%	<0.1%	<0.1%	<0.1%
	10	98.3%	0.7%	0.9%	0.2%
	100	78.9%	8.2%	11.6%	1.4%
	1000	23.9%	29.3%	42.9%	4.0%
Uranium:	1	99.8%	0.1%	<0.1%	<0.1%
	10	95.1%	2.2%	2.6%	0.2%
	100	54.2%	18.0%	26.8%	1.1%
	1000	9.1%	35.8%	53.4%	1.7%

Table V.1: Energy loss by 4 different mechanisms (ionization, bremsstrahlung, direct e^+e^- pair production, and nuclear interactions), as a percentage of the total, as a function of incident energy for muons incident on hydrogen, iron, and uranium.

CHAPTER VI

OPERATION AND PERFORMANCE OF THE CALORIMETER ELECTRONICS

The Cosmic Ray Run offered the first opportunity to evaluate the behavior of the full central calorimeter *in situ*. Many basic technical questions were first monitored and analyzed in an environment not terribly dissimilar from collider running. During the design and construction phases, much effort went into building a device that would perform optimally with respect to the physics we were pursuing. These first *in situ* tests of the calorimeter, at times performed in concert with other portions of the detector, were therefore a crucial first-order indication as to how we could expect D0 to perform in the collision hall. A large concern was the behavior of the first full complement of calorimeter electronics, connected to the final calorimeter module array: appropriate attention was therefore paid to electronics issues during the run, with an eye toward potential difficulties that could cause problems during future data-taking.

Some Details on the Calorimeter Electronics

Figure (17) shows an idealized schematic of the calorimeter electronics. C_D is the detector capacitance at the input to the preamp; there is one preamplifier for each calorimeter channel. The voltage pulse at the detector is a triangular-shaped pulse of $\approx$ 400 nanoseconds in duration, as shown in the upper left hand corner of the figure. The output voltage of the preamplifier is given by:

$$V_{out} = \frac{Q_{in}}{C_F} \tag{64}$$

where Q_{in} is the charge collected at the calorimeter cell, and C_F is the feedback capacitance, of either 5.5 or 10.5 picofarads.

After amplification. the signal is shaped in the base line subtractors (BLS), with shaping consisting of one RC ($\approx$ 30 μsec) differentiation followed by one RC ($\approx$ 0.25 μsec) integration and an amplification of X3. The filtered signal (shown in the plot in the middle left hand portion of the figure) is sampled and held twice

in two different arms of a sample and hold module: once just before the rise of the signal, and again at its peak. The difference between the base and peak is taken with a single operational amplifier, which gives a DC output voltage that is proportional to the charge deposited in that channel of the detector. The BLS also time-multiplexes the signals, which helps to reduce the number of ADC's needed for digitization.

In order to get a 15-bit effective dynamic range with our choice of 12-bit ADC's, the signal then undergoes amplification by precision X1-X8 amplifiers in the BLS. The magnitude of the amplification is chosen event-by-event on the basis of the size of the signal: signals below 1.25 volts are multiplied by 8, while those above this value go through the X1 amplification route. A bit containing the information as to the amplification level of the signal at this stage (again, channel-by-channel) is shipped with the data to the ADC's in the Movable Counting House. After digitization, those signals that have gone through the X1 amplification path undergo a 3-bit shift (equivalent to X8 amplification), in order to put all signals (both the X1 and X8 variety) on an equal footing. This puts the full dynamic range at 15 bits ($2^{15} - 1$, or 32,767 ADC counts full scale), while retaining an actual 12-bit digitization process, which helps reduce the time needed to complete the digitization. Twelve-bit ADC's are also considerably less expensive than those using 15-bits. The ADC full input range is 10 volts, with the maximum X8 signal corresponds to 4095 counts. The ADC's also have the capability to store pedestal values (means and widths), in order to perform hardware pedestal subtraction and zero-suppression (to be discussed further below).

One can compute the approximate number of electrons that are deposited in the argon for an ADC output of 32,000 counts. This maximum value corresponds to 10 volts at the output of the BLS. The BLS uniformly multiplies by 3, making the signal at the input to the BLS (or output of the preamp) 3.3 volts. Equation (64),

using the 5.5 picofarad feedback value, gives:

$$Q_{in} = 3.3 \text{ volts} \times (5.5 \times 10^{-12} \text{ farads}) = 1.8 \times 10^{-11} \text{ Coulombs}$$
$$= 1.2 \times 10^{8} \text{ electrons.} \quad (65)$$

It is instructive to put these numbers in perspective.

The amount of energy needed to liberate an $e^- Ar^+$ pair in liquid argon is a well-known experimental number [60]. The number of electrons collected in the argon per MeV of energy deposited by a minimum ionizing particle can then be computed:

$$\frac{1\text{MeV}}{2 \cdot (23.65 \frac{eV}{e^- Ar^+ \text{pair}})} \approx 20000 \frac{e^-}{\text{MeV}}. \quad (66)$$

(The factor of 2 in the denominator on the left hand side reflects the fact that only half the charge produced in the gap is actually collected - see, for example, [59].) We can calculate the energy of the electron that has deposited 1.2×10^8 electrons in the argon:

$$E_{e^-} = \frac{1.2 \times 10^8 \, e^-}{\text{SF} \cdot (\frac{e}{mip}) \cdot 20000 \frac{e^-}{MeV}}$$
$$\approx 100 \text{ GeV}. \quad (67)$$

In order to extend this range still higher, electromagnetic layers 3 and 4 have preamplifiers that have a lower gain by about a factor of 2 (by virtue of their 10.5 picofarad feedback capacitors.) Since a 100 GeV electron deposits $\approx 90\%$ of its energy in these two layers, the full range of the electronics has been designed to accomodate 200 GeV in each of them, or a full electron energy of greater than 400 GeV. (The longitudinal profile does not change much with energy.) This is comfortably above the expected electron energies at the Tevatron. At the low end, a single ADC count corresponds to:

$$\frac{1.2 \times 10^8 \; e^-}{32000 \text{ ADC counts}} \approx 4000 \frac{e^-}{\text{ADC count}}. \quad (68)$$

A minimum ionizing muon deposits:

$$< \frac{dE}{dx} >^{mip}_{argon} \times 0.46 \frac{\text{cm}}{\text{gap}} \approx \frac{1 \text{ MeV}}{\text{liquid argon gap}} \quad (69)$$

Readout Layer	$< C_{tot} >$ (nf)	$< \sigma >_{ped}$ (ADC′ cts)	$< \text{signal} >_{\mu}$ (ADC′ cts)	$< \text{signal} >_{\mu} \div < \sigma >_{ped}$
EM1	1.6	2.8	8	2.9
EM2	1.7	3.2	8	2.5
EM3	1.7	3.3	30	9.1
EM4	2.8	7.8	41	5.3
FH1	5.5	14.2	93	6.6
FH2	5.5	14.4	71	4.9
FH3	5.5	13.8	57	4.1
CH	5.4	4.3	41	9.6

Table VI.1. Some quantities related to signal-to-noise for the central calorimeter. Values are extracted from data taken during the Cosmic Ray Run. $< C_{tot} >$ is the average measured cold capacitance, and ADC′ counts are gain-corrected ADC counts. (Details in text).

which corresponds to $\approx$ 20000 electrons deposited in an argon gap in the calorimeter. The smallest minimum ionizing signals are in EM1 or 2 (2 MeV, or 40000 e^-), which contain the least number of gaps. Using Equation (68), we find that 1 ADC count is then $\approx$ 10% of the smallest minimum ionizing signal in the calorimeter.

The electronics has thus been designed for significant precision at the low end, and the ability to adequately cover a large energy range, as is dictated for collider experiments. It is worth noting that the largest minimum ionizing signal in the calorimeter is that for FH1 (21 gaps), and that this corresponds to $\approx$ 100 ADC counts, which is $\approx$ 3% of the X8 range, or 0.4% of the full dynamic range, of the ADC's. Minimum ionizing signals are thus at the very low end of the system that has been designed.

Noise

Noise of all forms contributes to the resolution of the physics pursued with D0, making it a crucial consideration of detector design, particularly for cases involving many readout channels. As a benchmark, it is desirable that the minimum ionizing signal be above the noise; detection of minimum ionizing particles is desirable as

a means of helping to identify muons in collider events. Early calculations [15,56] suggested that the signal-to-noise for minimum ionizing particles would not present a problem in the D0 calorimetry: the Cosmic Ray Run provided a framework in which to test this *in situ* (see Table VI.1).

The rest of this chapter will describe some of the results, and their significance, of the technical performance of the D0 calorimeter electronics during the run.

Pedestals

In the absence of signals resulting from particle passage through the calorimeter, the electronics readout still has a finite value, called the pedestal. The mean value of the pedestal in a given channel (typically $\approx$ 200 counts) is arbitrary, dominated by a DC offset built in to the electronics to assure that the input to the ADC remain in range. The fluctuations around this mean are due to the noise in the system; in the absence of noise, the pedestal distribution would be a δ-function.

Knowledge and measurement of the pedestals underlies all of the physics measurements made with the calorimeter, with both the mean and width (characterized by the r.m.s. deviation, σ) of interest. Operationally, pedestal means and σ's are calculated by acquiring $\approx$ 650 events that are out-of-time with beam collisions, with each event containing a pedestal value for each channel. From the ADC distribution of these "empty" events, a mean and σ are calculated for each channel. (The calibration program used to compute these values is called CALIB.) After a CALIB pedestal run, the value of the mean and σ for each channel is stored locally in the electronics of the ADC circuit ("downloaded") for use in subsequent physics events.

To make the recorded ADC count proportional to energy, with no artificial offset, the ADC subtracts the pedestal mean from the digitized data signal, channel-by-channel, before it ships the data to the computer to be recorded. This pedestal subtraction is an option, but it is one that was always exercised during the Cosmic Ray Run, and will also be used routinely during collider running.

An important option in the front-end processing of the data that uses pedestal information is called zero-suppression. This capability is essential for collider run-

ning. Reading out all 50,000 channels on each event results in an event record size that is prohibitively cumbersome. In a typical collider event, $\lesssim$ 5% (or $\approx$ 2500) of the channels contain energy from the physics of interest. Because of the noise fluctuations in the pedestal, the "empty" channels cannot be removed on a yes-no basis: all we can ask is whether the signal in a channel is consistent with its pedestal value. Therefore, the ADC suppresses the output of those channels whose energy, after pedestal subtraction, lies within the range $\pm N\sigma$, where N is a parameter chosen prior to the data-taking sequence. Zero-suppression will necessarily cut out some low-energy portion of the physics event; a value of N between $\approx$ 2 and 3 gives a reasonable suppression. The choice of which zero-suppression parameters should be used, and their effects on the data, continues to be the focus of much study by the collaboration.

Some variables in the event, such as the total energy, are event-by-event sums of energy over the 50,000 channels in the calorimeter. Small biases in the calculation of the pedestal means can introduce large errors in the evaluation of the total energy. A bias of +0.1 ADC count in each channel, for example, results in 5000 extra counts of energy in the calorimeter, or about 12 GeV. This number is comparable to the noise contributed by random sources and, as such, is deemed unacceptable (see section below). Similarly, if zero-suppression is used, errors in the computation of the σ's can lead to biases in the data.

In general, the determination and use of pedestal information is one of the most important portions of the calibration program collider experiments. Ultimately, what matters is that the pedestal means and sigmas reflect as accurately as possible their values during the data-taking. The frequency with which pedestal runs are taken is thus determined by the time scale over which overall system drifts, if any, are likely to occur. Also, the accuracy with which pedestals are determined (given by $\frac{\sigma}{\sqrt{N_{events}}}$) should be significantly better than 1 ADC count, our quantized unit of readout.

Sources of Noise

The width of the pedestal is a convolution of 2 random sources: electronic noise and uranium noise. The electronic noise is primarily a result of thermal noise of the conducting channel of the field effect transistor (FET) at the input to the preamplifier. It scales linearly with the capacitance (C_D in Figure (17)), according to the empirically determined formula [15]:

$$\text{EINC} = [1936 + 3200 \times C_D(\text{nanofarads})] \text{ electrons.} \tag{70}$$

EINC is known as the equivalent input noise charge at the input to the FET. Uranium decays via the reaction $^{238}U \rightarrow {}^{206}Pb$ result in the production of photons, electrons, and α-particles that, for the fraction that escape from the uranium, are sampled in the liquid argon gap in the normal manner. Because we measure the pedestal in the presence of the uranium background signal, the energy detected from these decays results in no average offset in real collider events. The fluctuations in the number of sampled tracks resulting from uranium decay do, however, result in an increase in the width of the pedestal with respect to its non-uranium (electronic-only) values.

While the electronic noise distribution is a gaussian, the uranium noise is asymmetric. Figure (18) shows pedestal distributions, both with high-voltage on, in EM2, which uses uranium absorber, and in CH, which uses copper. The relative symmetry of the distributions is evident. Nevertheless, to first order, the total pedestal width is the sum in quadrature of the width from uranium noise and that from the electronic noise:

$$\sigma_{tot}{}^2 = \sigma_{el}{}^2 + \sigma_{ur}{}^2. \tag{71}$$

We would expect, for a fixed plate thickness, that the number of uranium disintegrations sampled in the argon should increase with the total area of a readout channel, A_{tot}:

$$A_{tot} = A' \times N_{gaps}. \tag{72}$$

A' is the cross-sectional area (in $\eta - \phi$) of the readout channel. The fluctuations in the uranium noise should then go like the $\sqrt{A_{tot}}$. (The area increases with both the number of gaps, and with the depth in the calorimeter.) The capacitance of the cell is well-approximated by that of a parallel-plate capacitor:

$$C_{cell} = \left(\frac{A'}{\text{gap width}}\right) \times N_{gaps} = \text{constant} \times A_{tot}. \tag{73}$$

The total capacitance contains contributions from both the cell and the cable that connects the module to the preamplifiers:

$$C_D \equiv C_{tot} = C_{cell} + C_{cable} \tag{74}$$

where $< C_{cable} > = 1.3$ nf, a non-negligible fraction of the total capacitance. We thus have contributions to the noise that depend differently on the specific module and cable parameters:

$$\sigma_{el} \sim C_{tot} \sim (C_{cell} + C_{cable}) \tag{75}$$

and

$$\sigma_{ur} \sim \sqrt{A_{tot}} \sim \sqrt{C_{cell}}. \tag{76}$$

In general, then, the functional dependence of pedestal width with capacitance is straightforward for electronic noise or uranium noise, but can be rather complicated for the total noise (recall Equation (71)). Figure (19) shows a plot of the measured pedestal widths, taken during the Cosmic Ray Run, as a function of capacitance for (a) high-voltage off (electronic noise only) and (b) high-voltage on (electronic plus uranium noise). [5] The linear dependence of the former is evident, while the deviation from linearity is apparent for the total noise. The increase in the total widths upon introduction of uranium noise is also seen. The high capacitance

[5] Collection of any ionisation in the gap, be it from uranium decays or from physics events, requires an electric field in the gap to induce the flow of charge. This can only occur with the high voltage on.

channels having small widths with high voltage on are the coarse hadronic channels in which, because they employ copper absorber, there is no uranium noise.

Pedestal Studies

In the cosmic ray study, the muon-associated signals are of the same order of magnitude as the noise fluctuations. In order to study the noise and its interactions with the signals in detail, we have chosen to take the bulk of the data in this study in a pedestal-subtracted but non-zero-suppressed mode. For this data set, every channel in the calorimeter was read out for every event.

The following study of pedestal bias shows the advantage of such a choice. Using information provided by the central drift chamber, we were able to define a very generous $\eta - \phi$ cone through which the muon had passed. Calculating an average value (and σ) for those channels that were expected to have seen no muon energy (i.e., those channels outside this cone) gives pedestal information that most accurately reflects the true pedestals during the data-taking. Since the raw data was pedestal subtracted using the pedestal means as calculated by CALIB, asymmetries or anomalous structure in the distributions of pedestal means calculated in the above manner (i.e., pedestal-subtracted pedestals) indicate either an inaccuracy in the pedestal determination, or a drift in a portion of the system, or some combination of the two. Figure (20) shows the mean pedestal shifts determined in the above way, for all EM channels and all FH channels. For the EM channels, where the uranium noise is relatively small due to the small total cell area, the distribution of means is peaked at zero and symmetric. The distribution for the FH channels, however, is decidedly skewed toward the positive end, with a (positive) non-zero mean. This effect is now understood to be a result of problems in the CALIB program (this has since been improved), that are exacerbated in channels with more uranium noise. The distributions are excellent examples of some of the problems mentioned above: because of inaccuracies in the calibration program, the pedestal means and σ's "downloaded" to the ADC's were biased representations of the real pedestal means and widths computed during the data-taking. The overall positive

value of the FH distribution, and its skewness, can then bias results. The technique of re-calculating pedestals was implemented throughout this study, even though it will not be available for the zero-suppressed collider data.

The upper portion of Figure (21) shows the averages of the individual channel pedestal means in electromagnetic layer 4, as computed by CALIB, over the Cosmic Ray Run. The fact that the variation is on the order of 0.5 counts over the 2 months implies that we can expect reasonably stable pedestals over long time scales.

Coherent and Incoherent Noise

The total noise in a system consists of two sources: incoherent (or random) noise and coherent (or correlated) noise. Examples of the former are the noise described above which is responsible for the pedestal widths, i.e. electronic and uranium noise. The latter can be due to a number of effects, such as detector and electronic cross-talk, or pickup from external sources. Coherent noise can also be mimicked by uniform pedestal inaccuracies. Very small coherent noise contributions can degrade the resolution significantly, as will be shown in the following discussion.

Below we derive the contributions to the r.m.s. error of a variable S_i that sums the signals of N_{ch} channels on the i^{th} event. Let:

$$S_i = \sum_{a=1}^{N_{ch}} x_i^a, \tag{77}$$

where x_i^a is the signal in the a^{th} channel measured on the i^{th} event. The error on S_i is given by:

$$\delta S_i = \sum_{a=1}^{N_{ch}} \delta x_i^a, \tag{78}$$

where

$$\delta x_i^a = {}_p x_i^a(\text{observed}) - {}_n x_i^a(\text{noise off}). \tag{79}$$

Here, ${}_p x_i^a$ is the observed signal in the a^{th} channel on the i^{th} event, and ${}_n x_i^a$ is the signal that would be seen in the same channel with the noise in the system turned

off. The variance in S is then given by:

$$< \delta S^2 > \equiv S_T^2 = < \sum_{a=1}^{N_{ch}} \sum_{b=1}^{N_{ch}} \delta x_i^a \delta x_i^b >$$
$$= \frac{1}{N_{ev}} \sum_{i=1}^{N_{ev}} \left[\sum_{a=1}^{N_{ch}} \sum_{b=1}^{N_{ch}} \delta x_i^a \delta x_i^b \right], \quad (80)$$

where N_{ev} is the number of events.

It is useful to evaluate Equation (80) explicitly, keeping track of the diagonal and off-diagonal terms:

$$S_T^2 = \frac{1}{N_{ev}} \sum_{i=1}^{N_{ev}} \left[\sum_{a=1}^{N_{ch}} ({}_p x_i^a - {}_q x_i^a) \right]^2$$
$$= \frac{1}{N_{ev}} \sum_{i=1}^{N_{ev}} \sum_{a=1}^{N_{ch}} ({}_p x_i^a - {}_q x_i^a)^2 +$$
$$\frac{1}{N_{ev}} \sum_{i=1}^{N_{ev}} \left[\sum_{a,b,a \neq b} ({}_p x_i^a - {}_q x_i^a)({}_p x_i^b - {}_q x_i^b) \right]. \quad (81)$$

We define:

$$S_T^2 = S_I^2 + S_C^2 \quad (82)$$

where S_I is the incoherent contribution to the noise, and S_C is the coherent contribution, each given by:

$$S_I^2 = \frac{1}{N_{ev}} \sum_{i=1}^{N_{ev}} \sum_{a=1}^{N_{ch}} ({}_p x_i^a - {}_q x_i^a)^2 \quad (83)$$

$$S_C^2 = \frac{1}{N_{ev}} \sum_{i=1}^{N_{ev}} \left[\sum_{a,b,a \neq b} ({}_p x_i^a - {}_q x_i^a)({}_p x_i^b - {}_q x_i^b) \right]. \quad (84)$$

We also define a matrix of dimension N_{ch}^2, the elements of which describe the correlations between the a^{th} and the b^{th} channels:

$$S_{ab} = \frac{1}{N_{ev}} \sum_{i=1}^{N_{ev}} ({}_p x_i^a - {}_q x_i^a)({}_p x_i^b - {}_q x_i^b). \quad (85)$$

The diagonal elements S_{aa} give the square of the individual channel σ's for the a^{th} channel. With $\sigma_{aa}^2 = S_{aa}$, use of Equations (83) and (85) gives:

$$S_I^2 = \sum_{a=1}^{N_{ch}} \sigma_{aa}^2. \tag{86}$$

This is as expected: random noise, by definition, adds incoherently as the sum of squares: the total incoherent noise is a sum in quadrature of the individual channel σ's. The off-diagonal elements describe the coupling between channels a and b: a significant number of events for which both channels undergo positive excursions from their means will result in a large positive value of S_{ab}. Similarly, anti-correlations would result in a large negative value for S_{ab}. The matrix S_{ab} is seen to be symmetric: $S_{ab} = S_{ba}$.

In practice, the off-diagonal elements S_{ab} are often found to be proportional to the diagonal elements, so that:

$$S_{ab} = C_{ab}\sigma_{aa}\sigma_{bb}. \tag{87}$$

The C_{ab}, called the correlation coefficients, vary from -1 to $+1$, and are used to quantify the correlations between the a^{th} and the b^{th} channel:

$$C_{ab} = \frac{S_{ab}}{\sigma_{aa}\sigma_{bb}} = \frac{1}{N_{ev}} \sum_{i=1}^{N_{ev}} \frac{({}_p x_i^a - {}_q x_i^a)({}_p x_i^b - {}_q x_i^b)}{\sigma_{aa}\sigma_{bb}}. \tag{88}$$

$C_{ab} = +1$ implies totally correlated noise between the channels a and b, while a value of -1 implies full anti-correlation.

We perform the following sums:

$$< S_I^2 > = \sum_{a=1}^{N_{ch}} S_{aa} = N_{ch} < S_{aa} > \tag{89}$$

$$< S_C^2 > = \sum_{a,b,a\neq b} S_{ab} = N_{ch}(N_{ch} - 1) < S_{ab} > \tag{90}$$

where $< S_{aa} >$ and $< S_{ab} >$ are the average diagonal and off-diagonal elements, respectively, and are given by:

$$< S_{aa} > = \frac{1}{N_{ch}} \sum_{a=1}^{N_{ch}} S_{aa} \tag{91}$$

$$< S_{ab} >= \frac{1}{N_{ch}(N_{ch}-1)} \sum_{a,b,a\neq b} S_{ab}. \tag{92}$$

The coherent noise exceeds the incoherent noise when:

$$< S_C^2 > > < S_I^2 > \tag{93}$$

In practice, however, the $< S_{aa} >$ and $< S_{ab} >$ are calculable directly from Equations (91–92) and (85), making condition (93) more useful in the following form:

$$\frac{< S_{aa} >}{< S_{ab} >} = N'_{ch}. \tag{94}$$

The ratio of the average diagonal element to the average off-diagonal element, for total noise consisting of equal contributions from its coherent and incoherent parts, is equal to the number of channels summed. It is useful in practice to apply Equation (94) in the following alternative manner: the ratio of the average diagonal to the average off-diagonal elements, calculable from the data, gives the number of channels N'_{ch} that can be summed before the coherent noise becomes equal to the incoherent noise. The ratio on the left hand side of Equation (94), then, provides the figure of merit for quantifying coherent noise.

The importance of understanding and controlling coherent noise lies essentially in Equations (89) and (90): letting $< S_{aa} >= \sigma^2_{inc}$ and $< S_{ab} >= \sigma^2_{coh}$, we find (for large values of N_{ch}):

$$< S_I >= \sqrt{N_{ch}} \cdot \sigma_{inc} \tag{95}$$

$$< S_C >= N_{ch} \cdot \sigma_{coh}. \tag{96}$$

The incoherent noise scales like $\sqrt{N_{ch}}$, while the coherent goes like N_{ch}. In summing large numbers of channels, therefore, coherent noise can dominate the error in the total energy sum even though the per-channel value is much smaller than the incoherent one.

The incoherent contribution to the error in the total energy sum in the calorimeter is $\approx$ 10 GeV. The example in which pedestals are uniformly biased by +0.1 counts introduces effects which are identical to coherent noise, and results in an error in the total energy of $\approx$ 18 GeV energy deposit, an unacceptably large number. This 0.1 counts, which is $\approx$ 1 to 2% of a typical individual channel σ, is significantly smaller than the individual channel incoherent noise. The random noise, a result of inherent electronics and detector characteristics, cannot be improved upon. It therefore sets the scale for additional noise sources: one would like to keep the coherent noise well below the incoherent contribution. A jet covers roughly 1/30 of the detector, and an electron shower only $\approx$ 10 channels in total. In a 3-jet event that has been zero-suppressed, roughly 10% of the detector is summed, giving $\approx$ 1.8 GeV error in the energy measurement resulting from coherence in this example. For electrons, the effect is negligible. In general, the fact that only a fraction of the detector is included in event energy determinations helps contain the problem. In addition, there is strong evidence [62] that any coherence in the D0 calorimeter is likely to be limited to single preamplifier boxes, reducing the error on the total energy by $\sqrt{12} \approx$ 3.5. With this factor the error in the total energy falls to $\approx$ 5% of that introduced by the incoherent term for a 0.1 count pedestal inaccuracy. We believe that a level of coherent noise such that N'_{ch} in Equation (94) is $\gtrsim$ 1500 is acceptable.

The coherent noise "source" in the above example (i.e., pedestal bias) results in complete detector coherence. For physical sources, this is an unlikely situation: it is more probable that the coherent sources in practical situations will result in coherent noise in a portion of the detector (e.g., localized pickup of an external source.) Full coherence across the detector results in no error in transverse momentum, but partial coherence may. [6] Errors in total energy persist in either case.

In practice, decoupling the noise from the signal on an event-by- event basis is impossible: a given measure of the signal contains both the fluctuations from the

[6] Full coherence introduces no net P_t, as the energy within a cone of a given radius at a given angle is exactly cancelled by the energy in a similar cone 180 degrees (in both θ and ϕ) away.

signal (i.e., the intrinsic detector resolution, intrinsic particle width, etc.) and those from the noise. In order to have the ${}_qx_i^a$ (signal in the absence of noise) well-defined and measurable on an event-by-event basis, it is desirable to measure the coherent noise when there is no signal in the calorimeter. Pedestal-subtracted pedestal runs provide us with such an opportunity: for this class of events, the ${}_qx_i^a$ are all = 0, which provides us with the most accurate measure of the coherence, and the noise calculations are somewhat simplified as well.

Coherent noise for the D0 calorimeter had been studied in partial test systems prior to the Commissioning Run, but the run offered us the opportunity to investigate such effects in the fully installed central calorimeter. The detector was in an electronic environment that was as close to the final one as had been seen to that point. All four quadrants of electronics were powered up, and fully connected to the internal modules. External systems (muon electronics, central tracking signal cables, high and low voltage feeds, conductive piping for water cooling) approximated the final setup. Our group at NYU was responsible for the grounding and shielding of the signals from the modules to the BLS's; we therefore had a special interest in studying the system noise. It was believed that, should the system be susceptible to oscillations (a coherent effect), it might very well be seen at this point.

The left hand side of Figure (22) shows a plot of the correlation coefficients for one ADC in the northwest quadrant of the central calorimeter obtained during the Cosmic Ray Run. The mean is consistent with 0, the width is quite narrow, there is no anomalous structure, and it is symmetric – there is no evidence of overall positive or negative channel-to-channel correlations in any portion of this ADC. The plot shows a maximum coefficient of $\pm$ 0.20. In order to see directly the effects of coherent noise as represented by these plots, an artificial noise source was introduced into the detector: a pulse generator was used to pulse a heater wire entering the cryostat, with a repetition rate of $1/\tau$ (τ = 2.2 μsec, our sampling time), or $\approx$ 500 kHz. The plot on the right in Figure (22) shows the correlation coefficients that result in the same quadrant when such a noise source is introduced. The small

satellite peak at the right is the result of correlated noise in those channels affected by the pulser. The correlation coefficient plots under normal conditions (i.e., with no noise source introduced) were similar in other quadrants, as were the results with the muon toroid fully powered. The ratio $< S_{aa} > / < S_{ab} >$ (as given by Equation (94)) over all ADC's in the northwest quadrant was $\approx$ 1840, which was as good as had been seen in D0 test beams and initial tests of the final CC module array. With the noise source introduced, the same ratio was $\approx$ 25 channels.

The results, overall, were very encouraging, with no evidence of appreciable levels of coherent noise. Placement of the detector in the colliding beam environment might yet produce non-negligible coherent effects in the calorimeter; noise levels will thus be studied when D0 is in position for collider running.

Calibration Pulser

Although one of the real advantages of liquid argon ionization mode calorimetry is the identical response of every gap to charge deposited in it, this ideal situation is in practice compromised by variations in gain of the electronics. For optimum utilization of the calorimeter information, this gain variation needs to be corrected. Several examples of the sources of such variations are described below.

The combination of the detector capacitance, C_D, and the effective input resistance of the preamplifier (see Figure (17)) produces a capacitance-dependent rise time of the calorimeter signals. The difference between the largest and smallest values of capacitance in the detector is about 5 nanofarads, producing a maximum difference in signal rise time of $\approx$ 200 nanoseconds. Because the peaks of all the signals are sampled at the same time with respect to particle passage through the detector, this difference results in (for identical amounts of charge deposited in each cell) a capacitance-dependent, and hence channel-to-channel, variation in the measured signal.

Another capacitance-dependent variation in signal comes from the sharing of the charge between the capacitance to ground at the input to the preamplifier ($C_{in} \approx$ 19 nanofarads) and the detector capacitance. With this correction, a more accurate

formula describing the output voltage of the preamplifier (see Equation (64)) reads:

$$V_{out} = \frac{Q_{in}}{C_F} \cdot \left(\frac{C_{in}}{C_{in} + C_D} \right). \tag{97}$$

The correction factor, $\frac{C_{in}}{C_{in}+C_D}$, is about 0.92 for EM1 channels, and decreases to $\approx$ 0.77 for FH channels. It thus results in a sizable capacitance-dependent variation in the voltage level at the output of the preamp, for a fixed Q_{in}.

The preamplifiers also have intrinsic gain variations one would like to correct for. Any drifts in the system over time, independent of their cause, will also effect the overall integrity of the data; these should be corrected for as well.

Without correcting the data for the first two effects above, the response of the calorimeter would vary strongly as a function of capacitance. Signals in the low (EM) and high (FH) capacitance channels, even for a fixed Q_{in} in each, would be quite different. Even within a given layer, where the channel-to-channel differences in total capacitance can be 500 picofarads or more (for the FH layers), the spread in gain would severely compromise the resolution of the detector. To study the physics at the level we seek, all the above effects, including variations in preamplifier gain and system drifts, must be properly corrected for.

For the D0 calorimetry, gain corrections are made by the application of data taken with a precision pulser. The pulser produces a voltage pulse that results in the injection of a nominally identical amount of charge to every preamplifier. This pulse is designed so as to induce a response in the preamp that is, in principle, identical to that of calorimeter signals. The gain variations are exhibited by both the pulser signal and the data in an identical way. The pulser data, then, contains the information as to how much the real signal varies from channel-to-channel for a fixed amount of charge. Dividing the ADC output from the real signal by that from the pulser for that channel puts all channels on an equal footing. These gain-corrections, however, provide no information regarding an overall calibration (i.e., a conversion from ADC counts to energy deposited in the calorimeter); they provide only a relative channel-to-channel calibration. All data is pedestal-subtracted and

gain-corrected prior to (or during) analysis.

Figure (23) shows the signals resulting from the input of a fixed amount of charge at the input to the preamps of channels with 3 different values of detector capacitance (1, 2.7, and 4.7 nanofarads), at the output of the BLS as a function of sampling time. The data was taken during our first test of 5000 channels at Fermilab. All curves are normalized to the 1 nanofarad signal at its maximum value, which occurs at $\approx$ 2.8 μsec. [7] At our nominal peak sampling time of 2.2 μsec, there is $\approx$ 5% reduction of the 2.7 nanofarad signal with respect to the 1 nanofarad one, and $\approx$ 15% reduction of the 4.7 nanofarad signal. This gives the order of magnitude of the capacitance-dependence of the signal, and of the correction the pulser provides. The same 5000 channel test found that the pulser provided the same charge to the different preamps in a given preamp box to the 0.2% level. Its stability over an 18 day period was found to be better than 0.4% [58].

The bottom half of Figure (21) shows a plot of the mean of the channel-by-channel averages for EM4 of the pulser runs during the Cosmic Ray Run. It shows a stability of $\approx$ 0.3%. It should be mentioned that the gain of the preamplifiers have been found to be dependent on temperature at the level of $\approx$ 0.05%/deg C. The temperature of the preamplifier boxes, measured during the data taking by the D0 monitoring system, was found to vary $\approx \pm$ 1.5 deg C, and therefore accounts for $\approx$ 0.15% of the measured pulser instability. There is also a $\approx$ 0.03%/deg C gain change with temperature at the BLS which contributed $\approx$ 0.06% to the variations in gain during the run. Most of the instability in the pulser during the run, then, can be ascribed to temperature variations in other parts of the system. It is suspected that temperature variations in the room which houses the pulsers could be responsible for the remainder.

The above plots give one a feeling for the overall gain drifts that might be expected during a run. It is important to remember, however, that the conditions

[7] The signal in the low-capacitance channel has risen to $\approx$ 98% of its full amplitude after 2.0 μsec.

under which the pulser data is taken should approximate those under which the data was taken. The pulser, then, needs to accurately reflect system drifts, and correct the data properly for such drifts. In this regard, the understanding of the frequency with which gain runs must be taken is similar in nature to that for pedestal runs: they both ought to be taken frequently enough to accurately represent the data-taking conditions, but infrequently enough so as to allow time for acquiring real events.

A major caveat that has to be introduced regarding pulser performance is that of its timing relative to the data. The accuracy with which the response of the electronics to the pulser mimics that of the data is crucially dependent on the relative timing between the two pulses. We have used SPICE, a software package that simulates electronic circuits, using the D0 electronics parameters as input, to determine the timing constraints that proper gain-corrections require. We have also used measurements wherever possible to verify this information. In order for the pulser to accurately correct the gain variations in the data, the center of charge of the pulser (while taking a pulser run) and the center of charge of the triangular data pulse (while acquiring data) should appear at the input to the preamp at the same time, relative to the peak sample time at the BLS. It has been found that their relative timing should be the same to within $\approx$ 50 nanoseconds in order for the data to be properly gain-corrected. If it is not, a further capacitance-dependent correction can be made that can compensate for this error. In trying to obtain a verification of our calibration from the cosmic ray muon data, these issues become extremely important. Much attention needs to be paid, therefore, to the timing of both the base and the peak, for both pulser and data signals. This is a topic of much concern in this study, and will be discussed in more depth in the following chapters.

CHAPTER VII

THE D0 COSMIC RAY COMMISSIONING RUN

The D0 Cosmic Ray Run took place from February through May of 1991. Data were taken with the central muon system, the full central tracking system (central and forward/backward drift chambers, transition radiation detector, and vertex chamber), and the central calorimeter. Approximately 235,000 events were accumulated, with formal data-taking extending from the end of March to the end of May.

For the most part, we commissioned those portions of the detector that were available and ready for data-taking. The assembly of such a large device is a complex task; those parts of the detector that were used in the run were installed on the platform in the assembly hall by around December of 1990. Because the end muon chambers (EF) were not quite finished, and to retain easy access to the other detector elements on the platform, the end muon system was not included. All of the central tracking detectors were ready for commissioning, with most of them having undergone beam tests and independent cosmic ray muon tests during the construction and final assembly phases. The end calorimeters were being assembled in the clean room during the run, and were not ready for the cosmic test. Portions of the calorimeter (both end and central) had been analyzed in test beams in test cryostats, but none of the full calorimeter arrays had ever been tested. In essence, then, this was the first time that representative pieces from all three major detector groups had been assembled for a coordinated run, and the first time the data-acquisition system would be used to acquire data with all three detectors simultaneously.

Day shifts were dedicated to individual detector calibrations, i.e., taking and studying of pedestal and pulser runs by each detector group independently. Evening and, when manned, owl (overnight) shifts were usually reserved for global data acquisition with all 3 detector groups.

Figure (24) is an event display of a muon passing through the detector, in side

view, generated during the data-taking of the Cosmic Ray Run. Energy deposited in the calorimeter is visible, as are hits about the track in both the central drift chamber and the outlying muon chambers.

Trigger

There were two relevant triggering schemes for the Cosmic Ray Run. In the scheme of most interest in this study, a piece of scintillator was placed in the beampipe of the detector, along the Z-axis. It was 1.75 inches wide (in X) by 102 inches long (in Z) and $\approx$ 0.5 inches high (in Y). Any cosmic ray particle energetic enough to pass through the material in both the upper muon iron and chambers and one-half of the calorimeter will reach the center of the detector. (The central detectors consist of comparatively little material.) Upon passing through the beam pipe scintillator (BPSc), charged particles produce scintillation light that propagates down the scintillator toward both ends. Two phototubes, placed at either end of the scintillator, convert the light to a voltage pulse, that is sent to fast logic units below the platform for processing.

The phototubes were required to receive a signal within 40 nsec of each other; signals in both phototubes that satisfied this criterion were said to have produced a BEAM coincidence.[8] This signalled the occurrence of an interesting event, and set the downstream trigger logic (see below) in motion. This BEAM coincidence was used alone to acquire the data during the latter part of the run, from which the results in this study were extracted. During the early portion of the run, a large array of scintillators was placed atop the upper (C-layer) muon chambers (total area $\approx$ 960 sqft). It restricted the sensitive trigger area in both θ (45 deg $\lesssim \theta \lesssim$ 135 deg) and ϕ (55 deg $\lesssim \phi \lesssim$ 125 deg), and was originally used in conjunction with the BEAM coincidence (TOP*BEAM) so that all muons triggered on were guaranteed

[8] The effective speed of propagation in scintillator is $\approx$ 6 inches-per-nanosecond – in 17 nsec, therefore, light can travel the full length of the BPSc. The 40 nsec is a loose requirement that the trigger be a result of a charged particle passing through the BPSc, reducing the contributions of random coincidences between the noise in both phototubes to bearable levels.

to have passed through the upper muon chambers, in addition to some portion of the tracking detectors and the calorimeter. There were also scintillators placed in the forward region of the detector, with their plane perpendicular to the Z-axis, to select muons that had passed through the forward/backward drift chambers. Since the acceptance of this array included very little of the calorimeter's active volume, no further discussion of it will be presented in this study.

It is instructive to calculate the rate expected through the TOP*BEAM coincidence circuit. Using the total flux per unit solid angle per unit horizontal area about the vertical direction for the hard component of the cosmic ray spectrum (as given in Chapter IV), along with the appropriate geometric factors, the expected rate can be computed:

$$\begin{aligned} (\text{Rate})_{T*B} &= (\text{Flux}) \times (\text{area BPSc}) \times (\text{solid angle subtended by TOP scintillators}) \\ &\approx 13 \text{ Hz}. \end{aligned} \tag{98}$$

This must be corrected with an energy factor, describing that fraction of the incident flux energetic enough to make it through both the upper iron and the upper half of the calorimeter [63], giving a final result:

$$(\text{Rate})_{T*B} \approx 5 \text{ Hz}. \tag{99}$$

This is reasonably close to the $\approx$ 1 Hz rate as seen in the TOP*BEAM coincidence near the beginning of the run; some of the discrepancy was found to be due to problems with one of the fast logic units. Requiring only the BEAM coincidence gives a calculated rate of:

$$(\text{Rate})_{B} \approx 7 \text{ Hz}. \tag{100}$$

Our final measured rate for real BEAM triggers (i.e., triggers that reconstructed in the central drift chamber as real charged particle tracks) was $\approx$ 5 Hz. These order-of-magnitude calculations helped assure us that the trigger logic was working in a reasonable manner.

The geometry of the tracks imposed by the beam pipe scintillator is of interest. It produces tracks that are projective in ϕ: that is, the muons are restricted by the trigger to one or, at most, two ϕ units in each half of the calorimeter (depending on whether or not they start out close enough to a ϕ boundary, multiple scattering effects, etc.) The small width of the BPSc forces the muons to point to the beam line. The tracks, however, are not projective in η: tracks that do not pass through the vertex (Z=0) can routinely cross η boundaries as they pass through either half of the calorimeter. The above situation is an exaggerated version of that which occurs during collider running. The proton-antiproton collision is well restricted in the X and Y dimensions by focusing magnets in the beam line. In Z, the interaction region has a full width of $\approx \pm$ 30 cm, indicating that corrections to the projective geometry in η must be made. In any event, such crossing of η boundaries during the Cosmic Ray Run means that the signals from a single track can be shared with neighboring cells in the same layer. For the measurements of muon signals, with their small signal-to-noise, this has important consequences, which will be discussed at greater length in Chapter VIII.

Figure (25) shows a distribution of the tracks in Z at the beam pipe (X=Y=0), extracted from data acquired using the BEAM-only trigger during the run, as extrapolated from tracks reconstructed in the central drift chamber. The units are in centimeters, and the full length of the beam pipe scintillator is thus $\pm$ 130 cm on this scale. The distribution is not uniform; this was due to attenuation of the light along the scintillation counter. This non-uniformity does not effect the results, and was hence not included in the theoretical modelling of the data, described in later chapters.

This study focuses on data acquired with the BEAM-only trigger. Further discussion of the trigger will therefore be limited to this configuration.

Event Filtering

After much study, the voltage on the two beam pipe phototubes was left so that the the final rate (real tracks plus accidentals) was $\approx$ 15 Hz, about 2/3 of which

resulted from random coincidences from phototube noise. To trigger on such events would result in the logging of an enormous amount of "empty" events - events for which no muon had passed through the detector. A similar situation holds during collider running: logging every event for which a $\bar{p}p$ collision took place would result in the recording of much information containing little interesting physics. It would also require a system capable of logging such information at $\approx$ 100 Hz, beyond the current capability. Therefore, as mentioned in Chapter III, two levels of trigger, Level 1 and Level 2, are implemented.

The rates during collider running are such that the rate into the Level 1 is $\approx$ 50 kHz. The analogue of this during the Cosmic Ray Run was the rate for BEAM coincidences. This rate is sufficiently small so that everything was passed by the Level 1 trigger; no attempt was made here to select those events for which a track was present in the detector. Such selection was done in the Level 2 nodes.

The Level 2 is a network of microvax computers (nodes) that each contain filtering software for selection of potentially interesting events. The Cosmic Ray Run offered us the first opportunity to test this system, albeit at a much reduced rate. The filtering code that was utilized focused on the reconstruction in the central drift chamber. The $r - \phi$ position in the CDC is obtained from the wire information. As a charged particle passes through the central drift chamber, it ionizes the gas in the chamber. The electrons drift through the field created by high voltage applied to the sense wires, with the fields maintained at high enough values to induce proportional multiplication. The time difference between particle passage through the detector (computed from the time when the BEAM coincidence is made) and the collection of charge at a given wire is proportional, for a fixed drift velocity, to the distance the electrons drift through the field, and hence to the distance between the track and the wire. The different times obtained for the wires along the track is then translated into a distance profile, giving a nominal track position for each wire along the track.

Following a fit of the data in each half (upper and lower) of the chamber

independently,[9] a minimum of 5 out of the 7 wires in 3 out of the 4 layers of the chamber were required to have contributed to the fitted track information. If this criterion is met in either the upper or the lower half of the chamber (or both), the event is deemed to contain a cosmic ray track, and is passed on to the host computer for recording. The pass rate, or the percentage of BEAM triggers that contained a fitted track that passed the above criteria, was typically $\approx$ 28%. This rate was consistent with calculations of the expected accidental rate, as computed from the individual phototube rates and the combined discriminator widths. The Z-information, obtained from delay lines, was not used in the online filtering. In addition to its inferior intrinsic resolution ($\approx$ 3 mm), it was deemed to be unnecessary: a track passing through the chamber should nominally reconstruct in both dimensions. In the interest of speed and efficiency, the dimension offering the most reliable reconstruction and better resolution was used.

The central drift chamber provided invaluable information during the cosmic ray data-taking. Trying to obtain tracking information from the calorimeter is a difficult task, particularly when the signals involved are so close to the noise. Determining which cells have energy in them, and which are simply up-fluctuations of pedestals, is practically impossible for minimum ionizing signals without external tracking information. In fact, at the very beginning of the run, the calorimeter group had a very difficult time determining whether the device was working properly (or at all). It was not until the CDC and the calorimeter information were married that the first evidence of a working detector began to take shape. The tracking information from the CDC was used to point into the calorimeter to determine which cells were intercepted by the track. The calorimeter information was then extracted from this localized area. The routine and reliable use of the CDC information allowed for the successful analysis of the calorimeter's performance from the cosmic ray data, both

[9] A muon passing through both the upper and lower halves of the drift chamber is said to consist of two tracks: the upper and lower fits are treated seperately for each event. The acceptance is such that single-track events occur quite frequently.

on- and offline.

The fraction of the time our system was available for acquiring data during the Cosmic Ray Run (our "live time") was $\approx$ 30%. (This constraint was imposed by trigger and timing considerations.) The rate into the Level 1 was then $\approx$ 15 Hz/3, or $\approx$ 5 Hz. This is very close to the 1-2 Hz event-writing rate we are limited to. With the $\approx$ 28% pass rate for good events, the rate out of the Level 2 was then on the order of 1 Hz, which made effective use of our rate capability.

Timing

The primary difference between the timing of the signals used for data acquisition and transfer during collider running and that used for the Commissioning Run is the synchronization to the accelerator. The control signals for the front end data acquisition (e.g., base and peak, among others) are synchronized to the Tevatron's 3.5 μsec cycle time during collider running. The time of collision or, equivalently, the time defining particle passage through the detector, is periodic and well-defined, allowing the control signals to be timed with the same pre-determined periodicity. In particular, making sure that the base is sampled at the BLS as close as possible, but prior to, the rise of the signal, which is desired in order to obtain accurate measure of the baseline, and that the peak be sampled at the proper $\approx$ 2.2 μsec interval, becomes a relatively straightforward task. Cosmic rays, however, pass through the detector at random times. We were thus constrained to utilize such a synchronously-designed system in an asynchronous setting.

A primary problem for the calorimeter was the timing of the base to a signal which offers no prior indication of its arrival. The method finally implemented involved sampling the base every $\approx$ 5.2 μsec (our revised crossing interval used for the Cosmic Ray Run only), independent of whether a muon produced a trigger. For those crossings in which a trigger was seen, the baseline sampled for that crossing was used to subtract from the peak. The peak, however, as is always necessary, was timed to the rise of the signal; therefore, the time difference between the base and the peak varied from event to event. (This time difference is fixed when running

in collider mode.) The fluctuations in the voltage due to the uranium noise, which dominates the pedestal width, increase for longer sampling times. The width goes like the $\sqrt{\text{sampling time}}$, but the pedestal mean should be independent of such variations in sampling time. Systematic studies verified both of these expectations prior to running. It should be mentioned that all pedestal and pulser runs during the Cosmic Ray Run were taken under conditions identical to the data: a random trigger was used to simulate the asynchronous nature of the acquisition of the muon data. In this way, we were sure that the pedestal and pulser data reflected as accurately as possible the conditions encountered during data taking.

CHAPTER VIII

EVENT SELECTION AND DATA TREATMENT

To minimize systematic biases, we have chosen to restrict the analysis to non-zero-suppressed events. Channel-by-channel pedestal values can be evaluated on the same events as the data that is being analyzed for such a sample (as described in Chapter VI); this procedure allows for the correction of any intrinsic biases in the computation of the pedestal by CALIB, and corrects for drifts in the system that may have occurred between the taking of the CALIB pedestal run and the data-taking. In addition, we have opted for simplicity and consistency of the events to look at only those non-zero-suppressed events for which the muon toroid was not powered. This resulted in a final count of $\approx$ 12,000 event candidates.

For this class of non-zero-suppressed magnet-off events, the pedestals, as computed using the CDC information, were subtracted on a channel-by-channel and event-by-event basis. Gain-corrections were made with data from the calibration pulser that was obtained appropriately close in time to the data runs (see Chapter VI).

The Energy Variable

Since the ADC's measure the charge collected in the argon by the electronics, the pedestal-subtracted and gain-corrected ADC counts (henceforth called ADC′ counts) are proportional to the energy deposited in the argon, i.e., the visible energy. For this study, we choose visible energy as the variable of interest.

Since muons are highly penetrating and do not shower, converting from visible energy to total energy deposited (by applying the appropriate sampling fractions) offers no useful new information. Pulse height distributions in ADC′ counts, obtained on both an event-by-event and layer-by-layer basis, are therefore used to characterize the energy loss.

It should be stressed at this point that, although the distinction can be made between visible energy (ADC′) and total energy deposition (related to one another

by the sampling fraction), the units of each are arbitrary until a connection to reality (i.e., an energy scale conversion factor in, say, units of ADC'/MeV) is made. This subject is one of the main issues addressed in this study, and is discussed in detail in Chapters IX and X.

Roads from Central Drift Chamber Information

Directional information regarding the muons passing through the detector was obtained from the track reconstructed by the central drift chamber. Appropriate software routines used this information to point into the calorimeter along the direction of the track and provide the cells intercepted, on a layer-by-layer basis, by this extrapolated track. The net output of this procedure, then, provided a list, event-by-event, of the cells in the calorimeter that are expected to have been encountered by the muon as it passed through the detector.

Alignment uncertainties of the central drift chamber with respect to the central calorimeter, multiple scattering of the muon as it passed through the detector, and errors in the directional information provided by either the CDC or the track-extrapolation software can all contribute to uncertainties in this pointing procedure. One ultimately wants to know where the energy was deposited by the muon in the calorimeter – such uncertainties are addressed in the way the calorimeter data was treated, discussed in the following paragraphs.

Having obtained the above list of cells, a patch of 9 cells, 3 cells in the η direction and 3 along ϕ, was isolated in each layer for each event: the central cell of each patch was the one that the CDC information had predicted was the one the muon had passed through in that layer. For all but EM3, this results in a patch area of 0.3X0.3 in $\Delta\eta X\Delta\phi$ – the EM3 patch is twice as fine in each dimension. All subsequent analysis was restricted to this 3X3 patch in each layer. Because each layer is of finite depth (e.g., radial extent), a line drawn through the calorimeter can intercept more than 1 cell in a layer – we call this effect "sharing", as it represents muons that are expected to have deposited energy in more than 1 cell in a given layer. For events in which more than 1 cell in a given layer was intercepted by the

extrapolated track, we choose the one first returned in the list provided by the track extrapolation software as the central cell in the 3X3 patch. It should be mentioned that for all events, we require all channels in the 3X3 patch to be well-behaved on the basis of pedestal and gain information, and that all 9 cells are required to be full pads – no "clipped" edge pads, as exist in some layers at extreme $|\eta|$ boundaries, are permitted.

Figure (26) shows a superposition of the energy in $\approx$ 7000 events in EM1 for this 3X3 patch. The CDC information was used as described above to point into the calorimeter, and the superposition represents the energy sum of $\approx$ 7000 of these patches, located in different portions of the calorimeter on each event. The outer 16 cells are artificially suppressed to guide the eye, and an artificial offset of 1000 counts has been added to each of the inner 9. The central cell contains most of the energy, with those cells sharing a full border with the central one showing slightly enhanced energies. Sharing in the η direction is preferred over that in the ϕ direction: this is a result of our method of triggering. η boundaries are crossed routinely by incident muons, for a beam pipe scintillator with large acceptance in Z. The ϕ geometry tends to remain projective with such a trigger (see Chapter VII). Also, the resolution of the CDC track reconstruction in the $r-Z$ plane is inferior to that in $r-\phi$.

Event-by-Event Algorithms

Two natural algorithms might be used to characterize the energy deposited by the muon, event-by-event, in a given layer: the sum over the 9 cells, or the maximum pulse height in the 3X3 patch. Because the pedestal subtraction makes the mean energy of an empty cell equal to zero, the sum over the 3X3 area should be an unbiased measure of the muon signal. However, because the widths of the pedestals are close in magnitude to the width of the signal, such a sum has relatively poor resolution: summing 9 cells, of which only 1 or 2 contain muon signal, means that 7 or 8 cells, with their associated noise fluctuations, will be folded into the sum on each event, even though they contain no deposited muon energy.

In order to improve the resolution, an algorithm that picks out the maximum in

the 3X3 patch has been chosen. Since only one cell contributes noise fluctuations, the resolution is significantly better than that obtained by the summing method. However, the improved resolution comes with a price: the muon energy loss is, on some fraction of the events, misrepresented. There are two basic contributions to this misrepresentation: one is that resulting from pedestal up-fluctuations, and the other stems from the sharing effect.

The maximum pulse height, although quite likely to contain muon energy, can also represent events for which an up-fluctuation in a channel in the 3X3 containing pure pedestal (i.e., no muon energy) happened to result in a pulse height exceeding that channel's pulse height in which the muon energy was deposited. For this event, then, the pulse height chosen represents pedestal only, and contains no information regarding muon energy deposition. The likelihood of such an occurrence is least in layers for which the signal-to-noise ratio is best (see Table VI.1). In addition, sharing of the energy deposited by the muon in two adjacent cells in a given layer will bias the signal obtained: choosing the maximum will underestimate the total energy deposited when sharing occurs. The two effects are also coupled: events in which muon energy is shared will have an increased probability that a pedestal up-fluctuation in a cell containing no muon energy will have a higher pulse height than one which contains deposited muon energy.

The two resulting distributions, from taking the maximum and summing, are shown in Figure (27) for FH1. Both the peak and the mean of the spectrum resulting from the maximum is decidedly below that from the sum, and its width is $\approx 40\%$ smaller. The resolution (i.e., $\frac{\sigma}{mean}$) goes from $\approx 55\%$ for the summing algorithm to $\approx 37\%$ for the algorithm using the maximum.

Muon Selection by Range

It is desirable, for reasons elaborated on below, to select portions of the cosmic ray muon spectrum according to their energy. The calorimeter is deep enough that we can get some energy information from the range of the muon, which we have used for further cuts on the event sample.

As discussed in earlier chapters, the $\frac{dE}{dx}$ curve (expressed as a function of the incident muon energy) has a well-defined minimum, from which it increases rather softly (the relativistic rise, damped by the density effect) with increasing energy and more drastically ($\sim \frac{1}{v^2}$, the Bragg peak) with decreasing energy. The minimum for liquid argon occurs at an incident kinetic energy for muons of $\approx$ 270 MeV.

For verifying our energy scale and spectrum shapes by a theory-to-experiment comparison, it is convenient to restrict the sample to a region where $\frac{dE}{dx}$ varies slowly, i.e. the damped relativistic rise region. For this purpose, the event sample was restricted to include only those muons which produced a finite signal in the first lower fine hadronic layer (LFH1) of the calorimeter. A muon reaching the upper portion of LFH1 will have a minimum energy of $\approx$ 1.8 GeV entering the calorimeter from above, and a minimum energy of $\approx$ 300 MeV exiting the upper half of the calorimeter. The primary sample in this study examined pulse height spectra from the layers in the upper half of the calorimeter for the analysis, while requiring this cut in LFH1.

By adding an upper limit on range as well as a lower one, we can select a finite energy window. To do a study of events with well-defined energy, we selected a subset of the above events by requiring that the muons give no signal in the lower coarse hadronic layer (LCH). This sample, particles stopping in LFH1-3, has a muon energy range of $\approx (3.7 \pm 0.4)$ GeV – an energy window of $\approx \pm$ 10% – incident on the muon iron from above. For this sample, pulse height spectra from 12 layers of the calorimeter were examined, as we followed the track through both the 8 upper layers and the 4 lower electromagnetic ones.

Other Cuts

As mentioned in Chapter VII, the central drift chamber reconstructs tracks in its upper half and lower half independently: a through-going muon is considered, then, a "two-track" event. In order to select clean single-muon events, one and only one track was required to have been reconstructed in both its upper and lower half. In addition, the θ and ϕ information from the reconstructed track was used to require

that the upper and lower tracks be back-to-back (to within ≈ 0.4 radians in η, and ≈ 0.2 radians in ϕ), and thus represent a true through-going muon.

The muons enter the calorimeter at different angles. Muons of identical energies entering at different angles will therefore, by virtue of traversing different amounts of argon in the gaps, deposit different amounts of energy. A correction for the angle of incidence was made such that all track lengths in the argon were normalized to normal incidence: all signals resulting from muons entering the detector with angle θ (defined in the usual manner) were multiplied by $\sin\theta$.[10] Each signal, then, is placed on an equal footing with respect to every other one, and resulting histograms are then in the same currency.

The choice of the 3X3 unit as the appropriate patch size was not an arbitrary one. Of most importance is that the area be large enough that all of the muon energy is contained. Analysis of a subset of the event candidates was done, wherein patches of 5X5 were isolated and the outer 16 cells were summed, event-by-event and layer-by-layer. The results were consistent with no energy having spilled into the outer perimeter. On average in the 8 upper layers, the energy in these 16 cells was $(0.2 \pm 0.9)\%$ of the energy in the 3X3 region.

In order to help fortify the requirement that all energy remain in the 3X3 patch, we required 4 of the 7 layers other than the layer being considered to have its maximum pulse height in the middle of the 3X3 patch. This helps to select those events for which the muon was most likely to have deposited most of its energy in the central cell of the 3X3 patch in the layer under consideration, and thus will have deposited little or no energy outside the 3X3 boundary. We were able to make this cut only in the sample of tracks required to reach LFH1, due to the comparatively large size of this data sample.

Pulse height distributions for each of the 8 upper layers of the calorimeter were obtained for those tracks that were required to reach LFH1. After all cuts, the

[10] The track length needs no correction in the ϕ direction, as the module plates are perpendicular to the incident track in this dimension.

number of events that survived ranged from $\approx$ 1600 to 1700 events in each of the electromagnetic and fine hadronic layers, to $\approx$ 1000 events in CH.[11] For tracks that stopped in LFH, $\approx$ 400 to 450 events survived in upper FH and EM, and $\approx$ 200 in upper CH. Approximately 475 events contributed to the sample in each of the lower EM layers for this sample.

The distributions so obtained can now be compared to the theory, to which appropriate experimental effects have been folded in. This will be the subject of Chapter X.

[11] Some of the difference in the size of the event sample between CH and the other layers is attributable to a coarse hadronic beam by-pass module which, because of its smaller response compared to other CH modules, was eliminated from the analysis. It subtends 0.2 radians in ϕ, for all η, very near the vertical direction (+Y axis), where much of the cosmic ray muon flux is.

CHAPTER IX

ABSOLUTE ENERGY CALIBRATION

One of the goals of this thesis is the verification of the absolute energy calibration using the cosmic ray muon signal. ADC counts that have been properly gain-corrected put all signals on an equal footing: as previously mentioned, this gives only a relative (channel-to-channel) calibration. For all of the physics done with D0, an absolute energy scale is needed as well. Precision measurements of the W mass are an example of this, where an error in the overall energy scale translates into an uncertainty in the mass of the W. The goal of the absolute energy calibration is to obtain a conversion to a real energy scale, which can be applied to the output of the calorimeter electronics.

The energy scale of interest for this thesis is the visible energy, since we concentrate on the argon signal for our (non-showering) muons. For collider physics, on the other hand, what is useful is the total deposited energy (visible or not), since we would like to surmise the incident energy of all showering incident particles.

For either purpose, the energy scale conversion factor was obtained by two alternate methods: an *a priori* calibration, and a test-beam calibration. As we will see, however, the two methods are not of equal merit for the two applications.

A priori Calibration

In the *a priori* method, a known amount of charge is injected at the input to the preamplifiers at D0. Measurement of this charge is obtained by mapping out in detail on an oscilloscope the voltage pulse produced by the calibration pulser, from which the area of this pulse (in volt-μsec) is computed. The pulse is sent through a precision resistor, which produces a well-defined amount of charge at the preamp input.

Upon introducing this charge into the preamplifier, the electronics is read out in the normal manner. After gain corrections, this allows for the determination of the relationship between Q_{in} (the charge at the input to the preamplifier) and ADC'_{out}:

a given amount of charge at the preamp input produces some output voltage in ADC′ counts, which we measure through the same system as the data.

The major link in determining the *a priori* ADC′-to-MeV conversion hinges on establishing the relationship between the charge deposited at the preamplifier input and the amount of energy a particle traversing the detector deposits in the argon in order to liberate this same amount of charge. This is obtained from published experimental measurements of the relationship between energy deposited and charge produced in liquid argon (i.e., energy deposited per $e^- Ar^+$ pair - see Chapter VI) [60]. Thus, knowing the amount of charge that produced a measured number of ADC′ counts, and relating this same amount of charge to energy deposited in the gap, we can establish the *a priori* ADC′-to-MeV conversion factor, M_A:

$$M_A \left(\frac{\text{ADC}'}{\text{MeV}} \right) = \frac{(\text{ADC}' \text{ counts read out for charge } Q_{in})}{(\text{MeV deposited in argon gap for same } Q_{in})} \qquad (101)$$

The above outline gives the basic prescription for determining the slope for the conversion of ADC′ counts to MeV using the *a priori* method. There are a number of smaller effects that contribute to both the value and the error in M_A, which are described below.

Liquid Argon Impurity and Charge Collection

Impurities in the liquid argon reduce the amount of charge collected in the gap; liberated electrons are absorbed by electronegative contaminants (such as oxygen) in the readout material. Sufficient quantities of less electronegative substances (such as nitrogen) can also introduce some loss in the measured charge. Also, even for absolutely pure argon, a fraction of the charge is lost due to recombination prior to collection. The contribution to the value and error on M_A from these three effects, taken from our best estimates based on liquid argon purity monitoring studies and data (taken during the Cosmic Ray Run), give [67]:

$$(\text{oxygen contamination}) + (\text{nitrogen contamination}) + (\text{recombination})$$
$$= (3 \pm 1\%) + (2 \pm 1\%) + (5 \pm 2\%) \Rightarrow (10 \pm 3\%). \qquad (102)$$

The electron-absorption effects add linearly. Since our errors are independent, we opt to add them in quadrature.

Loss Due to Blocking Capacitor

The G-10 (a fiberglass/epoxy mixture in the module's readout boards) provides a capacitor that shields the preamplifier input from the high voltage applied to the resistive coat. Identical amounts of charge (1) injected directly into the preamplifier input and (2) produced in the argon gap, will give slightly different readout signals. Due to capacitive charge sharing, 6% of the charge produced in the gap is not collected: it remains on the blocking capacitor, and hence does not contribute to the signal read out. In order to produce the same signal in ADC′ counts at the output of the electronics, 6% more charge must be produced in the argon gap relative to that injected at the input to the preamplifier, and M_A must be reduced accordingly. We estimate a 1% contribution to the total error on M_A from this effect, which reflects primarily the variation in the thickness of the G-10 readout boards.

Other Uncertainties

Two more errors are relevant in the determination of M_A: (1) the number used to convert MeV deposited in liquid argon to the amount of charge deposited has an uncertainty of $\approx$ 2% [60], and (2) there is an error in the measurement of the area of the voltage pulse used to determine the amount of charge needed to produce a given response in the electronics.

The errors on M_A, taken together, yield:

$$\pm 2\%(\text{conversion of Q to MeV}) \pm 1\%(\text{effect of blocking capacitor})$$
$$\pm 2\%(\text{pulse area}) \pm 3\%(\text{argon impurity/recombination}) \Rightarrow 4\%, \qquad (103)$$

where we have added these uncorrelated systematic errors in quadrature. The final value for M_A is:

$$(3.75 \pm 0.16)\ \frac{\text{ADC}' \text{ counts}}{\text{MeV}}. \qquad (104)$$

We mention again that the *a priori* method relates ADC′ counts to visible energy

deposited in the argon (in MeV).

Test Beam Calibration

The D0 test beam run took place from early 1991 through January 1992. The apparatus consisted of a test calorimeter which contained modules identical to those that were used in the central calorimeter. The response of the test calorimeter to electrons of well-defined energies, as defined by bending magnets in the test beam line, was measured. The relationship between calorimeter readout and incident particle energy at the test beam could then be made. A "carry-over" established the relationship between the electronic gain at the test beam and that at D0. This allows one to deduce the correspondence between the measured electron signal and the incident electron energy at D0. The aim of the following paragraphs is to describe the logic and steps leading to an absolute energy calibration from the test beam data.

The Carry-Over

We can define the local units of visible energy in the i^{th} channel at D0 and the test beam (TB) in the following way:

$$ADC_i'^{TB} = K_i^{TB} \cdot ADC_i^{TB} \tag{105}$$

$$ADC_i'^{D0} = K_i^{D0} \cdot ADC_i^{D0}, \tag{106}$$

where the K_i are the calibration constants provided by the precision pulser, for the i^{th} channel, used for gain-corrections. The constants differ in the two places, and are therefore superscripted by location (TB or D0) as well as channel.

The electronics in the two places are not the same – different cable lengths, different preamplifier and BLS hybrids, etc., contribute to a difference in the signal in the two places: a fixed amount of charge deposited in the gaps of identical capacitance channels at the TB and at D0 will give different raw ADC output. We have used another pulser to establish the relationship between the electronics in the two places. This pulser is a portable unit, which allows for the injection of the same amount of charge into the preamplifiers at both D0 and the TB; as it establishes

something of a "standard" response in the two places. we call it the standard pulser (STD).

SPICE simulations (see Chapter VI) have suggested that the electronics for our calorimeter responds identically to a square pulse injected at the input to the preamplifiers as it does to the triangular pulse that results from charge collected in the gap. The response of the electronics to the standard pulser in the i^{th} channel, in ADC counts, is denoted by STD_i^{D0} and STD_i^{TB}. The same amount of charge is introduced at the preamp input in both places by the standard pulser (this will be elaborated upon later), which produces the desired square-shaped pulse. For the same fixed amount of charge deposited in the gaps at D0 and at the TB, the following relation holds:

$$\frac{ADC_i^{D0}}{\mathrm{STD}_i^{D0}} = \frac{ADC_i^{TB}}{\mathrm{STD}_i^{TB}}, \tag{107}$$

where ADC_i is the raw (non-gain-corrected) signal in the calorimeter resulting from this identical fixed amount of charge produced in the gap in both places. The above equation contains the crux of the calibration as obtained from the test beam carry-over: in units of the standard pulser output, the electronics response to the same amount of charge deposited in the gaps at D0 and at the TB is identical. The difference between the electronics in the two places is removed in the ratio.

Using Equations (105−107) above, the relationship between the local units of visible energy becomes:

$$\begin{aligned} ADC_i'^{D0} &= \left[\frac{\mathrm{STD}_i^{D0}}{\mathrm{STD}_i^{TB}} \cdot \frac{K_i^{D0}}{K_i^{TB}}\right] \cdot ADC_i'^{TB} \\ &\equiv \frac{1}{\beta_i} \cdot ADC_i'^{TB}. \end{aligned} \tag{108}$$

The K_i's are known from calibration runs taken in the respective places, and the STD_i's are quantities measured from data taken with the standard pulser in either place. Given an ADC′ reading in the i^{th} channel at the test beam, Equation (108) allows for the corresponding ADC′ reading in the i^{th} channel at D0. The β_i contain

all the information describing the differences between the electronics in the two places.

Total Energy Deposited at Test Beam

Equation (108) contains the relation between visible energy at D0 and at the TB. The known test beam energy, however, can only tell us the total deposited energy, forcing us to switch units.

An electron traversing the calorimeter deposits energy in more than one layer (and, in general, in more than one channel in each layer), with the total energy deposited equal to the sum of the total energy deposited in each of these channels. When computing the total energy deposited in the calorimeter, both the gain and the sampling fraction correction must be applied in order to put the signals read out from each channel on an equal footing:

$$ADC_i'' = \frac{ADC_i'}{SF_i}, \tag{109}$$

where ADC'' represents sampling-fraction-corrected ADC' counts. The total energy deposited, still in arbitrary units, for one event, is given by:

$$A = \sum_{i=1}^{N_{chan}} ADC_i'', \tag{110}$$

where the sum is over all channels containing energy deposited by the particle under consideration. The mean value over j events is given by:

$$< A >= \frac{1}{N_{evts}} \sum_{j=1}^{N_{evts}} A_j. \tag{111}$$

The measured calorimeter signal for an electron of a fixed energy in the calorimeter can be correctly represented, to within a constant, by Equation (111).

Using information from bending magnets in the beam, the energies of the incident electrons at the test beam are very well-known. Taking electron data at the test beam and treating it in the above manner, one can plot the incident beam energy as a function of $< A >$. Figure (28) shows such a plot as obtained at our test

beam. The slope of this plot, $S = \frac{d<A>}{dE}$, gives the expected relationship between gain- and sampling-fraction-corrected ADC counts at the test beam and total energy deposited in the calorimeter, in MeV. (Although the abscissa shows energy in GeV, we prefer the use of MeV units, and will refer to all energies in MeV.)

The relationship between the total energy deposited in the test beam calorimeter (in MeV) and visible ADC′ energy units is obtained by the use of the slope S and Equations (109) and (110), with appropriate TB supercripts:

$$
\begin{aligned}
{}_eE_{inc}(\mathrm{MeV}) = {}_eE^{TB}_{tot,dep}(\mathrm{MeV}) &= \frac{1}{S}\cdot A \\
&= \frac{1}{S}\sum_{i=1}^{N_{chan}} \frac{ADC_i^{\prime TB}}{\mathrm{SF}_i}.
\end{aligned}
\tag{112}
$$

where ${}_eE^{TB}_{tot,dep}(\mathrm{MeV})$ is the total energy deposited by an electron in the test calorimeter on a single event and the sum is over all channels containing energy deposited by the electron. ${}_eE^{TB}_{inc}(\mathrm{MeV})$, the incident energy of the electron as measured by the magnets in the beam line, is introduced in order to stress the equivalence, ignoring resolution effects, between the incident electron energy and the energy deposited in the calorimeter, when the calorimeter readout is treated by the prescription given on the right hand side of Equation (112). Since the total energy is equal to the sum of the energies in the different channels, we can write:

$$
{}_eE^{TB}_{i,dep}(\mathrm{MeV}) = \frac{1}{S}\cdot\frac{ADC_i^{\prime TB}}{\mathrm{SF}_i}
\tag{113}
$$

where ${}_eE^{TB}_{i,dep}(\mathrm{MeV})$ is the total energy, in MeV, deposited in the i^{th} channel at the test beam on one event. Equation (108), which provided a relationship between ADC′ at D0 and the TB, can be substituted into Equation (113) to obtain the relation between the energy deposited in the i^{th} channel at D0 (in MeV) and $\mathrm{ADC}_i^{\prime D0}$:

$$
{}_eE^{D0}_{i,dep}(\mathrm{MeV}) = \frac{1}{S}\cdot\beta_i\cdot\frac{ADC_i^{\prime D0}}{\mathrm{SF}_i}.
\tag{114}
$$

S, measured from test beam data, the β_i, which describe the differences between

the electronics in the two places, and the SF_i are all known.

Back to Visible Energy

Equation (114) gives us an expression for the conversion of visible energy in ADC′ units at D0 to the total energy deposited in a given channel of the calorimeter in MeV – this is what is of use for physics during collider running. In using the cosmic ray muons to verify this energy scale, we are interested in the visible energy deposited in the argon gaps. The visible energy is related to the total energy deposited by:

$$_{\mu}E_{i,vis} = {}_{e}E_{i,vis} \equiv E_{i,vis} = SF_i^e \cdot {}_{e}E_{i,dep}, \tag{115}$$

where SF_i^e is the sampling fraction appropriate for electrons in the i^{th} layer. Visible energy in the calorimeter is independent of the particle that produces it: the species of incident particle (in this case, electron or muon) becomes important when one attempts to describe the total energy deposited, where the appropriate sampling fraction needs to be applied. As described in Chapter III, the sampling fraction is defined using the energy deposited in the passive and active layers for minimum ionizing particles. The correct sampling fraction to use for electrons must be reduced relative to the mip sampling fraction by the $\frac{e}{mip}$ ratio:

$$SF_i^e = \left(\frac{e}{mip}\right) \cdot SF_i, \tag{116}$$

where, as before, SF_i is the sampling fraction for minimum ionizing particles.[12] Using this relation, we can write Equation (115) as:

$$E_{i,vis}(\text{MeV}) = \left(\frac{e}{mip}\right) \cdot SF_i \cdot {}_{e}E_{i,dep}(\text{MeV}) \tag{117}$$

or, substituting Equation (114):

$$E_{i,vis}^{D0}(\text{MeV}) = \left(\frac{e}{mip}\right) \cdot \beta_i \cdot \frac{1}{S} \cdot ADC_i^{\prime D0}. \tag{118}$$

[12]The expression for ADC_i'' in Equation (109) does not show this ($\frac{e}{mip}$) correction factor in its use of sampling fractions. This is because the ADC_i'' are proportional, to within a constant, to the total energy deposited. The sampling fraction is used, in converting from ADC′ to ADC″, only to put the different layers in the same currency, so that the sums performed in Equation (110) are valid and meaningful.

The above equation gives a prescription for converting from visible energy in ADC′ counts at D0 to visible energy in MeV deposited in the argon.[13] To be complete, it is in need of one more factor.

Relative Argon Impurities

The measured signal for electrons at the TB already reflects the reduction in signal due to argon impurities. What is important in carrying the calibration over from the test beam to compare it with muon data acquired during the Cosmic Ray Run is that the relative reduction in the signals in the two places due to argon impurities be accounted for. We call this factor Ω, and now write in full the final relation for the conversion of visible energy to a real energy scale at D0:

$$\begin{aligned} E_{i,vis}^{D0}(\mathrm{MeV}) &= \frac{1}{S} \cdot \beta_i \cdot \left(\frac{e}{mip}\right) \cdot \Omega \cdot ADC_i^{'D0} \\ &\equiv \frac{1}{\mathrm{M}_{TBC_i}} \cdot ADC_i^{'D0}. \end{aligned} \tag{119}$$

M_{TBC} is the visible energy scale factor, analogous to M_A, obtained by the test beam carry-over method. It remains to discuss some important details relating to the explicit evaluation of M_{TBC}, after which the appropriate numbers will be used to obtain a value and errors for M_{TBC}.

Timing Considerations and Layer Dependence

In order for the square pulse put out by the standard pulser to accurately simulate the data, it needs to be timed correctly. Much attention was paid to this during the standard pulser data-taking at both the TB and at D0. SPICE calculations have dictated that the center of charge of the square pulse must arrive at the preamplifier input at the same time that the center of charge of the triangular- shaped data pulse did during the data taking. The timing of the data (i.e., electron) pulse at the TB

[13] It is important to note that, implicit in some of the steps above, the sampling fractions in a given layer are assumed to be the same throughout the detector, both at D0 and at the test beam. Detailed measurements of electromagnetic module parameters, performed during module construction (e.g., uranium plate thicknesses and overall module height, at a number of η locations in each module), have shown this to be valid at the $\approx$ 1% level.

when the electron runs for the carry-over were taken should be identical to that of the STD pulse when the latter was used for the characterization of the test beam electronics (i.e., for determining the STD_i^{TB}). Similarly, in order to verify the calibration using muons acquired during the Cosmic Ray Run, the STD pulse should be timed properly to the triangular pulse as it was timed during the run. Timing scans were done at both locations, and this condition was satisfied.

In practice, the β_i are determined by taking a channel-by-channel ratio of data taken with the STD pulser and that taken with the calibration pulser. The calibration pulser is used in this manner to monitor drifts in the system: most sources of system drifts (e.g., temperature variations) will be common to both the STD and calibration output. It is desirable, but not essential, that the calibration pulser be timed in the same manner for this measurement as it is for those calibration runs used for gain-correcting the data. If this is true, and the calibration pulser was timed correctly for the data runs, no further capacitance-dependent corrections will be necessary. For the cases under study here, we found no evidence of the need for any additional capacitance-dependent corrections. This has the additional desirable consequence that the channel (or layer) dependence in the M_{TBC_i}, which is contained solely in the β_i, drops out. For identical amounts of charge at the input to the preamplifiers, if the gain-corrections are applied (i.e., timed) properly, all resulting gain-corrected signals should be the same - the β_i should be independent of capacitance. M_{TBC} will henceforth be considered to be independent of channel, and we will assume that one value will apply for all ADC'-to-MeV conversions at D0.

Determination of M_{TBC}

Our data indicates that β has an error of $\approx 2\%$, due primarily to instabilities in the pulsers (both the calibration and standard pulsers) that are in the process of being studied. Ω, the factor describing the difference in the signal reduction due to differences in argon impurities in the two places, has a value of (1.02 ± 0.01). The level of oxygen impurity in the two places was identical during the runs, but there

was nitrogen contamination that was present during the Cosmic Ray Run that was not present during the test beam running. The value and the error on Ω reflects this difference. The dominant error on M_{TBC} arises from the $\frac{e}{mip}$ ratio. We have chosen to use an experimental value determined for a calorimeter with slightly different geometry (3 mm uranium plates, 2 mm scintillator active layers) [31]. This value for $\frac{e}{mip}$ is 0.71. We have introduced a 10% error on this value, which encompasses many of the values in the literature, and includes our uncertainty in the effect the difference in the geometry and readout material have on this ratio.

Plugging in the above numbers for M_{TBC} gives:

$$M_{TBC} = (4.0 \pm 0.4) \frac{ADC'}{MeV}. \tag{120}$$

We recall that the value of M_A was $(3.75 \pm 0.16) \frac{ADC'}{MeV}$. It follows that:

$$\frac{M_{TBC}}{M_A} = 1.07 \pm 0.12. \tag{121}$$

The energy scale factors obtained by the two different methods agree within the error. This being the case, it is desirable to use the one with the smaller error. For the calibration of the visible energy in the calorimeter, M_A is therefore the scale factor of choice. Application of M_A to the cosmic ray data, and the subsequent comparison with theory, will be discussed in the next chapter.

Absolute Calibration for Collider Physics

We have stated a number of times that what is relevant for collider physics is the energy scale that relates the total energy deposited in the calorimeter to MeV. For use at D0, the absolute total energy calibration obtained from the test beam, Equation (114), can be used directly. The test-beam calibration is done by measuring the total energy deposited in the calorimeter by electrons at the test beam, and is applicable to the determination of the total energy deposited by electrons at D0. It will be noticed that this equation does not contain $\frac{e}{mip}$.

For the *a priori* calibration, on the other hand, the $\frac{e}{mip}$ ratio is needed to convert

	M_A	M_{TBC}
Visible Energy (ADC'/MeV)	3.75 ($\pm$ 4.3%)	4.0 ($\pm$ 10%)
Total Electron Energy (ADC''/MeV)	2.66 ($\pm$ 10.9%)	2.85 ($\pm$ 2.3%)

Table IX.1: The two absolute energy calibration constants for use with either visible energy or total electron energy. Units in each case are as shown; errors are in percent.

from visible energy to total deposited energy by electrons:

$$E_{i,dep} = \frac{E_{i,vis}}{\left(\frac{e}{mip}\right) \cdot \mathrm{SF}_i} = \frac{1}{\mathrm{M}_A} \cdot \frac{ADC'_i}{\left(\frac{e}{mip}\right) \cdot \mathrm{SF}_i} \quad (122)$$

$$\equiv \frac{1}{\mathrm{M}_A^{tot.dep}} \cdot ADC''_i, \quad (123)$$

where

$$\mathrm{M}_A^{tot.dep} \equiv \mathrm{M}_A \cdot \left(\frac{e}{mip}\right) \quad (124)$$

and ADC''_i is defined in Equation (109) above.

Thus, the large systematic error of $\frac{e}{mip}$ appears in the test beam calibration for visible energy (see Equation (119)), and in the *a priori* calibration for total energy. Table IX.1 summarizes the 4 calibration constants and their associated errors. The small error in M_{TBC} for total energy deposited helps to underscore the utility of the test beam calibration. For visible energy, which is the variable of choice in this study, however, we will use the *a priori* calibration.

Examination of the sources of the 2.3% error on M_{TBC} for total energy deposited makes it clear that our initial hopes of establishing an absolute electron energy calibration for physics of 1% using the test beam carry-over method are well within reach. 1% of this error is due to the error associated with the signal loss due to nitrogen contamination at D0 during the Cosmic Ray Run. The source of this problem has since been fixed: there should be no further nitrogen contamination in

our cryostat for the coming collider runs. Some of the remaining 1.3% is the result of pulser instabilities which, upon further study, should be understood and corrected for.

In the next chapter, we discuss the application of M_A to the cosmic ray muon data.

CHAPTER X

RESULTS

With the experimental data sample defined and the principles established for the generation of the theoretical distributions, we can now make the direct theory-to-experiment comparison. Two independent questions can be asked from such a comparison:

1. Do the shapes of the theoretical and experimental energy distributions match if we do not force the energy scale?

2. Does the energy scale we obtained in Chapter IX put the theoretical and experimental peaks in the same place?

The first question deals with the understanding of Landau fluctuations and resolution effects, while the second one tests the success of our energy calibration.

We will address both of these questions, on a layer-by-layer basis, in the sections below. In answering the second one, we will deal with the absolute energy scale as well as the layer-to-layer consistency of the calorimeter signal. Finally, we will present the energy scale comparison for a subset of muons stopping inside the calorimeter for which the incident energy is measured by the muon range.

Generation of Theoretical Spectra

The Landau theory as described in Chapter V allows for a full description of the spectrum shapes. Equations (56-62) describe the energy lost by ionization by a charged particle incident on a thin absorber. The predicted energy loss distributions can be obtained by application of these equations to the specific system under study.

The generation of the theoretical spectra is best described as a two stage process. The first involves the generation of the pure layer-by-layer signal distributions. These distributions contain the signal that would be seen in the liquid argon gaps of the calorimeter in the absence of resolution-broadening effects (such as pedestal fluctuations) or experimental biases (such as sharing). In reality, these effects do play a

role, so that prior to comparing the experimental and theoretical distributions, these experimental effects must be properly folded in to the pure signal distributions. The convolution of the experimental effects is the second of the two stages; each of these stages is described seperately below.

A Caveat

The Landau theory applies to a continuous medium: all energy lost in the thin layer of material is assumed to be fully sampled and detected. This includes the higher-energy delta-rays, that can travel long distances in the medium, leaving a trail of secondary ionization in their path. Such secondary ionization is part of the Landau description of the energy loss, and as such will be included in the energy deposition spectra obtained from the theory.

In sampling calorimeters, however, the contribution to the energy loss by these delta-rays is altered by "plate-effects": the readout layers are interrupted by absorber plates. Those delta-rays produced in the gap that are of sufficient energy to reach the absorber plates, and therefore deposit some of their energy in the uranium layers, will be only fractionally sampled by the calorimeter. Since these delta-rays are of relatively high energy, it is the tails of the distributions that are affected most by this inhomogeneity [31].

Full modelling of the energy deposition of muons in sampling calorimeters requires an extensive and quite complicated monte carlo. A full description would involve not only the correct treatment of delta-rays in the argon, but delta-rays in the absorber, and all of the non-ionization effects described in Chapter V – radiation, direct pair-production, and photonuclear reactions – in both the absorber and readout material, that manages to get sampled. Evidence suggests that these energy loss mechanisms also predominantly effect the tails of the distributions in sampling calorimeters [31].

Such a complete description has been considered for use in this study, and our conclusion is that such an approach would demand a prohibitive amount of time and effort to implement and understand. We therefore have chosen not to include these

"plate-effects" in our modelling of the ionization losses as predicted by Landau, and have also omitted the non-ionization losses mentioned above. We are thus choosing a "minimal" theory to see if it explains our data.

In order to obtain an accurate measure of the energy loss, we have chosen the most probable (or peak) of the distribution to characterize the distributions. This diminishes the effects of the tails that we believe are most affected by the processes we have not modelled, while still allowing for a well-defined description of the energy deposition.

Obtaining the Pure Theoretical Signal Distributions

We are interested in simulating the energy loss in the active layers of the calorimeter. The material-dependent parameters (n_e in the expression for ξ, and I in that for ϵ' - see Equations (56) and (59)) are well-defined, with the former being readily calculable and the latter available from tables [47]. The integral describing the universal function ($f_L(\lambda)$) can be evaluated numerically, at many different values of λ. A given incident energy defines all kinematic parameters in the theory (β and γ). Using all of the above, random numbers that have been generated according to the $\chi(W, x)$ probability distribution, give the value of the energy loss for a particle of a known incident kinetic energy in the argon on a given event. The energy loss distribution is the spectrum resulting from many such throws of the dice, each throw representing a value of the energy loss that varies statistically according to the Landau theory.

The minimum incident kinetic energy required for a muon to reach LFH1 is 3.3 GeV at the top of the muon iron, which is the point from which the $\frac{1}{E^2}$ cosmic ray differential energy spectrum must be referenced. Muons are generated according to this distribution at the top of the iron, and their energy is reduced by the mean $\frac{dE}{dx}$ in the toroid. This gives the appropriate energy distribution at the top of the cryostat.

The muons are then followed through the calorimeter on a plate-by-plate, gap-by-gap basis: their energies are reduced by the mean $\frac{dE}{dx}$ in the appropriate absorber

plate (either copper or uranium), and by the energy loss obtained from the Landau theory (as described by the procedure above) in the liquid argon gap. A particle entering a unit cell has kinetic energy E upon encountering the absorber. Its energy is $E' = E - < \frac{dE}{dx} > \cdot \Delta x$ upon exiting the plate and entering the argon, where $< \frac{dE}{dx} >$ is the mean $\frac{dE}{dx}$ of the muon in the appropriate absorber material, and Δx is the thickness of that material. In order to determine the energy lost in the argon gap, the dice are thrown according to the prescription described earlier, with the kinematic parameters corresponding to E'. The subsequent energy loss in that gap, $\Delta E'$, is computed. The energy is then reduced by the amount $\Delta E'$ upon entering the next plate, and the process is repeated throughout the calorimeter in the layers of interest. The measured signal is a sum of single-gap energy losses, and so the final readout signal in a given layer on a given event results from summing the losses in the appropriate number of liquid argon gaps for that layer. Since the experimental distributions have been corrected for their angle of incidence (see Chapter VIII), the theoretical modelling is done assuming the muons enter the calorimeter at normal incidence.

The above application of the Landau theory for our calorimeter gives the expected pure signal distribution, in MeV, in all layers of interest for the cosmic ray muons. We describe below the process of adding the experimental effects to these signal distributions, appropriate for making the experiment-to-theory comparison.

Introducing the Experimental Effects

The final theoretical distributions we have used to compare with the experimental data fold in the contributions from two additional effects: pedestal fluctuations and sharing. Random numbers are produced according to the appropriate pedestal and sharing distributions, with each of these distributions obtained on a layer-by-layer basis from the experimental data. Pedestal distributions are readily available from appropriate analysis of the off-track pedestals. The sharing distribution is obtained by establishing the number of cells in a given layer that are intercepted by the line projected into the calorimeter from the CDC information. Random num-

bers produced according to these distributions for each layer are applied in order to mimic the experimental situation.

We choose to compare the spectra obtained by the algorithm that picks out the maximum in the 3X3 patch. The significantly better resolution that characterizes these spectra results in theory-to-experiment comparisons that are more telling: the signal has not been obscured by the adding of many cells, each containing pedestal fluctuations. The summing algorithm, as mentioned in Chapter VIII, would result in a distribution of much poorer resolution, and hence is less useful for our purposes here.

For a given layer, then, the signal in each of the appropriate number of gaps is obtained from the Landau modelling. For each event, a random number is selected according to the sharing distribution for that layer, which describes what fraction of the gaps in that layer contribute to the signal in, say, cell A, and what fraction contribute to the signal in cell B. (The number describing the sharing therefore varies between 0 and 1.) Random numbers are also selected, according to the pedestal distribution in that layer, 9 times for each event, to represent the pedestals in the 9 cells that are considered in the 3X3 patch. The signal in cell A is added to 1 pedestal (chosen at random), the signal from cell B is added to a different one, and the maximum of these two resulting signals and the 7 other pedestal signals is determined. This, for that layer and that event, represents the signal which we enter into the theoretical energy loss spectra. The spectra so obtained from all layers of interest are those which we now use to compare to the experimentally-obtained distributions.

Comparison of the Experimental and Theoretical Spectral Shapes

Figures (29-32) show the results of our theory-to-experiment comparisons. In order to compare the two distributions, we have left the energy scale a free parameter in the theoretical spectra. The dotted distributions are the experimental distributions, and the solid are the theoretical ones. All units are in ADC′ counts.

Figure (29a) shows the comparison of the two distributions in EM3 when neither

pedestal fluctuations nor sharing distributions are folded into the theory. Figures (29b) and (30a) show the slight improvement when one or the other is introduced by itself. As is seen in Figure (30b), it is not until both effects are folded in that the theoretical distributions fit the data. The plots in Figures (31) and (32) show the resulting spectra, with both experimental effects folded in, for all electromagnetic and hadronic layers, respectively. The shapes of the experimental distributions are in good qualitative agreement with those from the theory.

Energy Scale

As discussed in the previous chapter, the most desirable absolute energy scale factor to use when describing visible energy is M_A ($M_A = 3.75 \pm 0.16$ ADC′/MeV). In order to obtain an energy unit common to both theory and experiment, we multiplied, on an event-by-event basis, the theoretical distributions described above by M_A. This gave the nominal expected energy loss distributions (again, layer-by-layer) in (expected) ADC′ counts.

A quadratic function was used to fit the distributions so obtained, with the region of the fit restricted to approximately half the peak height. The same fit was performed for the experimental spectra. From this, we have a value of the peak position for both the experimental distributions and the theoretical ones, in the same units. The ratio of the peak positions measures the level of agreement of our energy scale with the theoretical model. We have expressed the ratio as:

$$\frac{\text{Peak(experimental)}}{\text{Peak(theoretical)}} = \alpha. \qquad (125)$$

In short, α is the factor by which the energy scale M_A would have to be adjusted in order to obtain identical theoretical and experimental peak positions. A value of α = 1 means the two peaks agree perfectly.

Table X.1 shows the values of α for each upper layer of the calorimeter, as determined from the sample of tracks required to reach LFH1. The statistical error represents an addition in quadrature of the statistical fitting errors. The 2% systematic error results from two effects:

Layer	$\alpha \pm$ stat.error	syst. errors
UEM1	0.98 ± 0.02	
UEM2	0.96 ± 0.03	
UEM3	1.05 ± 0.02	
UEM4	1.06 ± 0.02	$\pm$ 2% (CR energies)
UFH1	1.18 ± 0.02	$\pm$ 4% (M_A)
UFH2	1.14 ± 0.01	
UFH3	1.12 ± 0.02	
UCH	1.18 ± 0.03	

Table X.1. Values of α for tracks required to reach LFH1. Values are for layers in upper half of calorimeter only. The errors are described in the text.

a. An assumed uncertainty of $\pm$ 100 MeV in the starting energy (the lowest possible energy for which a finite signal in LFH1 is obtained), which, in conjunction with the $\frac{1}{E^2}$ cosmic ray spectrum fall-off. results in an overall raising (+100 MeV) or lowering (−100 MeV) of the predicted signal in each layer;

b. The differential fall-off of the cosmic ray spectrum of $\frac{1}{E^2}$ depends on both energy and incident angle. The portions of the spectrum we are concerned with here fall as $\frac{1}{E^N}$, where N varies between 2 and 3 [68,71]. A portion of the 2% reflects this variation in the energy dependence of this fall off.

The 4% systematic error reflects the total uncertainty in M_A, as described in the previous chapter.

Layer-to-layer Signal Consistency

We can now ask whether the signal is the same throughout the different layers in the calorimeter. Given that the nominal gap widths are the same throughout the detector, and the gain-corrections remove any layer-to-layer differences in the expected signal, we expect all of the energy scales to be the same, within errors, in the different calorimeter layers. We use the above values for α in the different layers to test this expectation.

Table X.2 shows a summary of the results. <ALL LAYERS> is a weighted mean

<ALL LAYERS>	=	1.102 ± 0.006
<EM ONLY>	=	1.021 ± 0.011
<FH ONLY>	=	1.143 ± 0.008
<FH>/<EM>	=	1.12 ± 0.02

Table X.2. Signal consistency in the upper layers of the calorimeter, for those tracks that reach LFH1. Quantities are defined in the text.

of α for all layers, with <EM ONLY> and <FH ONLY> being the corresponding weighted average for the respective sections. The resulting <FH>/<EM> ratio, used conventionally throughout the collaboration, is as shown. We find a (12 ± 2)% difference between the response in FH and that in EM. There will be further discussion of this in the next chapter.

The Value of the Scale Factor M_A

The test of whether M_A has the correct absolute value is whether the α_i in Table X.1 agree with 1 within the combined statistical and systematic uncertainties. We interpret a significant deviation of the α_i from 1 as a discrepancy between the expected and observed energy scale in a given layer.

For all electromagnetic layers, the α_i are consistent with 1 within the errors: we therefore say that our energy calibration works for all of these layers. For the hadronic layers, the α_i differ significantly from 1 even after the systematic errors are added to the statistical ones, reflecting the <FH>/<EM> discrepancy described in the previous section. We therefore conclude that, within our model, the energy scale M_A works for the electromagnetic layers, and that it fails at about the 10% level for the hadronic ones.

Application to Stopping Particles

As described in Chapter VIII, a subset of stopping muons is chosen by requiring a finite signal in lower fine hadronic layer 1, and by also requiring there be no signal in lower CH. This sample, then, has stopped somewhere in the lower fine hadronic (LFH) layers. The incident energy at the top of the muon iron for such a sample is

(3.7 ± 0.4) GeV, giving a $\approx \pm$ 10% determination of the incident energy. We looked at those layers for which the energy loss is well-defined: all upper 8 layers of the calorimeter, and the lower electromagnetic sections, for a total of 12 layers.

Restricting the muons to this well-defined energy at the lower end of the cosmic ray muon energy range does not alter the results obtained above, as shown in Tables X.3 and X.4.

In conclusion, there is good qualitative agreement between the shapes of the theoretical and experimental spectra. The α_i obtained for both reaching and stopping tracks also agree with one another. The <FH>/<EM> response imbalance is evident in both samples. The α_i for the electromagnetic layers agree with M_4, but the hadronic ones do not. The latter α_i do, however, agree with one another.

Layer	$\alpha \pm$ stat.error	syst. errors
LEM4	0.97 ± 0.02	
LEM3	1.03 ± 0.02	
LEM2	1.01 ± 0.04	
LEM1	0.96 ± 0.10	
UEM1	1.04 ± 0.08	
UEM2	1.01 ± 0.08	± 2% (CR energies)
UEM3	1.10 ± 0.03	± 4% (M_4)
UEM4	1.05 ± 0.02	
UFH1	1.16 ± 0.05	
UFH2	1.14 ± 0.03	
UFH3	1.10 ± 0.03	
UCH	1.17 ± 0.05	

Table X.3. Values of α for tracks required to stop in LFH. Data from both the upper and lower EM layers are given.

<ALL LAYERS>	=	1.051 ± 0.009
<EM ONLY>	=	1.026 ± 0.010
<FH ONLY>	=	1.126 ± 0.020
<FH>/<EM>	=	1.10 ± 0.02

Table X.4. Signal consistency for tracks that stop in LFH. <EM ONLY> includes data from both the upper and lower EM sections.

CHAPTER XI

CONCLUSIONS

As shown in the previous chapter, the shapes of the theoretical and experimental distributions agree quite well. The agreement is better in the region of the peak than in the tails, as expected. Full inclusion of the experimental effects was necessary before the theory approximated the experiment well. That the fits in the peak were as good as they were indicates that good results can be obtained from the information in the peak region without modelling the "plate-effects". At the typical energy of our cosmic rays, the simple continuous medium Landau theory appears to be a good approximation to the energy loss in the active layers of our sampling calorimeter.

The two ways of obtaining the energy conversion scale, from measuring the charge sensitivity of our electronics (M_A), and from the test beam carry-over (M_{TBC}), agree well.

The good agreement of the experimental and theoretical shapes in the peak region makes the most probable energy a viable vehicle for checking this energy scale. One would expect this to be less true, in general, if one were to use the mean to characterize the Landau distributions, as the fluctuations in the tails greatly effect the mean. The peak appears to be insensitive to both the inhomogeneity of the medium and, at the typical energies we are interested in here, the losses due to radiation and other non-ionization processes.

The α_i obtained for the electromagnetic section agree with M_A. Those for FH and CH are $\approx$ 10% high, but they do agree with one another.

The <FH>/<EM> response imbalance has received much attention in the collaboration – our value for both samples is consistent with $\approx$ 10% difference in the response between the two. An effect of approximately the same magnitude and sign (<FH>/<EM> > 1) was seen at the test beam during tests of the central calorimeter modules. Beam tests of endcap calorimeter modules, however, did not exhibit

this response difference when studied at the test beam last year. The source of the effect in CC is still not understood; we have, however, done much work toward trying to understand it.

There are two possible sources of the problem that immediately leap to mind: one involves the capacitance-dependence of the gain corrections, and the other is related to module construction. As discussed in Chapter VI, if the calibration pulser and the data are not timed properly relative to one another, the gain correction will have a capacitance-dependent bias. The total capacitance of the FH channels is about a factor of 2 to 3 higher than those in EM. If the calibration pulser is timed incorrectly relative to the data, an <FH>/<EM> response imbalance is precisely what one would expect to see. This has been studied and measured at both the test beam and for the Cosmic Ray Run. In both cases, to the best of our knowledge, the timing was done properly. We believe one cannot blame the signal imbalance on the relative channel-to-channel calibration done with the calibration pulser.

The other suspected source is the module construction. If the liquid argon gaps in the FH and CH modules were, on average, uniformly $\approx$ 10% larger than those in the EM section, this would produce such a difference in the response. As far as we know, this possibility still appears to be the only alternative that has not been definitively disproved.

We believe that $\approx$ 1% calibration will be achieved using the test beam carry-over. For much of the physics we are concerned with for D0 (i.e., jet studies, top search), this is quite adequate. For precision measurements of the W mass, however, we would like to achieve a measurement to $\approx$ 0.1% or better. The W mass energy scale will have to be obtained from mass measurements of the Z.

Finally, we mention one of the most satisfying results of the Cosmic Ray Run: we were able to characterize a device designed for high mass physics using minimum ionizing particles, which are at the very low end of the dynamic range of the electronics. System instabilities, noise, and other fluctuations did not swamp the small muon signal, despite the low signal-to-noise ratio. The device worked re-

markably well, and running all systems together posed no insurmountable problems. All indications are that we have a detector that should work quite well for collider physics.

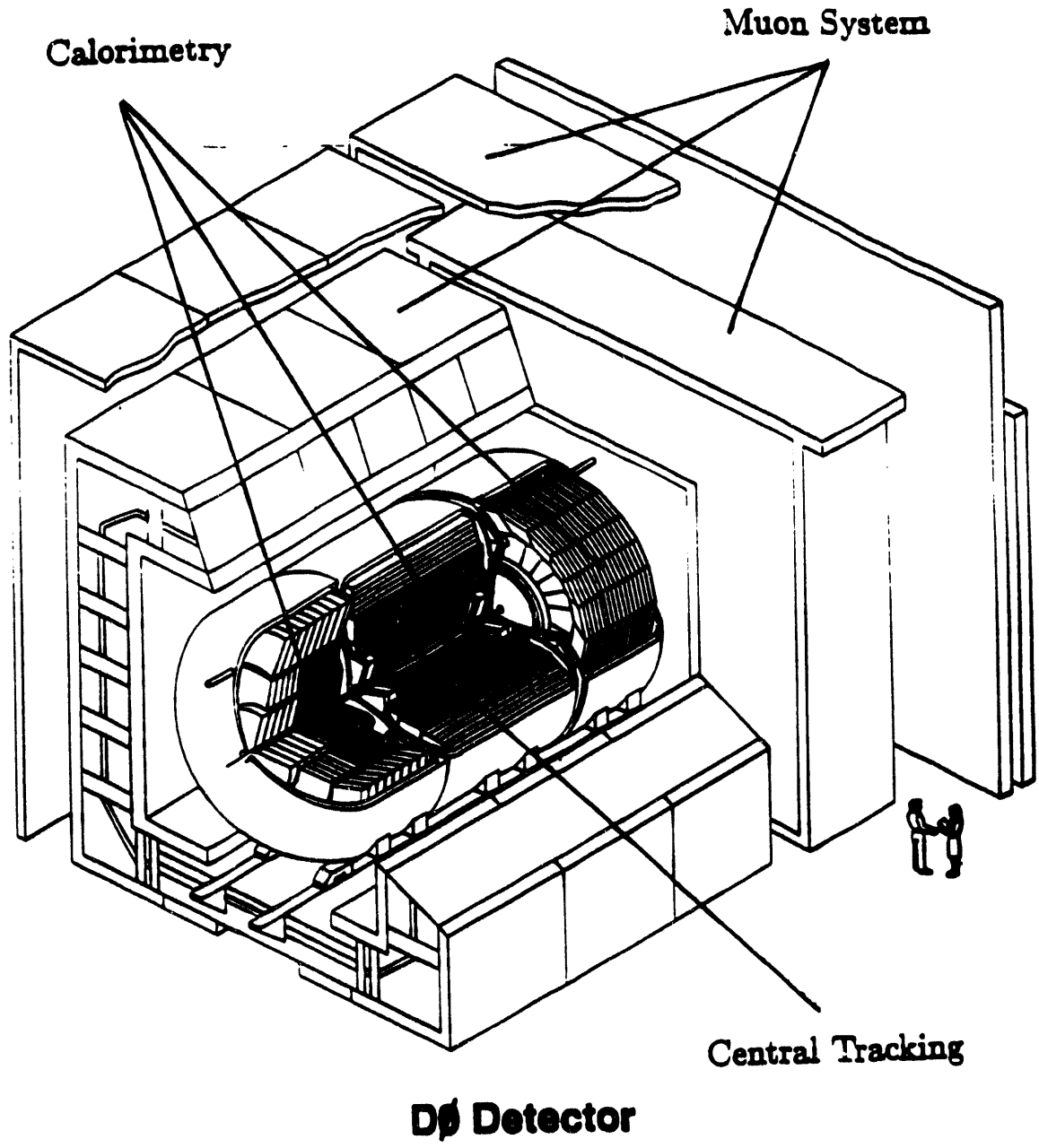

Figure 1: The D0 Detector: cutaway view. (from [16])

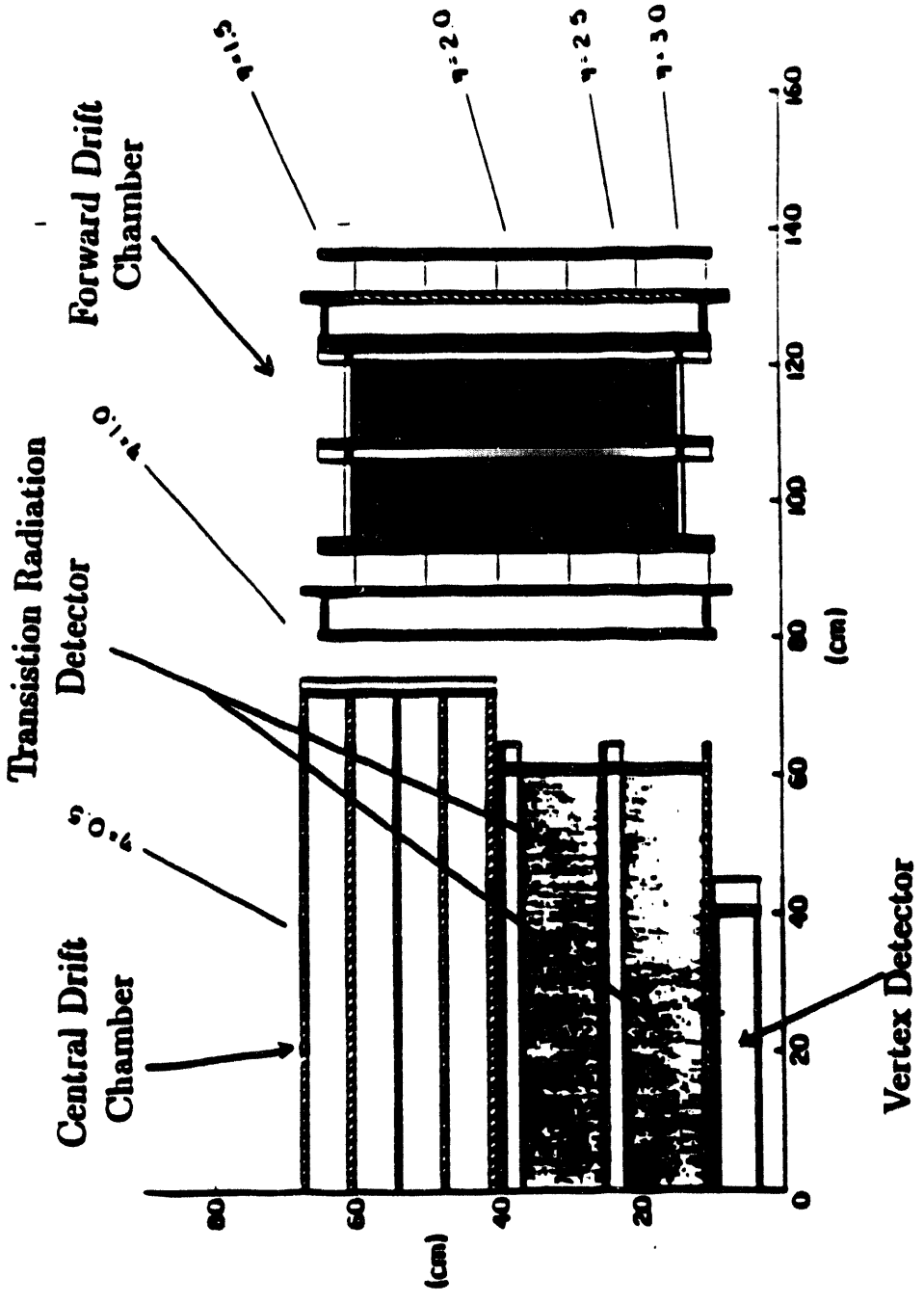

Figure 2: Cross sectional view of the D0 central tracking detectors in one quadrant of the r-Z plane. (The abscissa points along the physics Z-coordinate). (from [15])

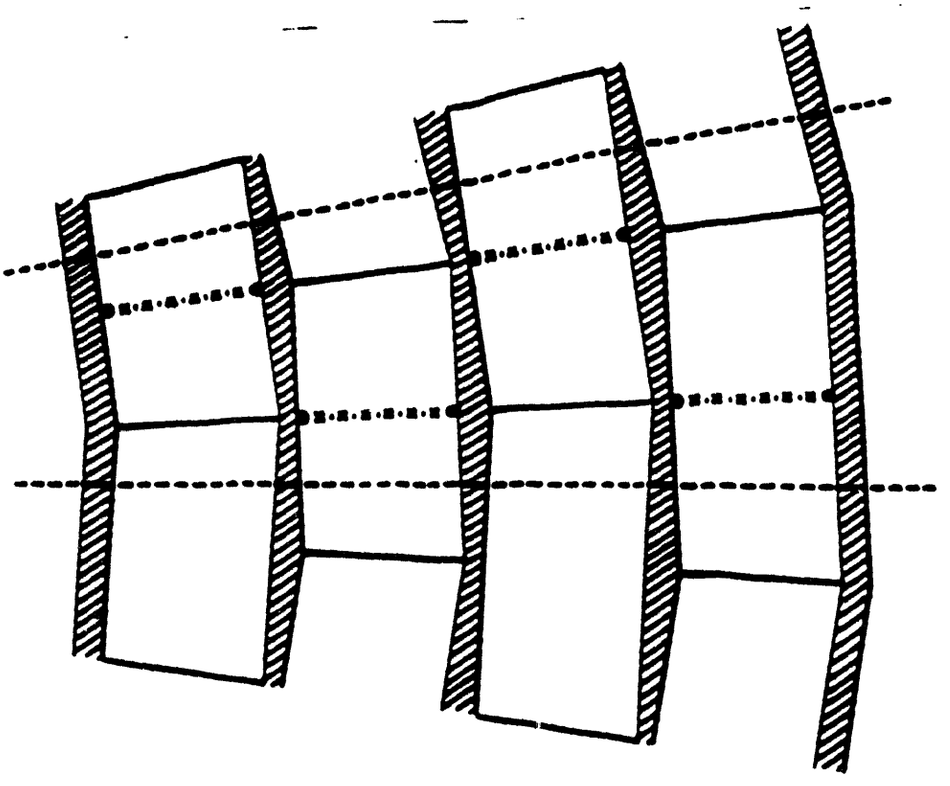

Figure 3: The wire arrangement within supercells of the central drift chamber. (x = sense wires, · = potential wires, o = delay lines.) View is in r-ϕ plane. (from [15])

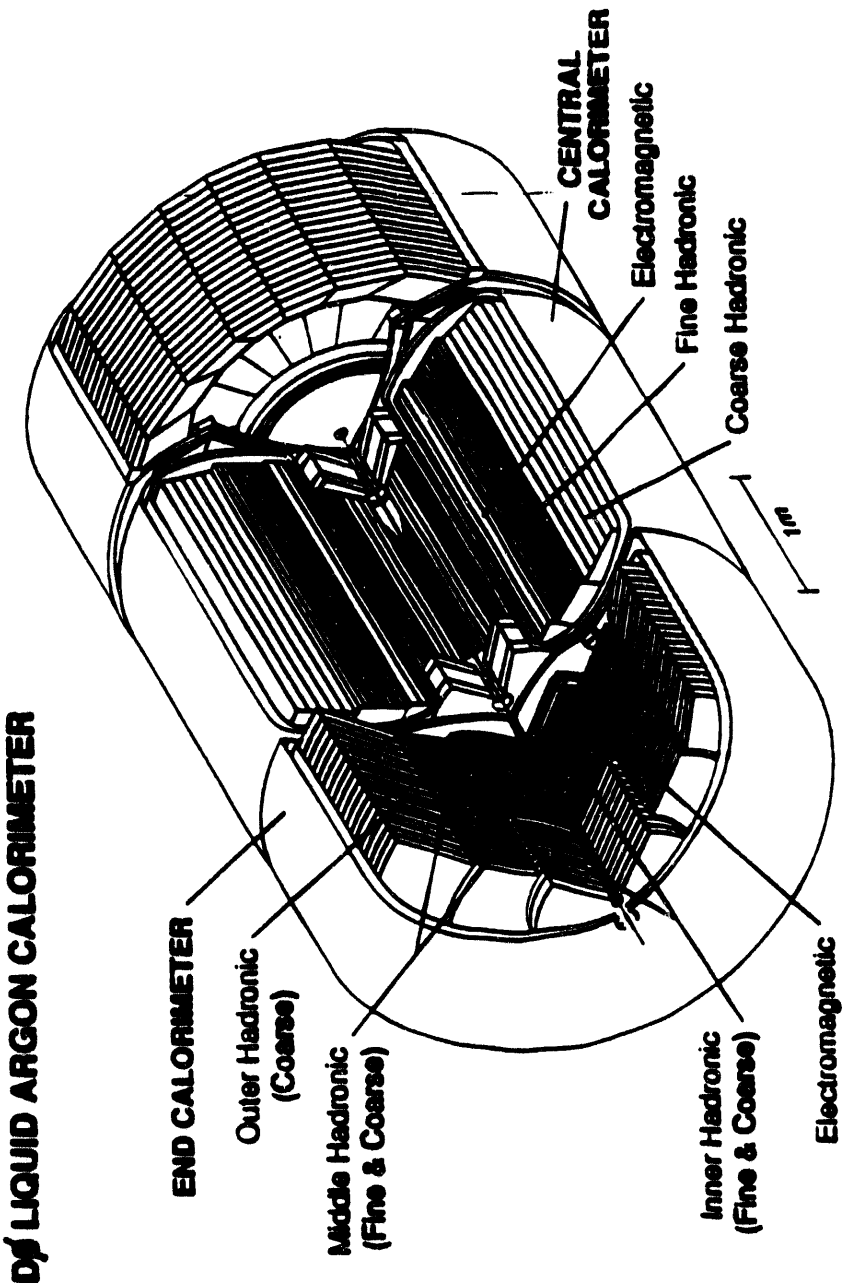

Figure 4: Cutaway view of the D0 calorimeters. (from [16])

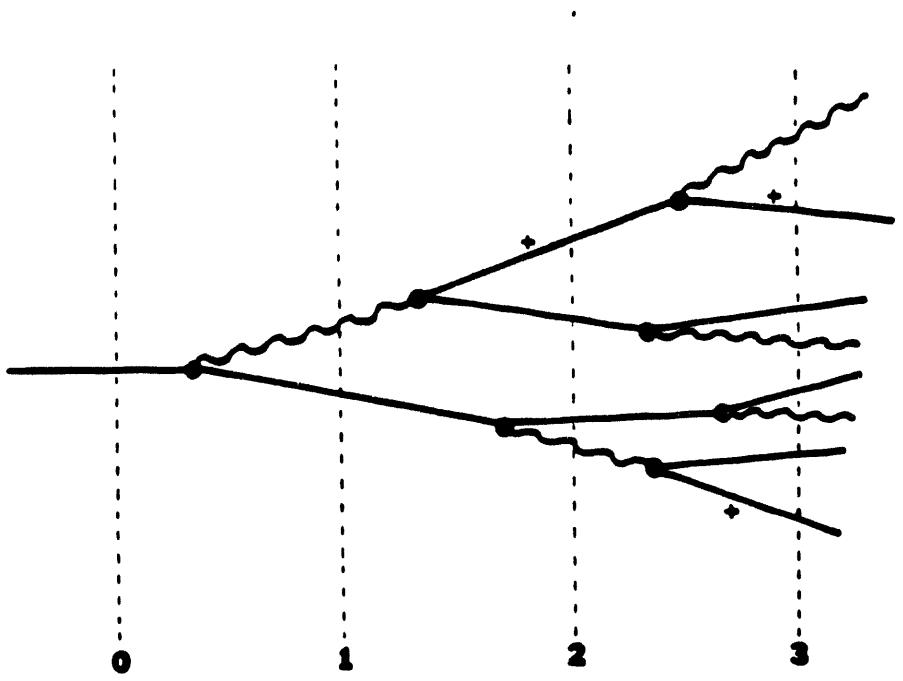

Figure 5: Simple model for the development of an electromagnetic shower. Solid lines (with +) indicate electrons (positrons) and wavy lines indicate photons. The numbers at the bottom indicate the distance measured in radiation lengths. (from [24])

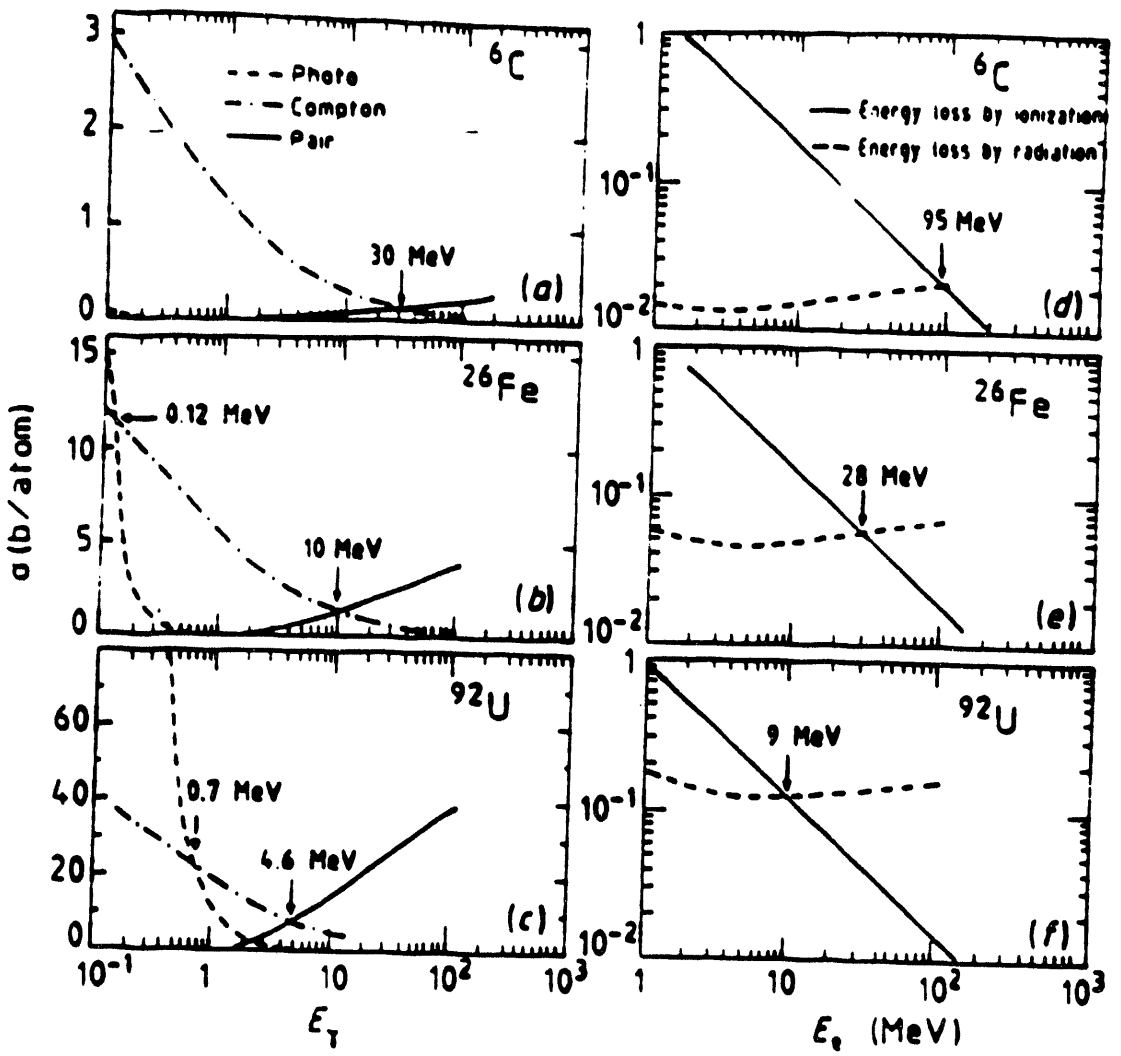

Figure 6: The cross-sections for pair production, Compton scattering, and the photoelectric effect, as a function of the photon energy in carbon (a), iron (b), and uranium (c). The fractional energy loss by radiation and ionization, as a function of the electron energy, in carbon (d), iron (e), and uranium (f). (from [33])

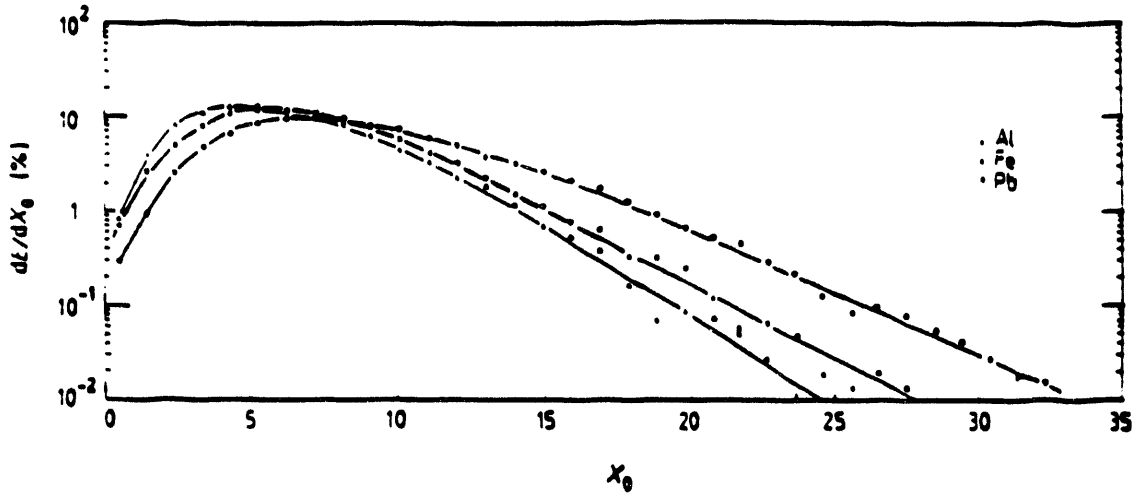

Figure 7: The energy deposit as a function of depth, for a 10 GeV electron shower developing in aluminum, iron, and lead, showing approximate scaling of the longitudinal shower profile, when expressed in units of radiation length, X_0. Results of monte carlo calculations. (from [33])

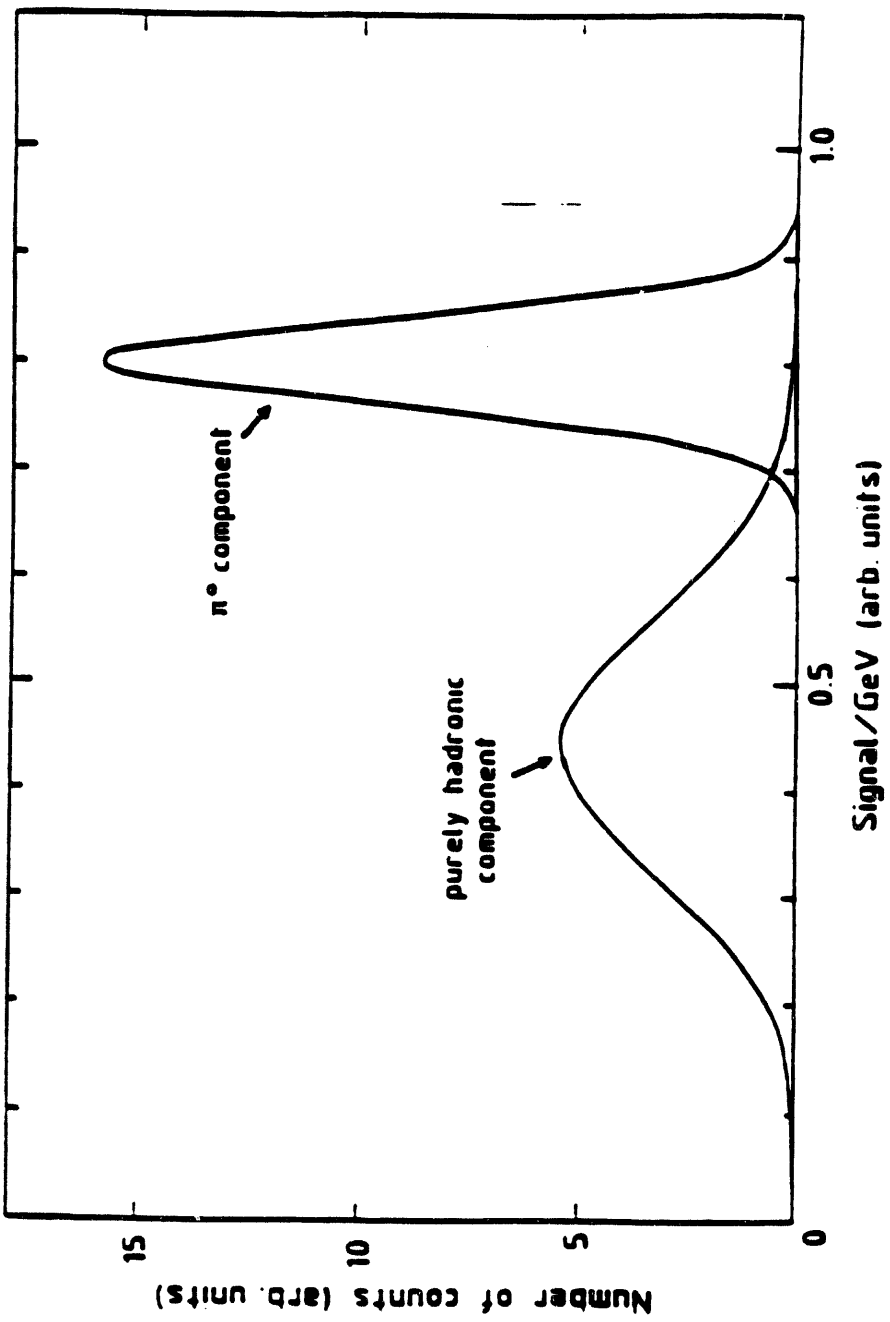

Figure 8: Schematic view of the response of a hadron calorimeter to the electromagnetic and non-electromagnetic components of the hadronic shower. (from [27])

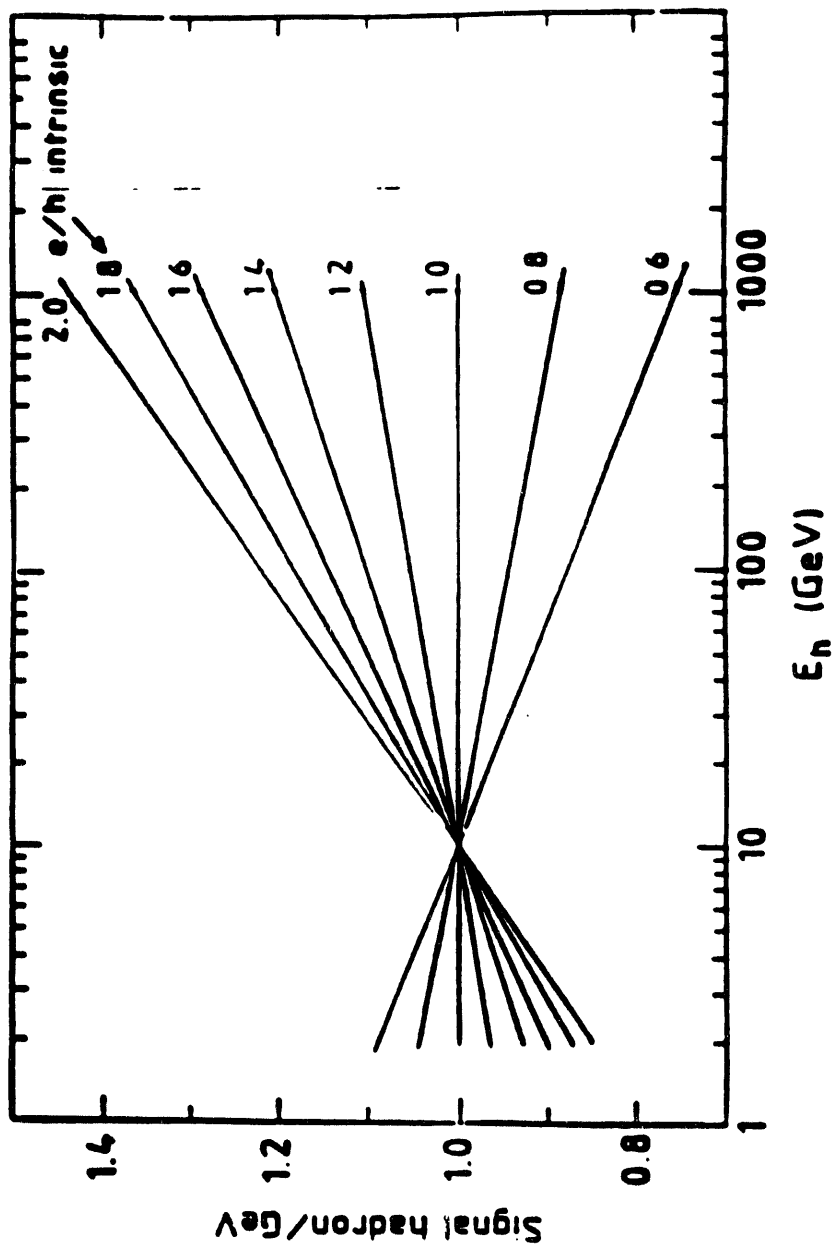

Figure 9: Monte carlo simulation of the effects of $\frac{e}{h_{intr}} \neq 1$ on the signal linearity of hadron calorimeters. E_h is the energy of the incident hadron. (from [26])

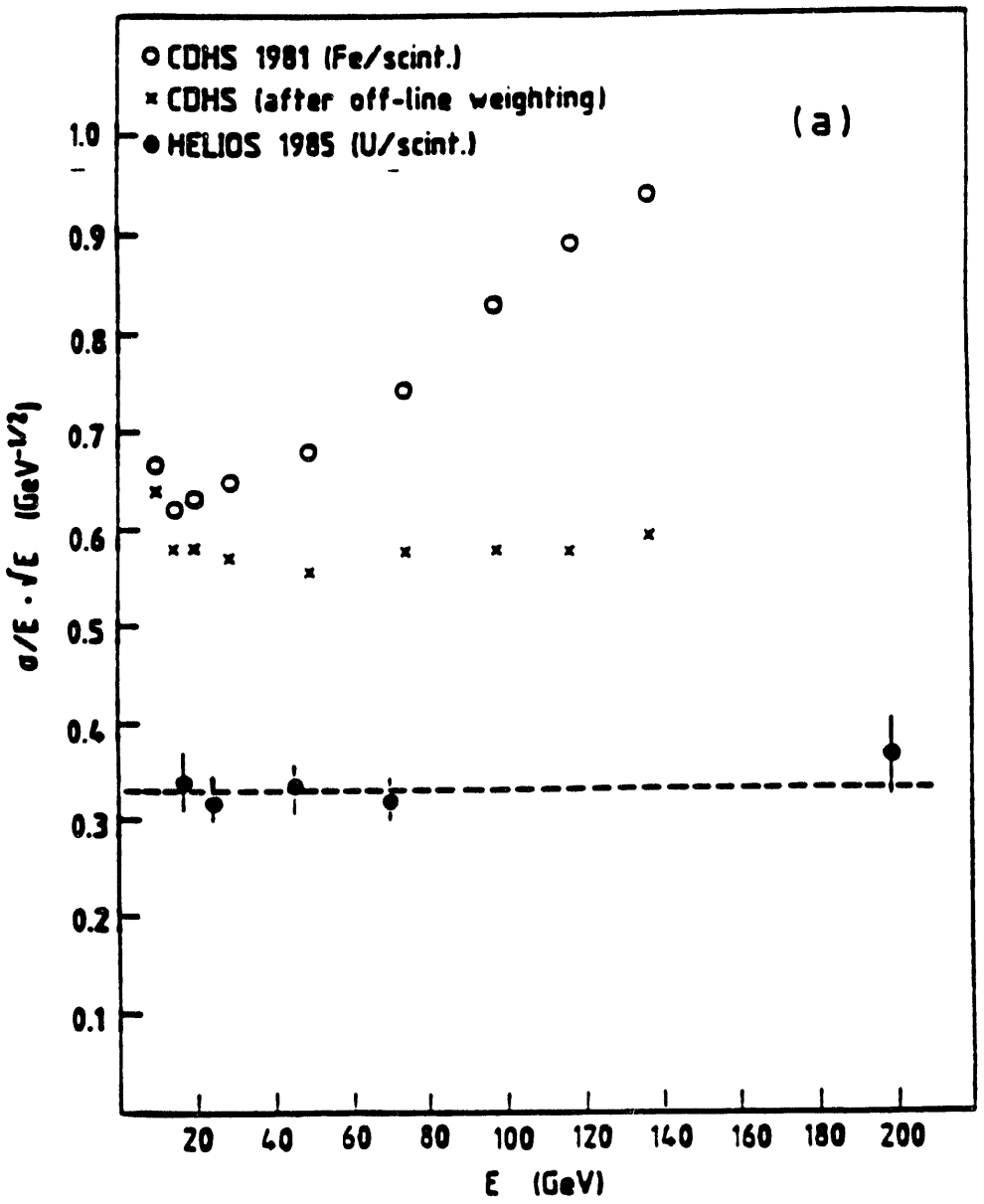

Figure 10: Experimental data for the CDHS calorimeter ($\frac{e}{h} \approx 1.4$) and the HELIOS calorimeter ($\frac{e}{h} \approx 1.0$), showing the energy resolution as a function of the incident hadron energy. (from [26])

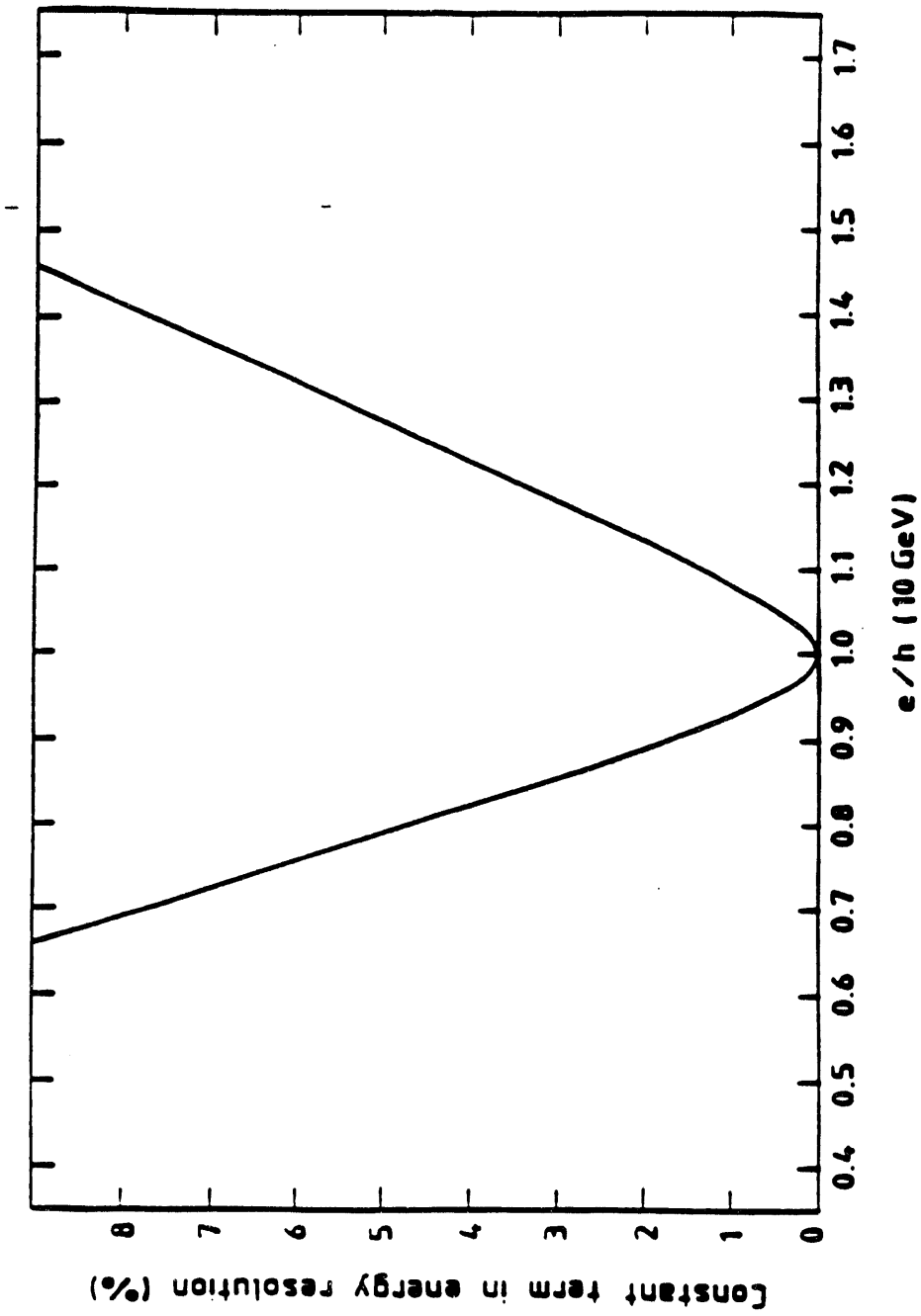

Figure 11: The constant term in the energy resolution (in %), as a function of $\frac{e}{h}$ (evaluated at 10 GeV). (from [27])

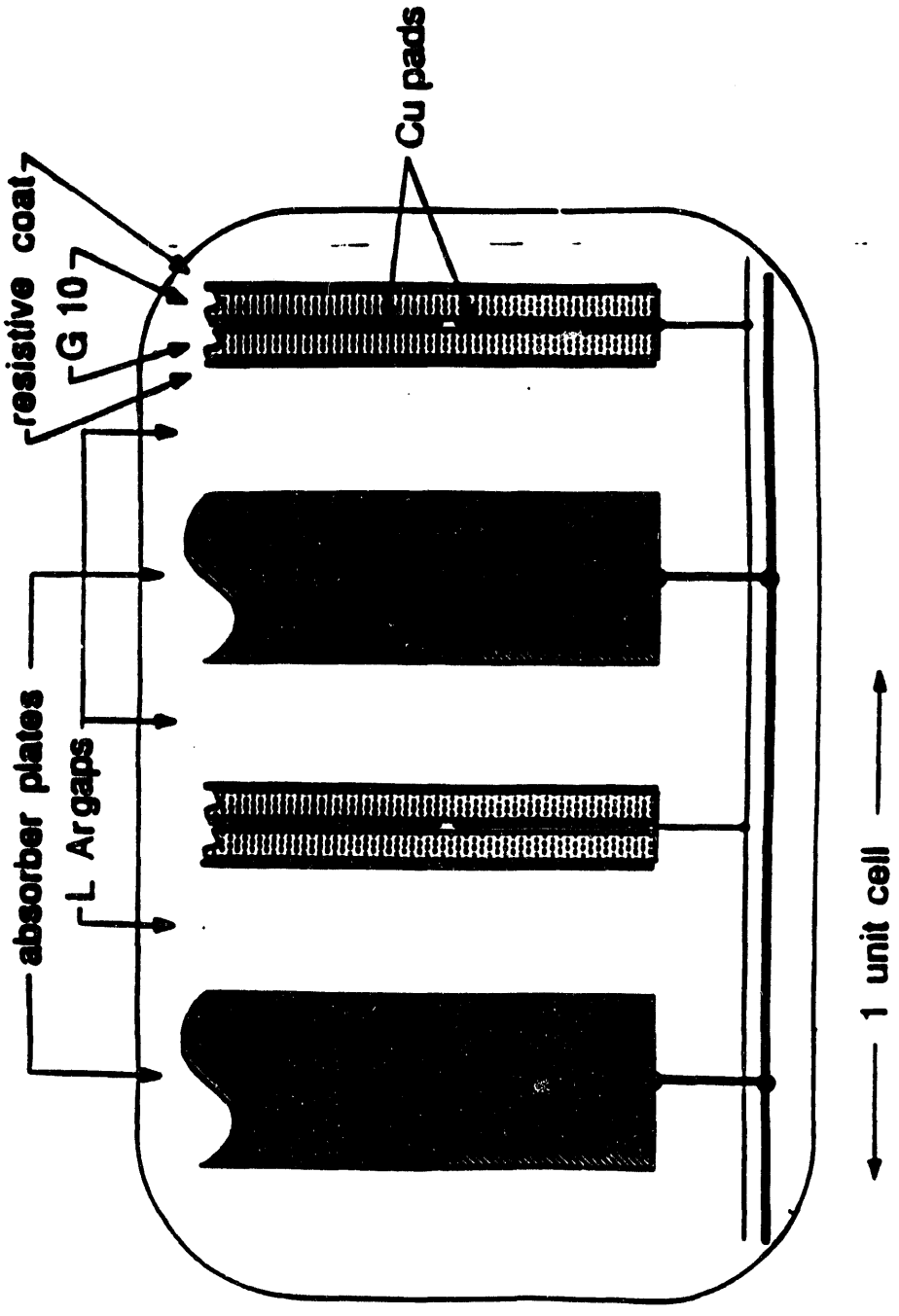

Figure 12: Sketch of one unit cell in the D0 calorimeter. (from [29])

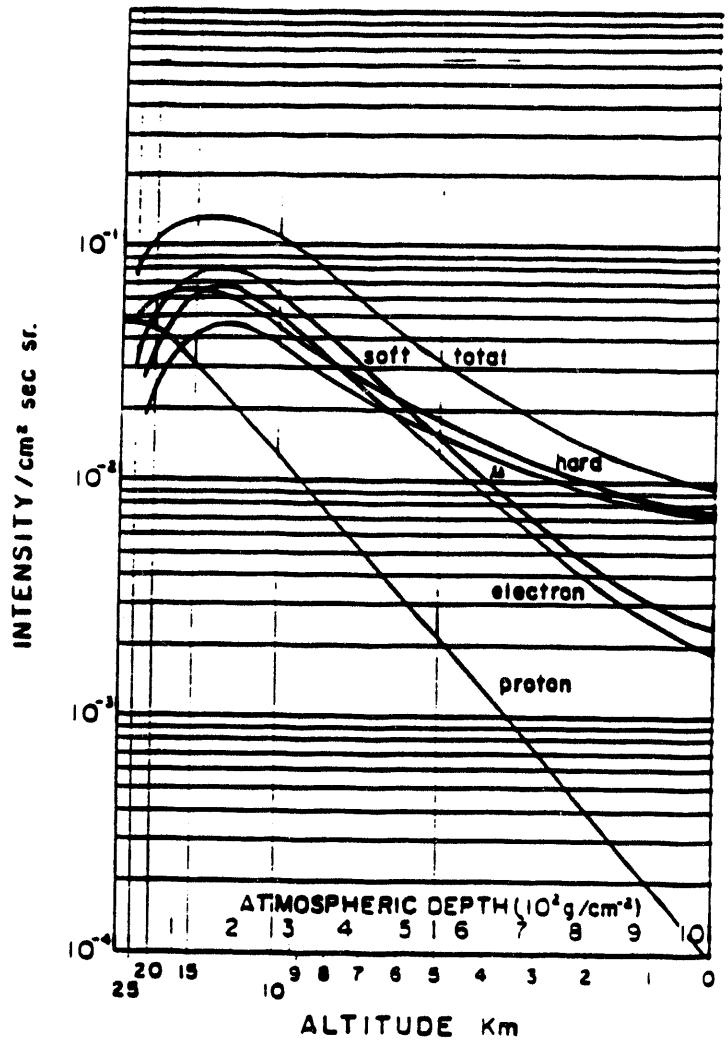

Figure 13: The intensities of the various components of vertical cosmic rays in the atmosphere, as a function of atmospheric depth. (from [34])

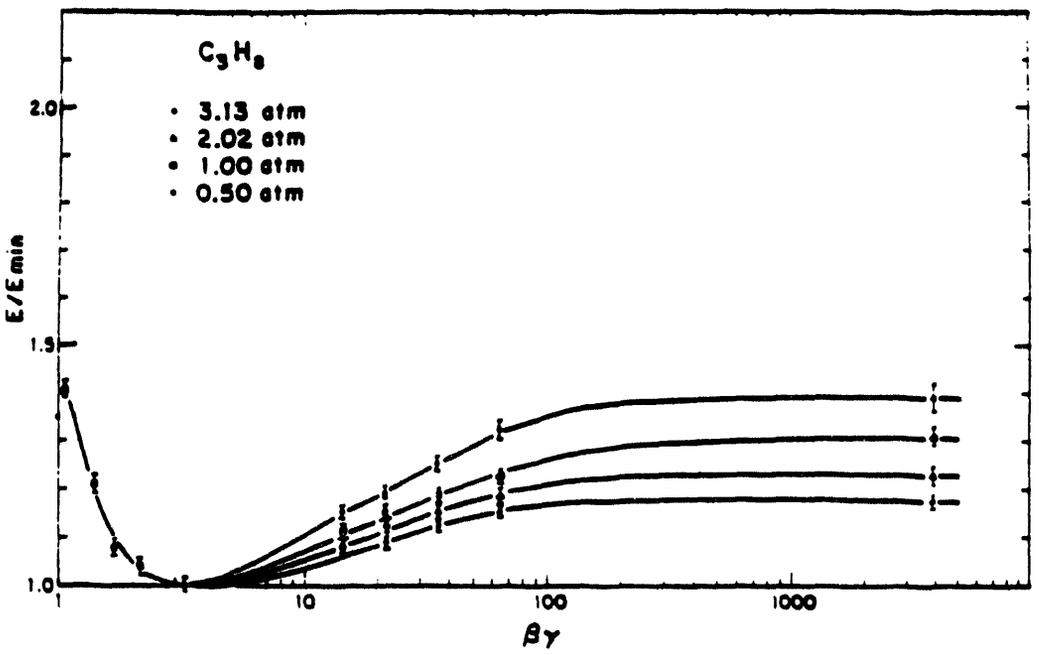

Figure 14: Measured most probable energy losses (for protons and pions) in propane gas at 4 different pressures, as a function of $\beta\gamma$. The energy losses are normalized to those for 3 $\frac{GeV}{c}$ protons. (from [54])

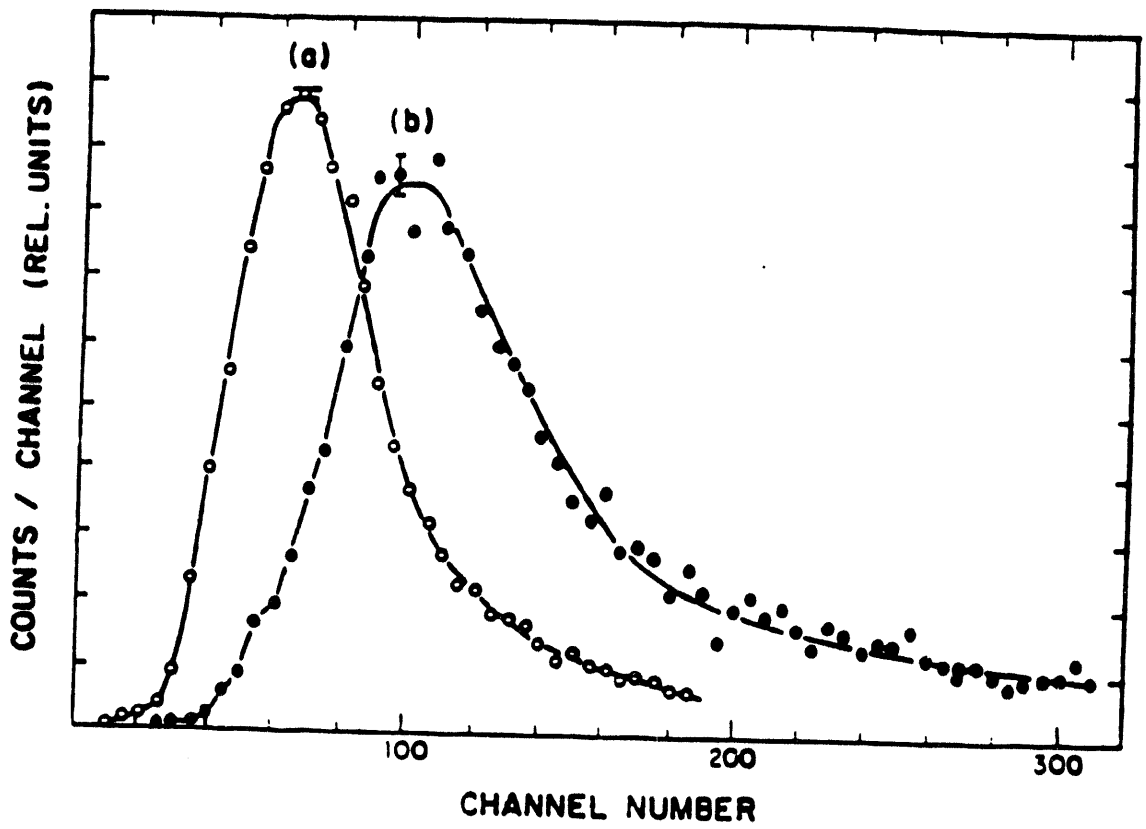

Figure 15: Measured pulse height distributions for (a) 3 $\frac{GeV}{c}$ protons and (b) 2 $\frac{GeV}{c}$ electrons in a 90% Ar + 10% CH_4 gas mixture. (from [54])

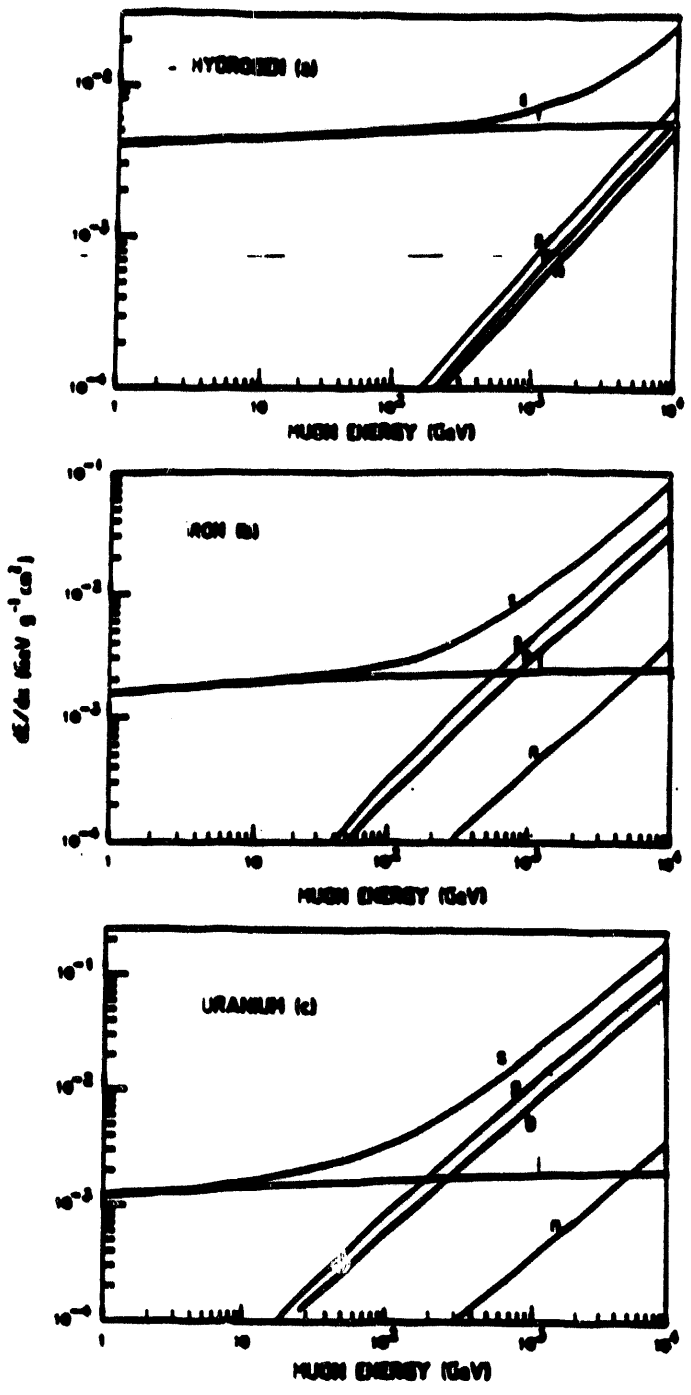

Figure 16: Calculated contributions to the energy loss from ionization (i), bremsstrahlung (b), pair production (p), nuclear interactions (n), and their sum (s) as functions of the energy in hydrogen (*a*), iron (*b*), and uranium (*c*). (from [47])

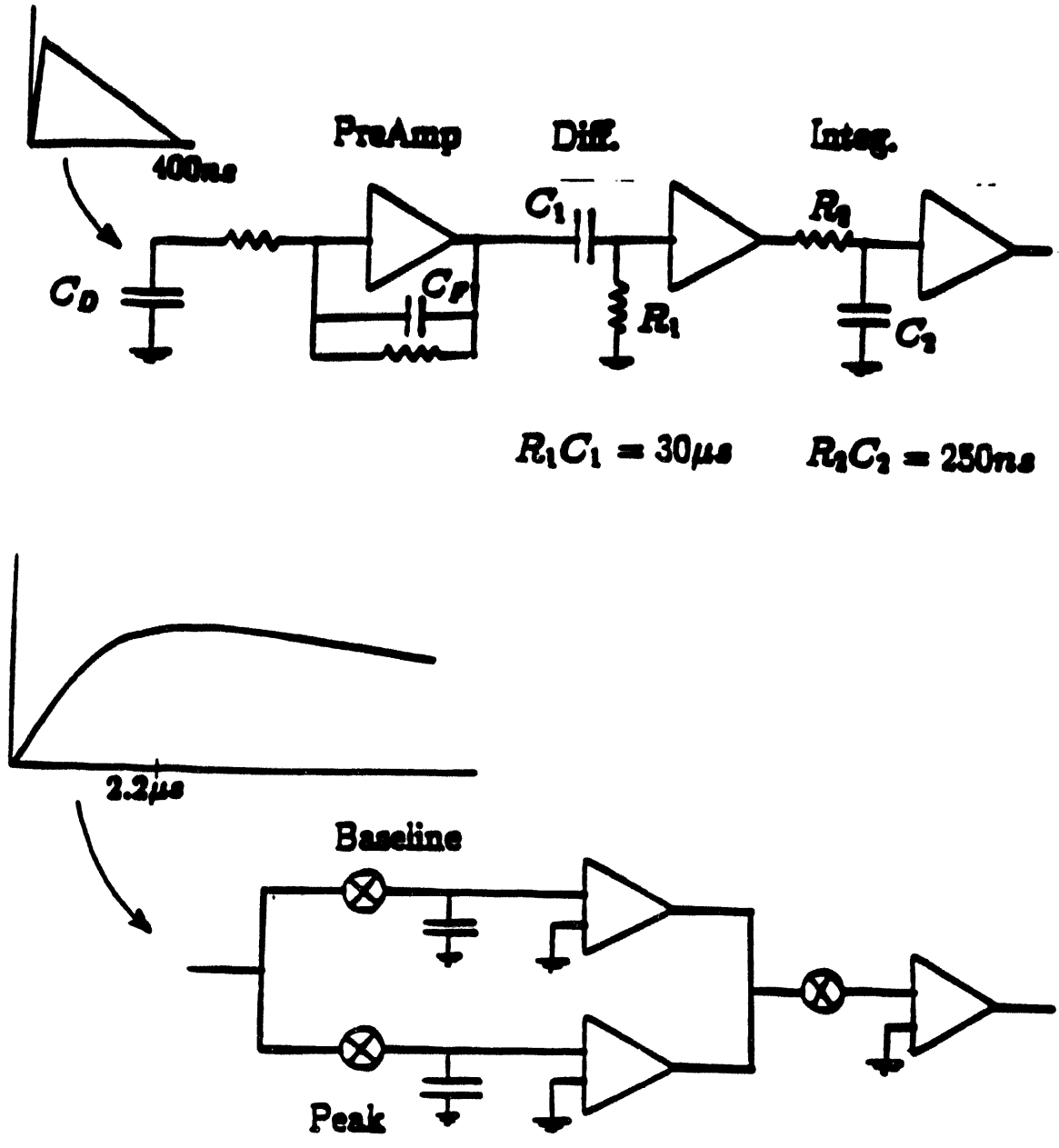

Figure 17: Simple schematic of the D0 calorimeter electronics. (from [65])

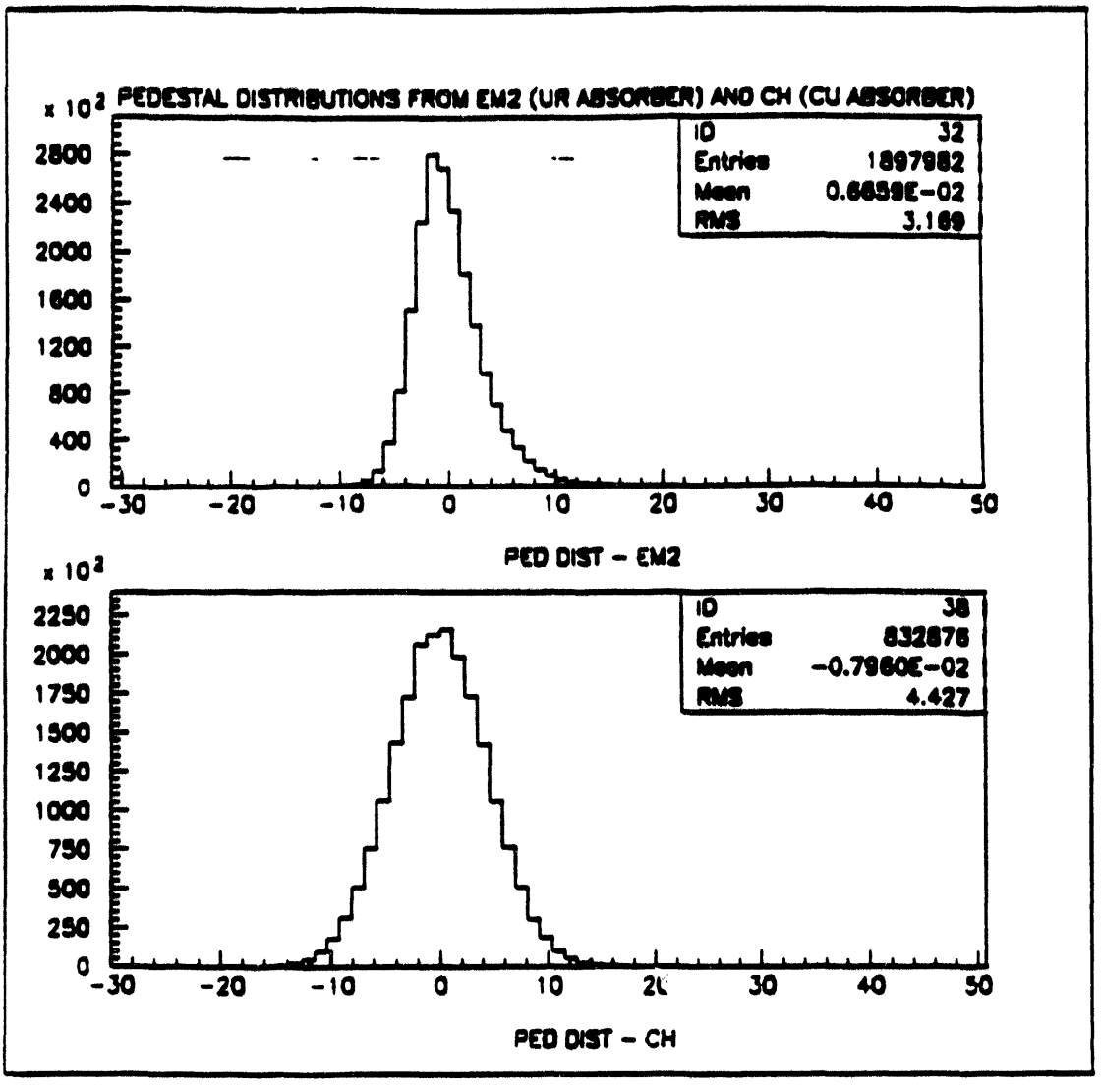

Figure 18: Pedestal distributions for electromagnetic layer 2 (EM2) and the coarse hadronic (CH) sections. The pedestal distribution for EM2, which uses uranium absorber, is asymmetric due to the uranium noise. The CH pedestals are symmetric, as copper is used in this section.

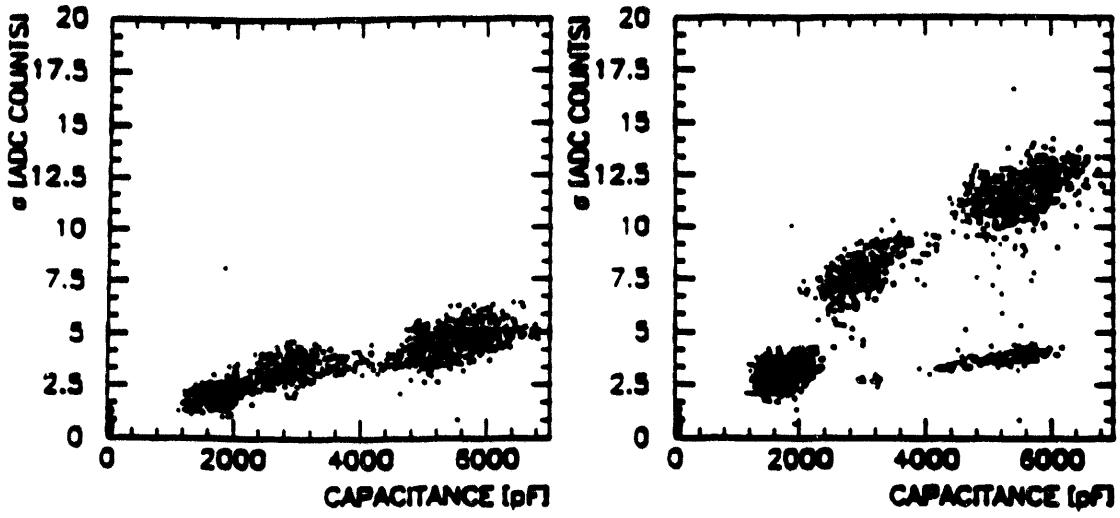

Figure 19: Widths of pedestals versus capacitance with high-voltage off (left-most plot – electronic noise only) and high-voltage on (right-most plot – electronics plus uranium noise). (from [65])

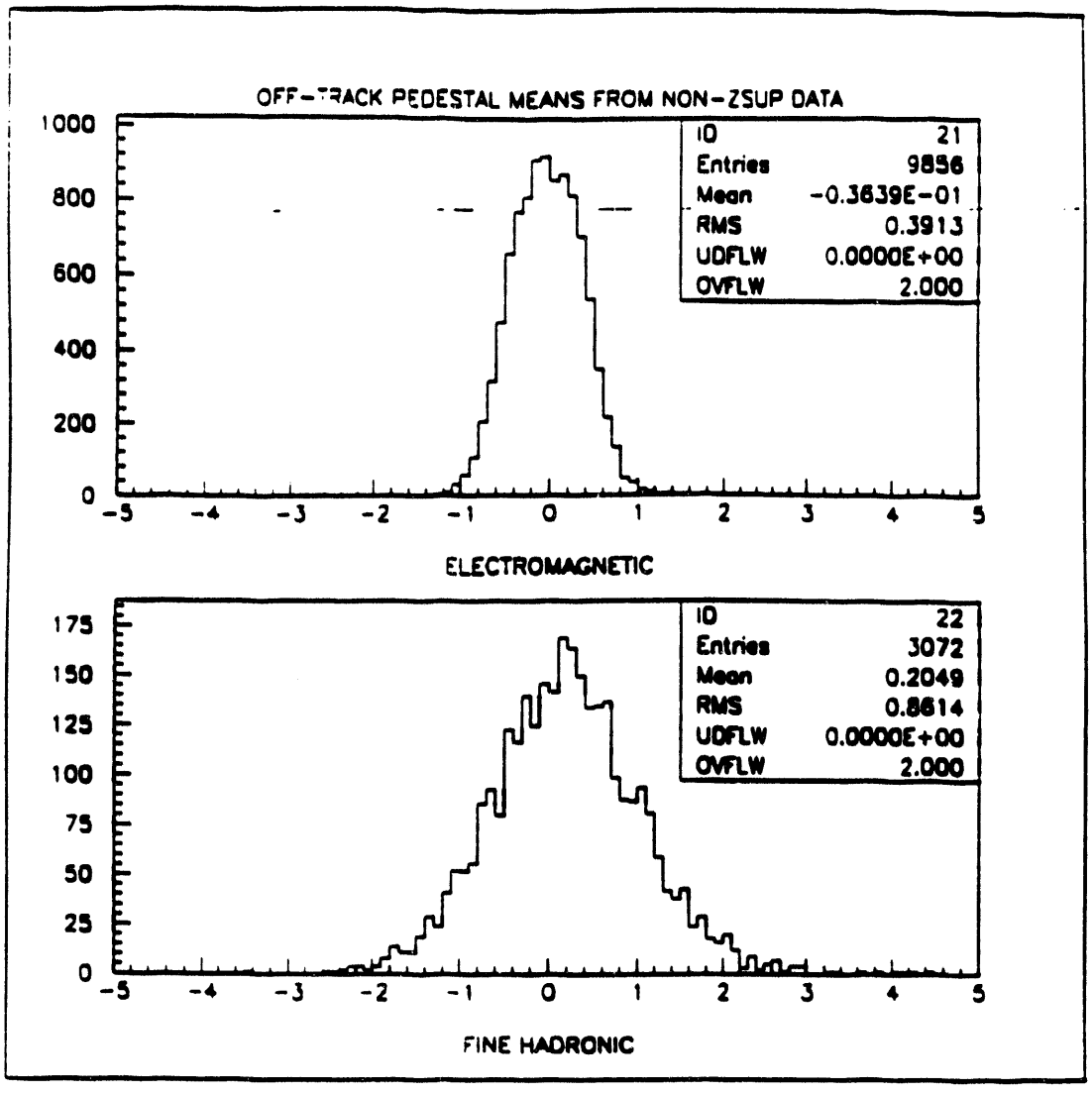

Figure 20: Off-track pedestal means in the electromagnetic sections (upper) and the fine hadronic sections (lower) of the calorimeter, as computed from data taken during the Cosmic Ray Run.

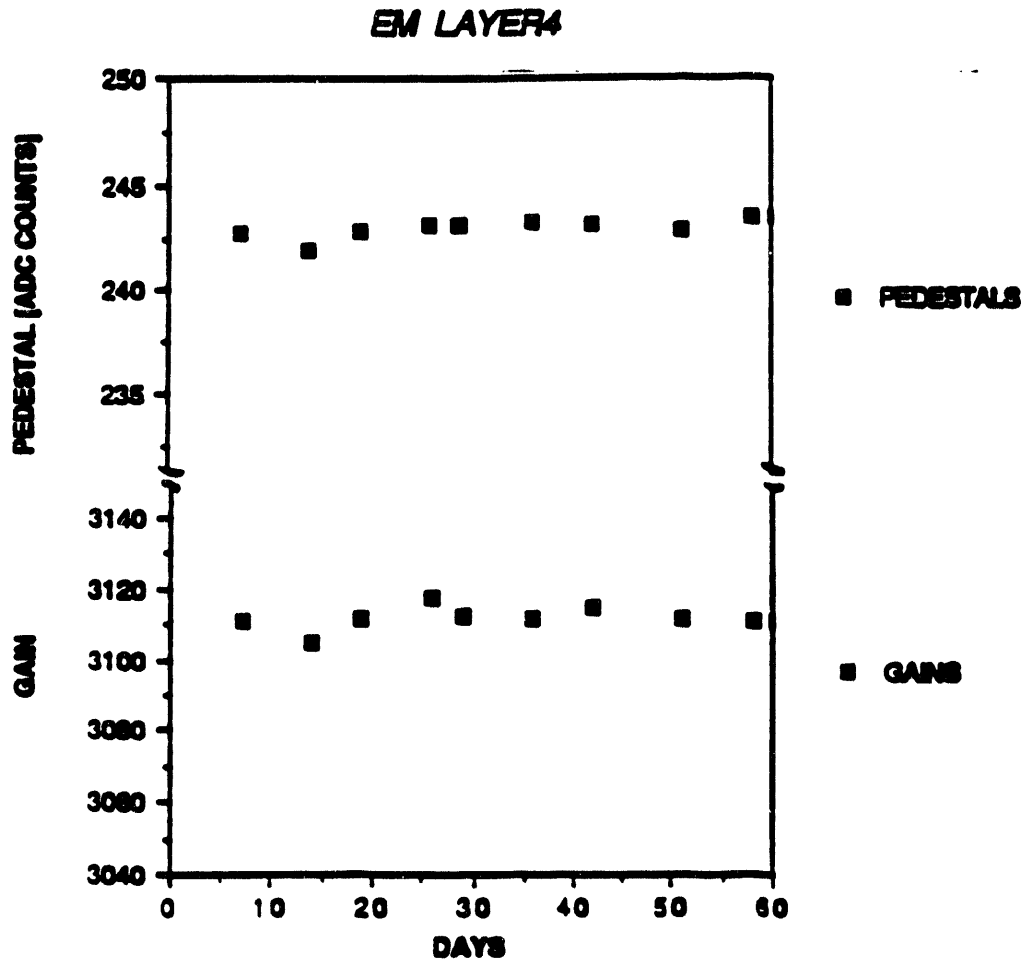

Figure 21: The average of the individual channel pedestal means (upper portion of plot) and gains (lower portion of plot) in electromagnetic layer 4, as a function of time during the Cosmic Ray Run. The abscissa is in days after the start of the run. (from [65])

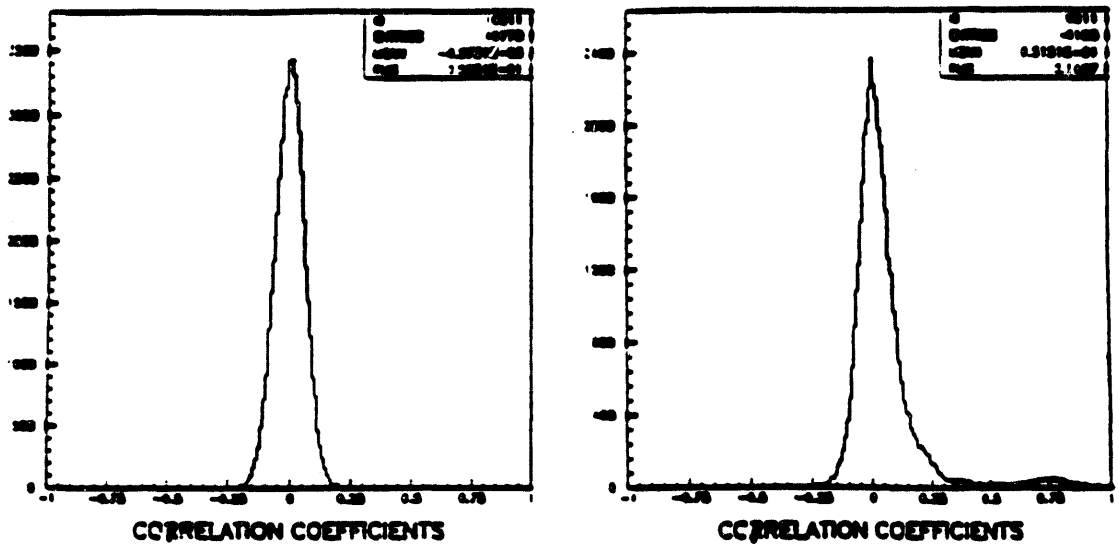

Figure 22: Correlation coefficients in one ADC card in the northwest quadrant of the central calorimeter, as obtained during the Cosmic Ray Run. The plot on the left (right) is without (with) an artificial noise source introduced. (from [65])

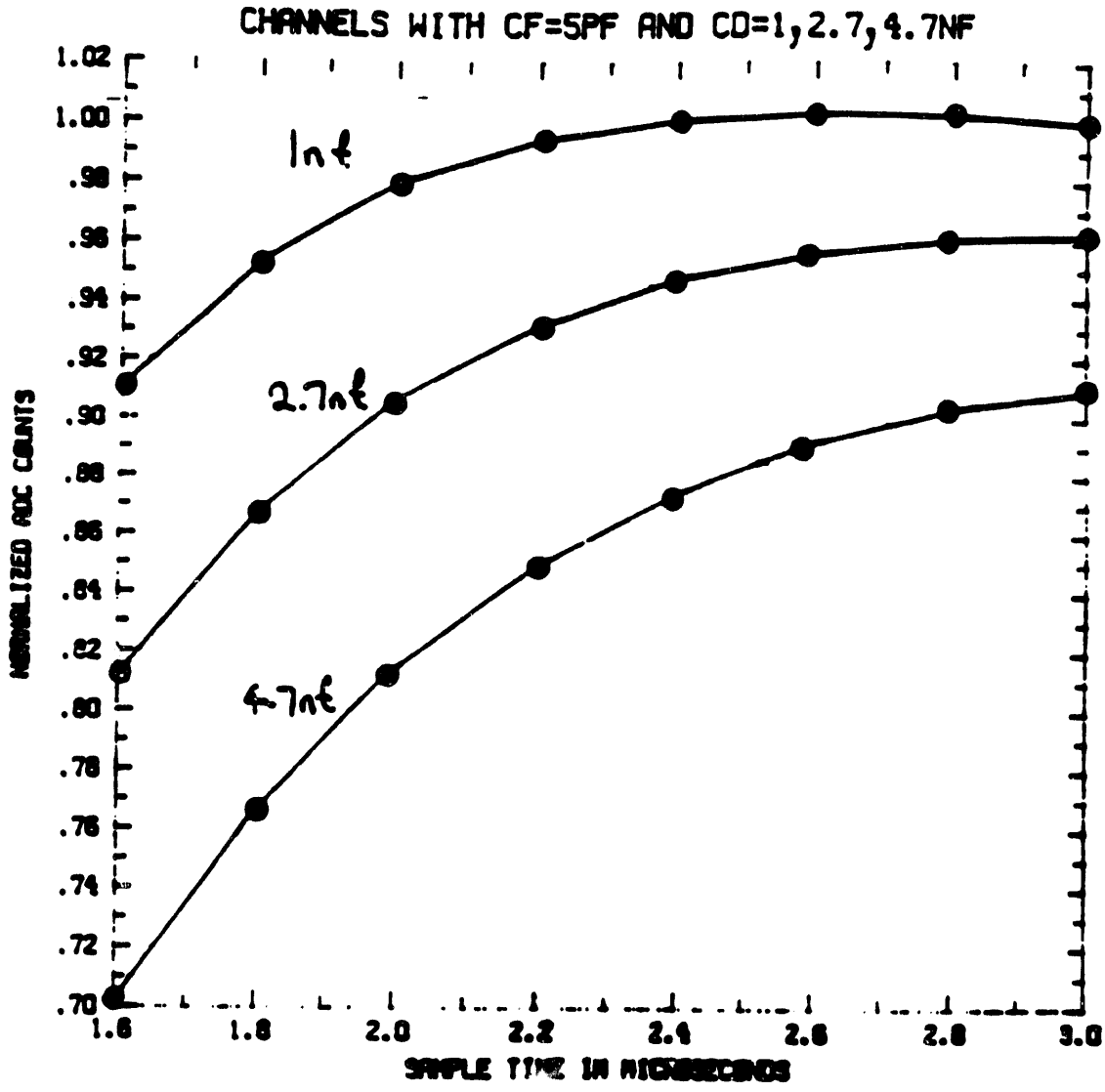

Figure 23: Signal shape, as a function of sampling time, at the output of the BLS for 3 different capacitance values (C_D). (from [58])

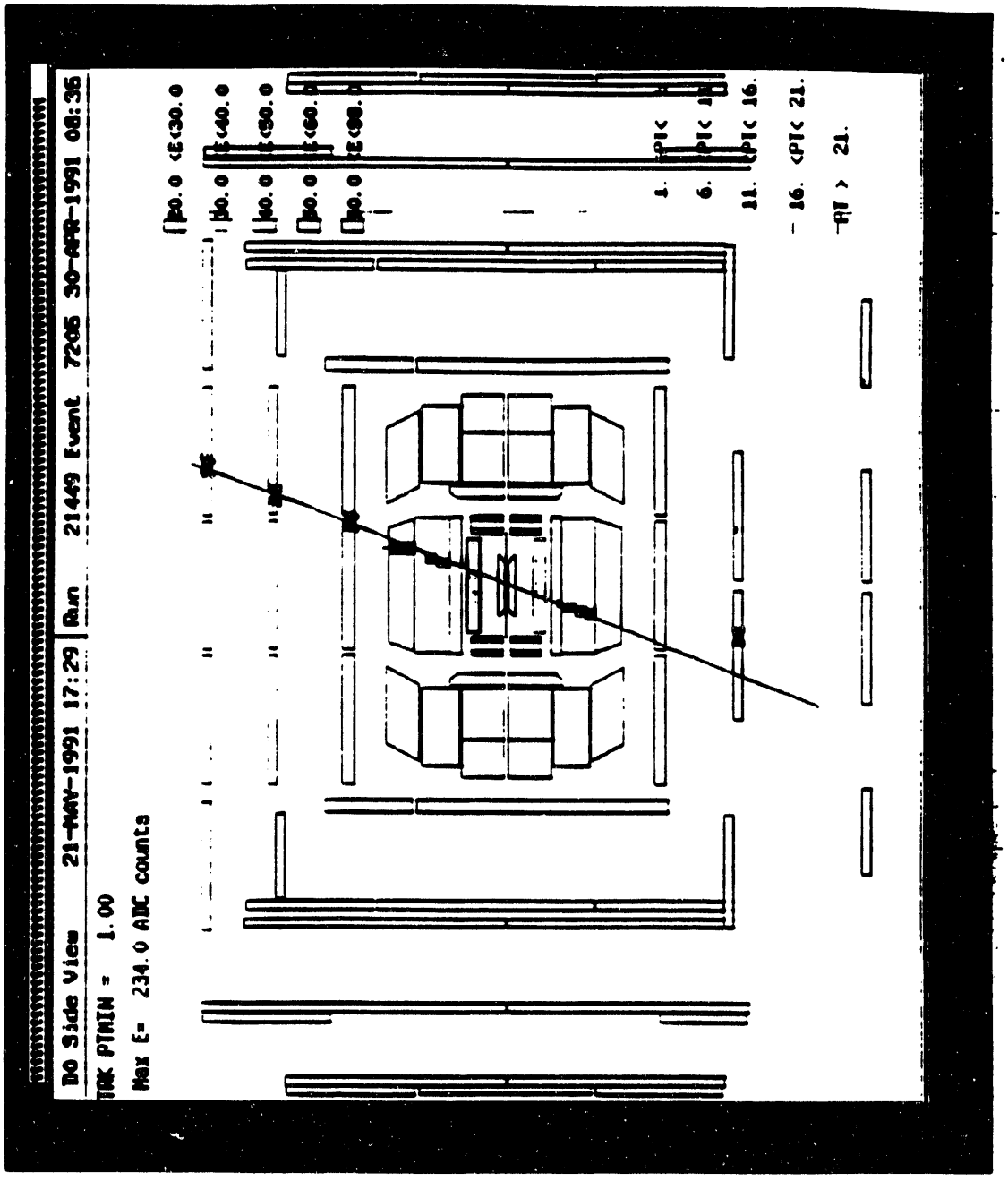

Figure 24: Event display of a muon passing through the detector, in side view.

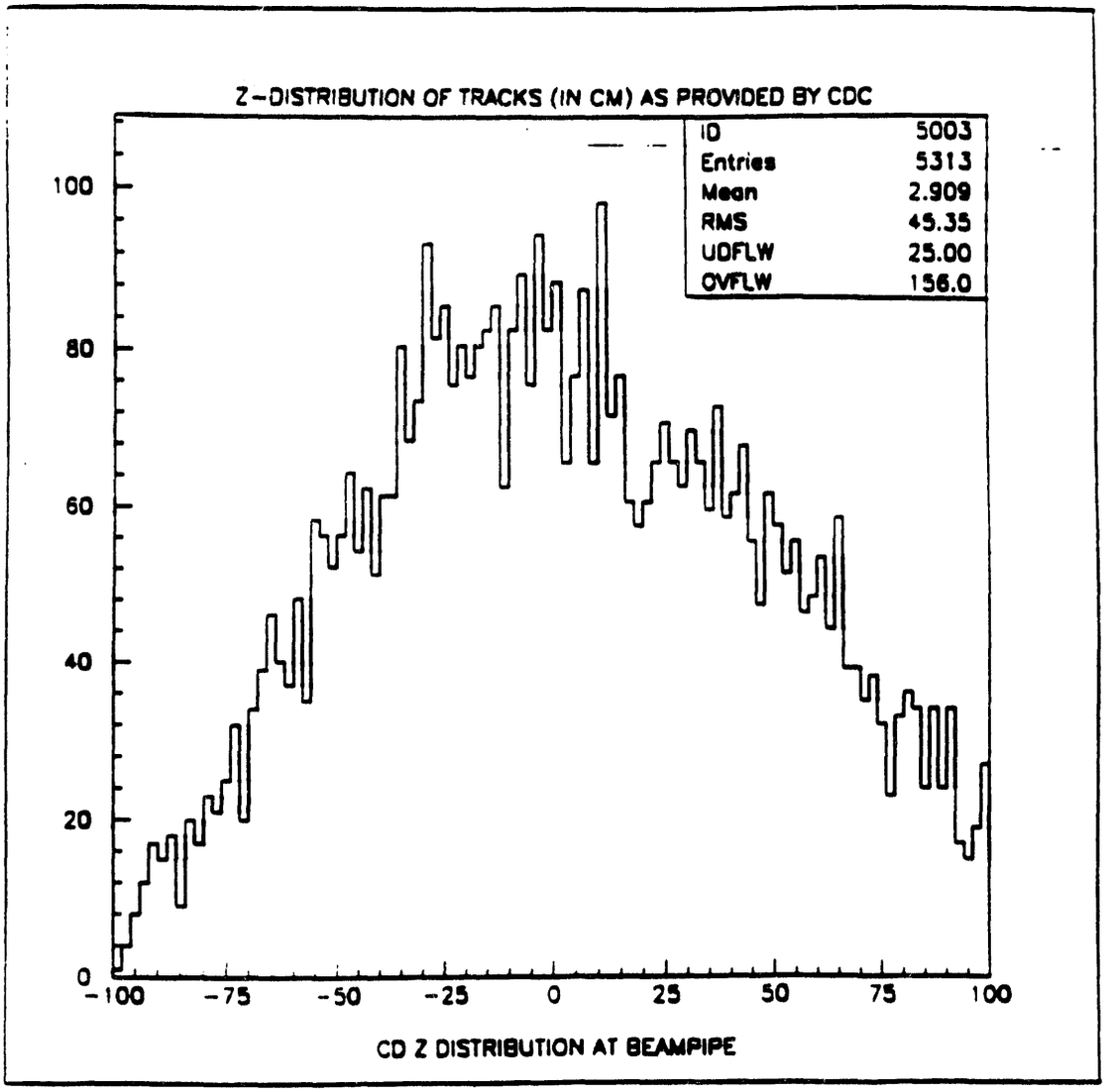

Figure 25: Distribution of the Z-position of the muon tracks at the beam pipe (X = Y = 0), extracted from central drift chamber information during the Cosmic Ray Run.

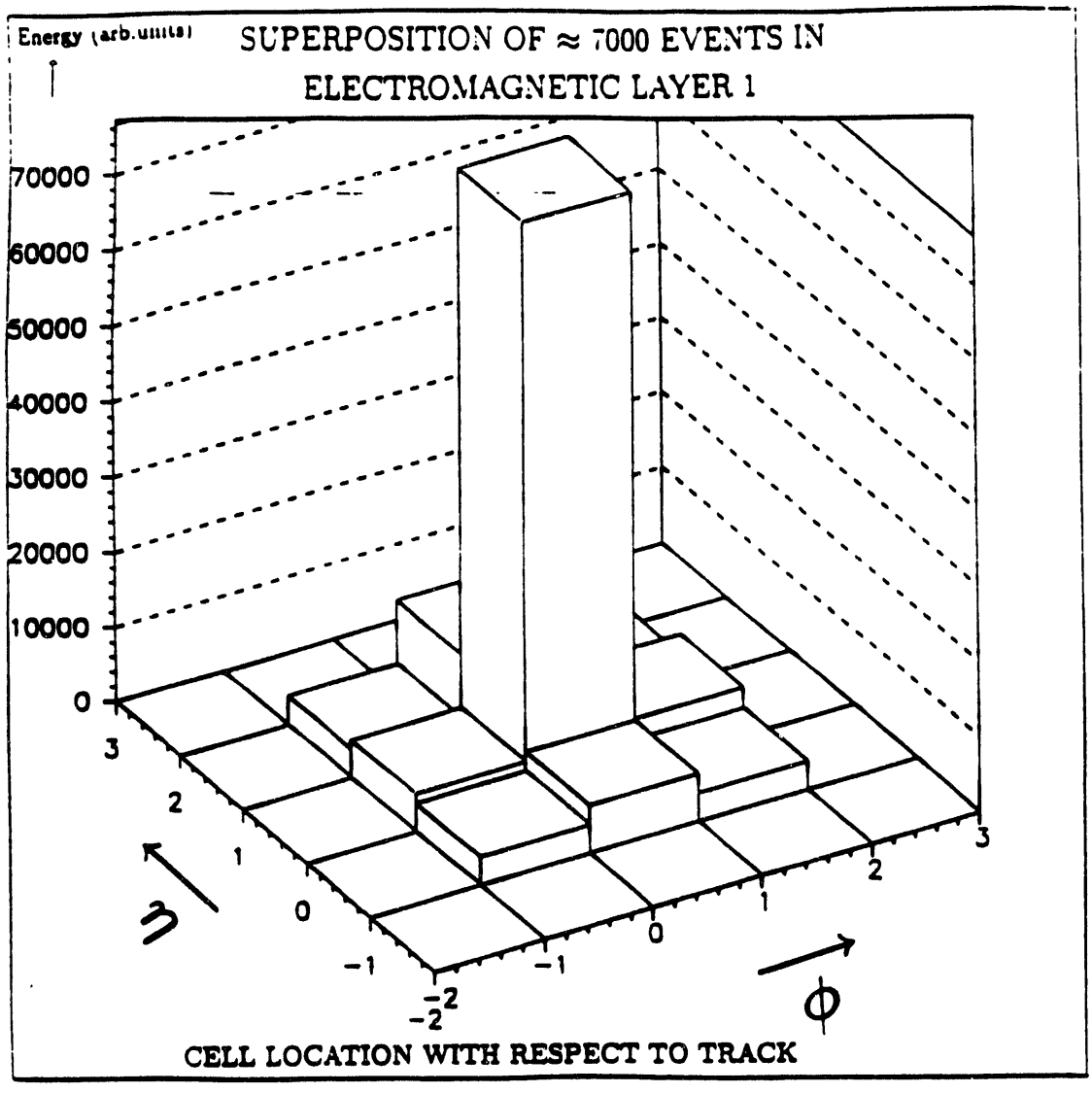

Figure 26: Superposition of energy in 3X3 cell area of EM1 in ≈ 7000 magnet-off, non-zero-suppressed events. The central cell is the cell predicted to have been intercepted by the muon, as determined from CDC data. Details are in Chapter VIII.

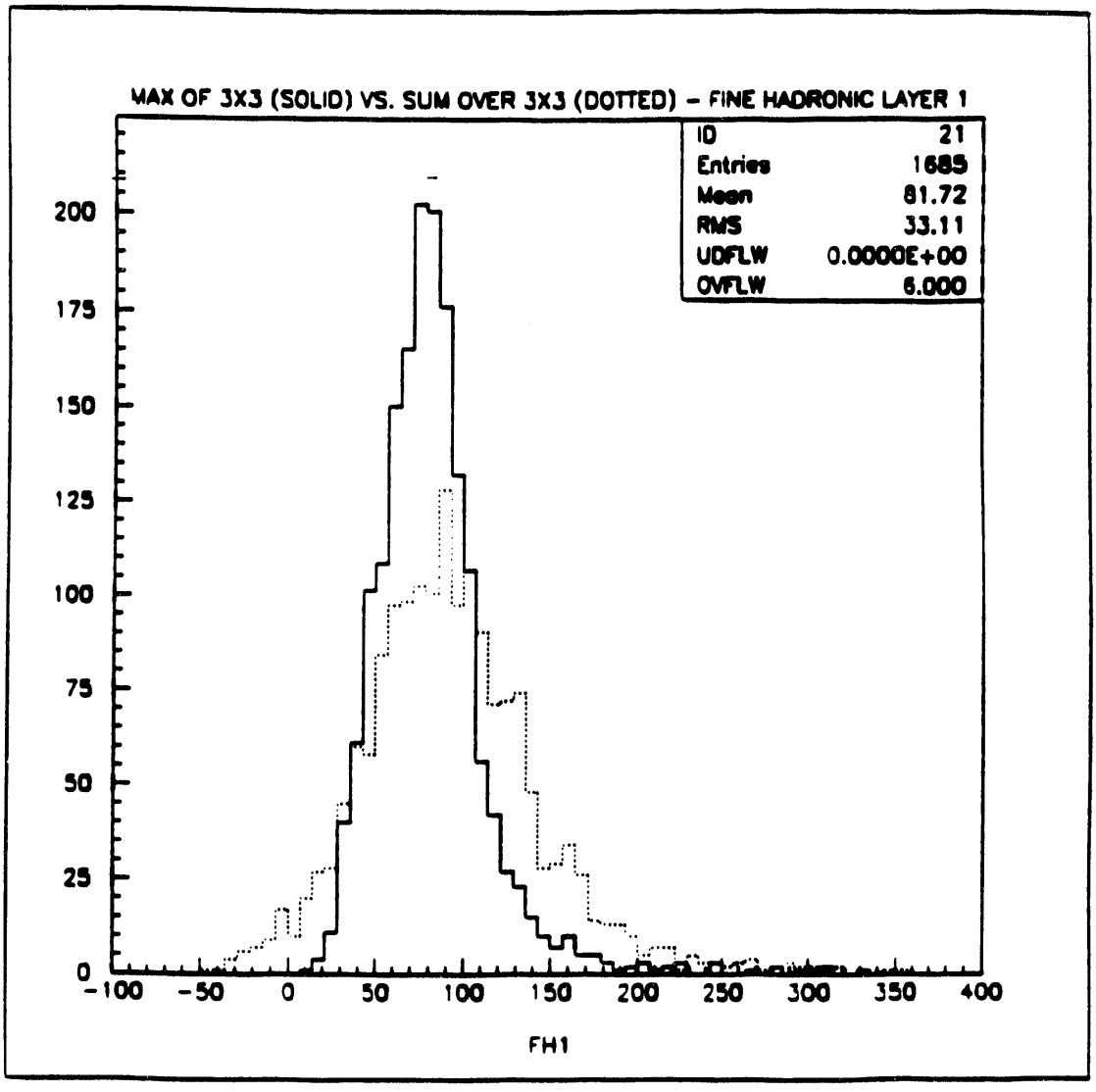

Figure 27: Distributions resulting from event-by-event summing of the 3X3 cell area (dotted), and from picking the maximum (solid), for magnet-off, non-zero-suppressed event sample.

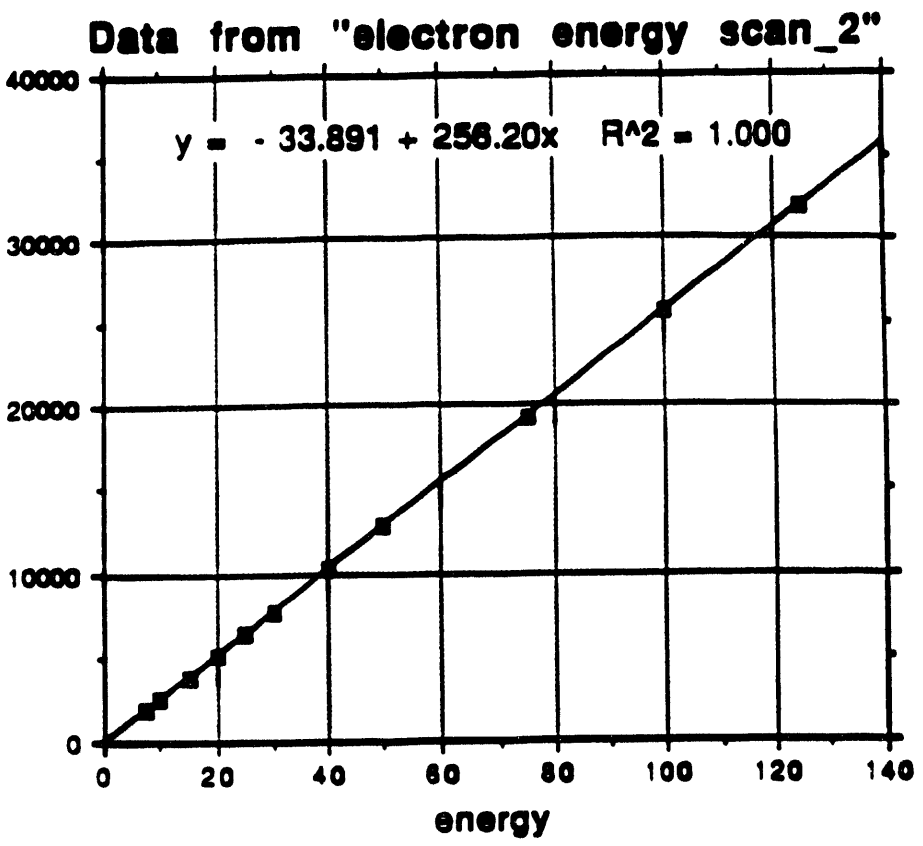

Figure 28: Measured electron energy in test calorimeter (arbitrary units – see Chapter IX) as a function of incident electron energy (as determined from bending magnets in the beam line). Data was obtained from D0 test beam run. (from [64])

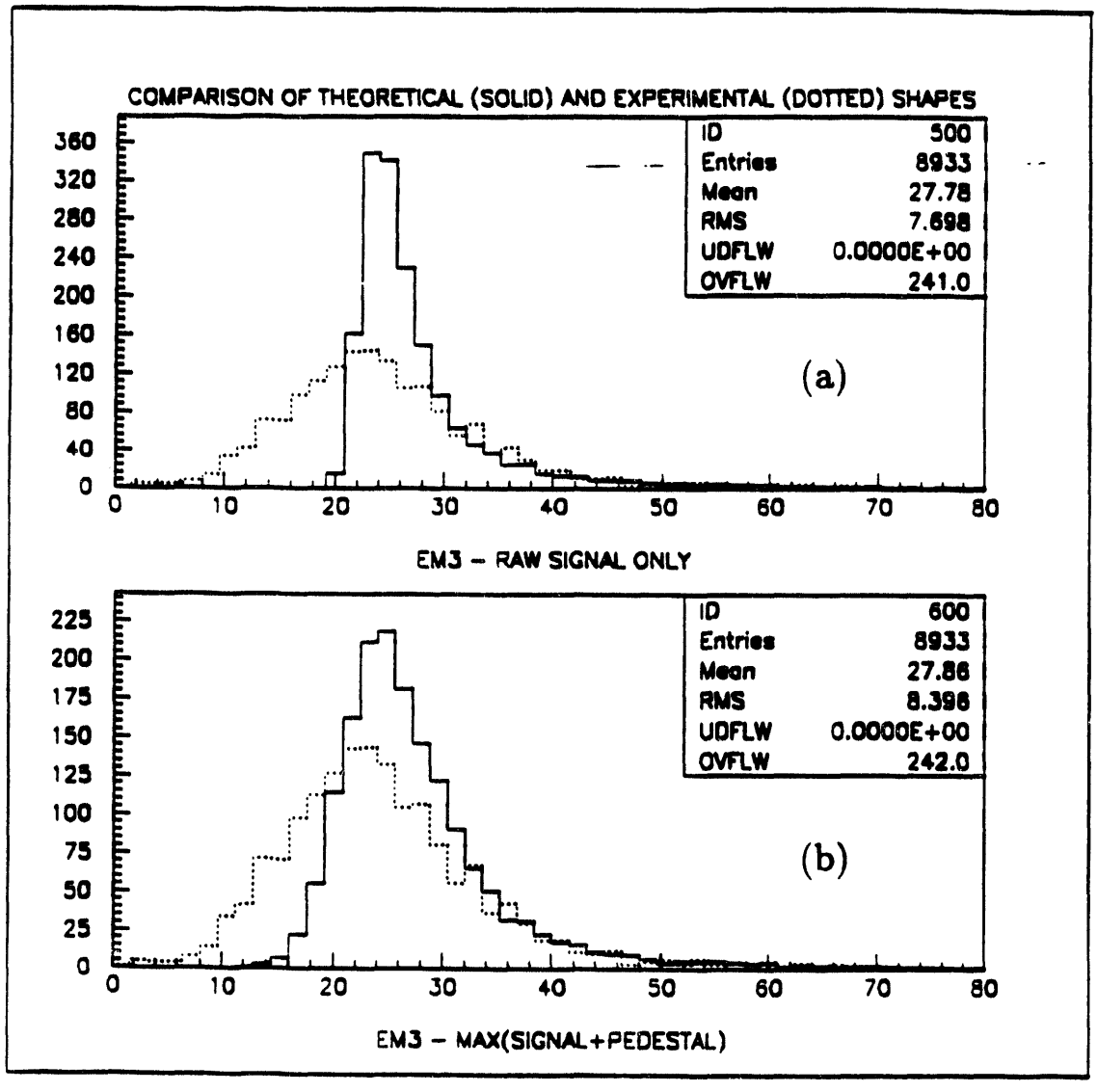

Figure 29: Comparison of shapes of experimental (dotted) with theoretical (solid) distributions for EM3. Theoretical plot represents pure Landau prediction with no experimental effects folded in (a), and the maximum in the 3X3 when pedestal fluctuations, but no sharing, are added to the pure Landau spectrum (b). Details are in Chapter X.

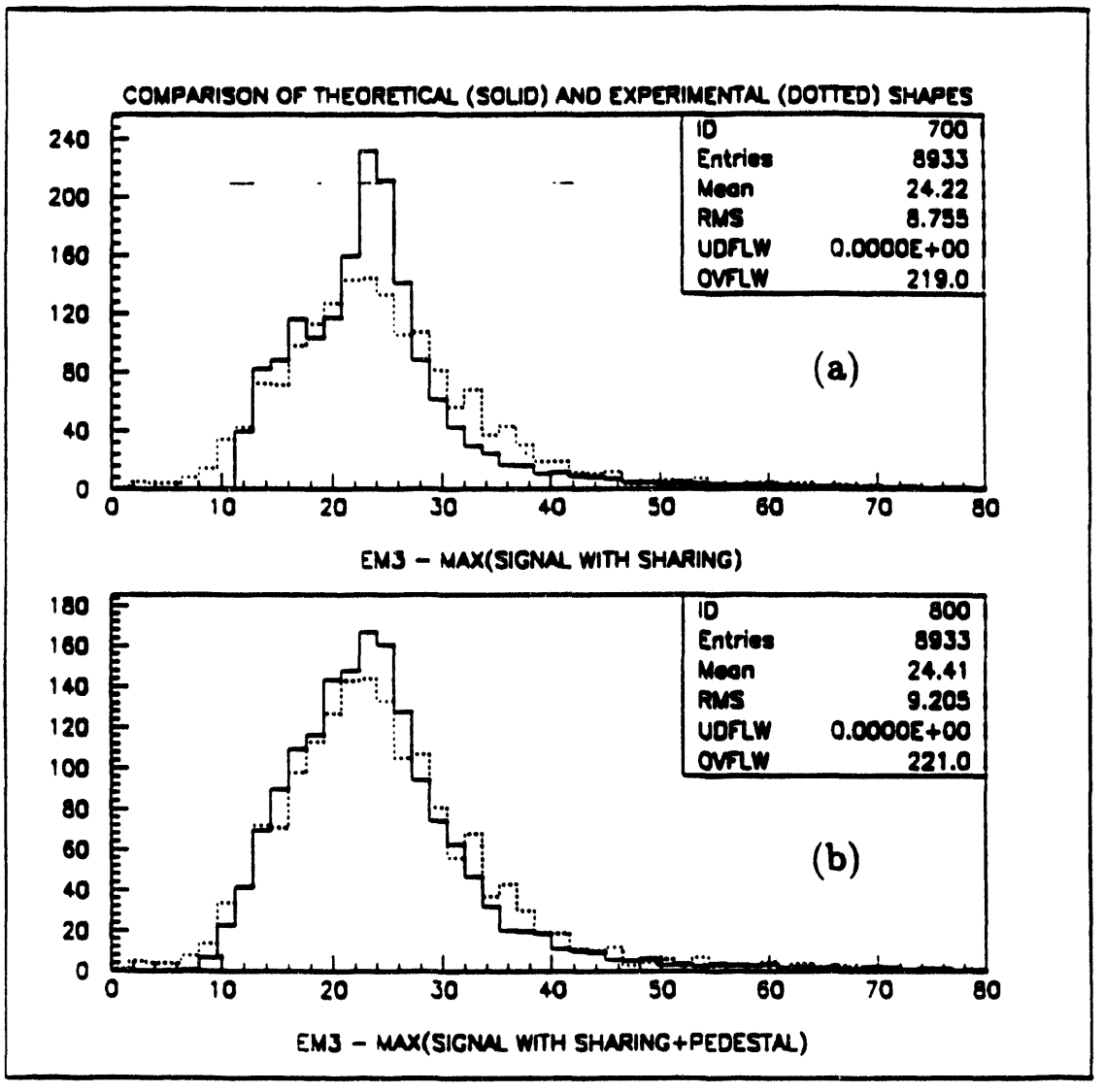

Figure 30: Comparison of shapes of experimental (dotted) with theoretical (solid) distributions for EM3. Theoretical plot represents the maximum in the 3X3 when sharing, but no pedestal fluctuations, is introduced (a), and the maximum in the 3X3 when both pedestal fluctuations and sharing are introduced (b). Details are in Chapter X.

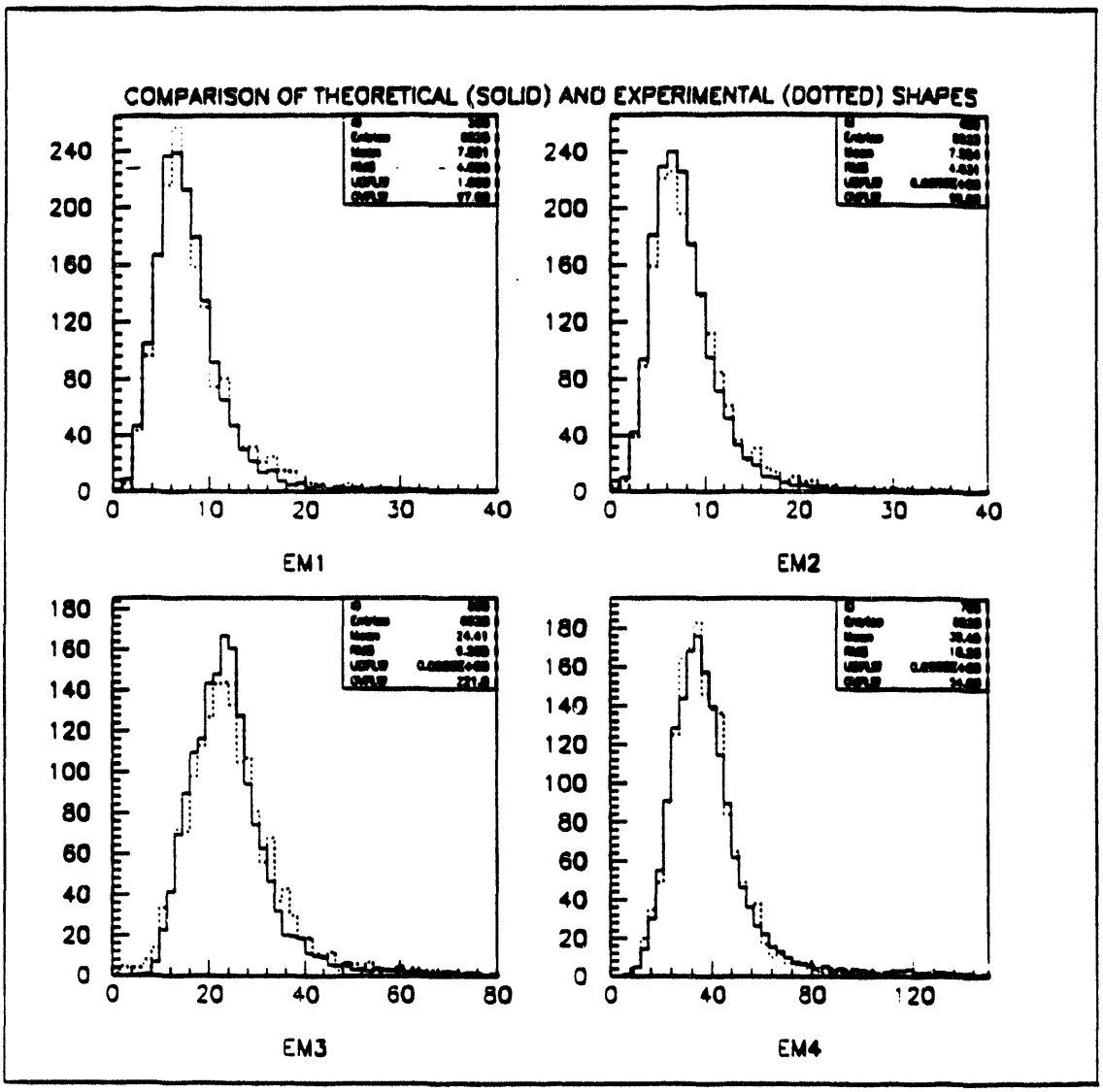

Figure 31: Comparison of shapes of experimental (dotted) with theoretical (solid) distributions, with all experimental effects (pedestal fluctuations and sharing) introduced, for the electromagnetic section.

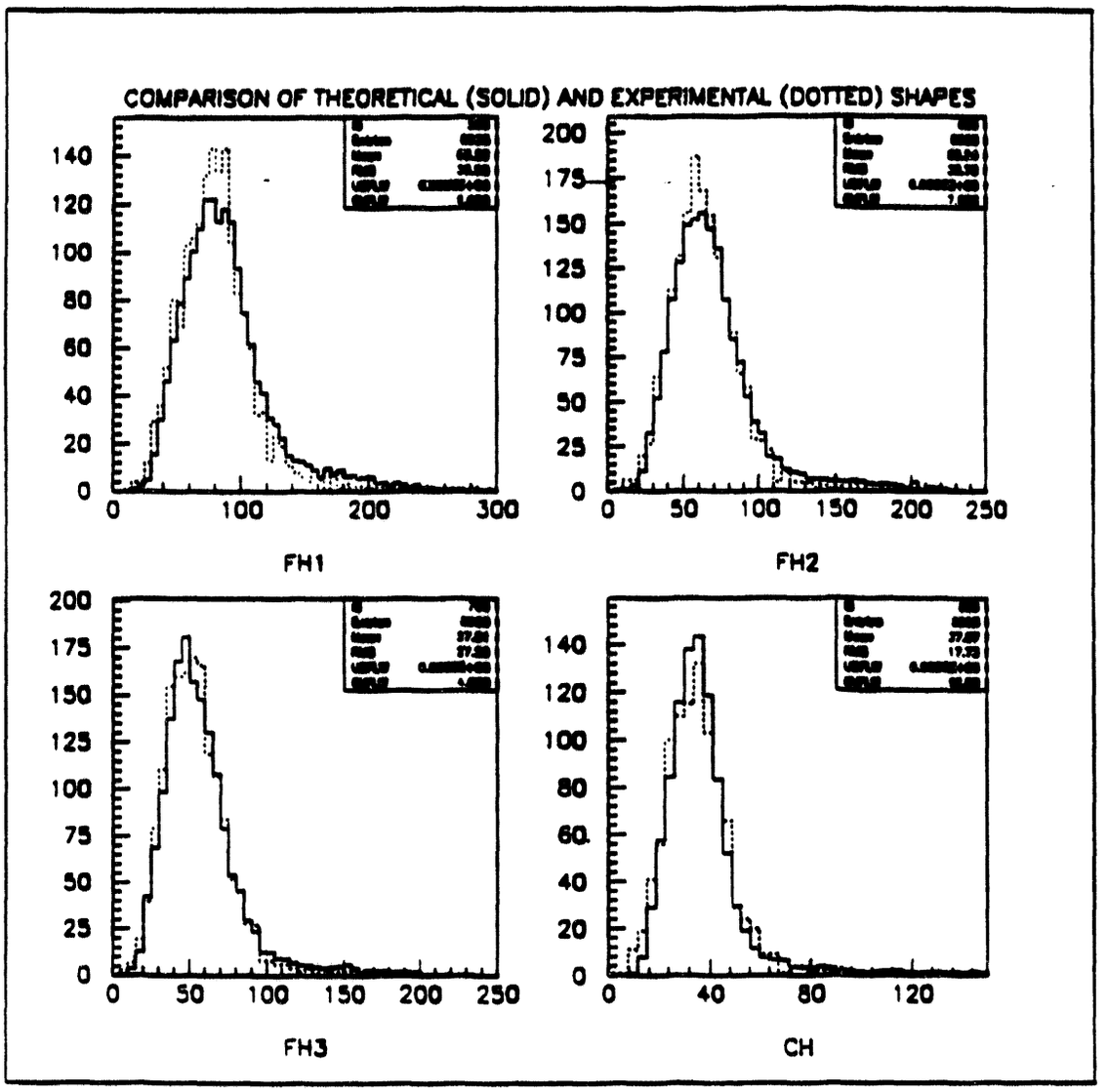

Figure 32: Comparison of shapes of experimental (dotted) with theoretical (solid) distributions, with all experimental effects (pedestal fluctuations and sharing) introduced, for the hadronic section.

BIBLIOGRAPHY

[1] V. Barger and R. Phillips, Collider Physics. Addison Wesley Publishing Company, 1987.

[2] G. Salvani and A. Silverman, "Physics with Matter-Antimatter Colliders", Phys. Rep. 171 (1988) 231-424.

[3] E. Eichten, "Theoretical Expectation at Collider Energies", FERMILAB-Conf-85/178-T (May, 1986).

[4] "CDF/UA2 Presentations on W/Z Physics at the 1991 Lepton-Photon Conference (Geneva)", D0 internal note D0-1170 (August, 1991).

[5] "A New Limit on the Mass of the Top Quark", presented by K. Sliwa at the XXVth Recontres de Moriond, Les Arcs, France, March 4-18,1990, Fermilab preprint, FERMILAB-Conf-90/93-E (May 1990).

[6] L. DiLella, "Jet Production in Hadronic Collisions", Ann. Rev. Nucl. Part. Sci. 35 (1985) 107-34.

[7] H.E. Fisk and J. Slaughter, eds., "Collider Physics at Fermilab in the 1990's", D0 internal note D0-934 (February 27, 1990).

[8] UA2 Collaboration, P. Bagnaia et al., Phys. Lett. B138 (1984) 430.
UA2 Collaboration, J.A. Appel et al., Phys. Lett. B160 (1985) 349.

[9] R.P. Feynman, Phys. Rev. Lett. 23 (1969) 1415-1417.

[10] M. Breidenbach et al., Phys. Rev. Lett. 23 (1969) 935.
W.K.H. Panofsky, Proc. 14th Int. Conf. on High Energy Phys., Vienna (CERN) (1968).

[11] S.L. Glashow, Nucl. Phys. 22 (1961) 579.
S. Weinberg, Phys. Rev. Lett. 19 (1967) 1264.
A. Salam, "Elementary Particle Theory", ed. N. Svartholm(Stockholm: Almqvist, Forlag A B) p. 367.

[12] UA1 Collaboration, G. Arnison et al., Phys. Lett. B122 (1983) 103.
UA2 Collaboration, M. Banner et al., Phys. Lett. B122 (1983) 476.
UA1 Collaboration, G. Arnison et al., Phys. Lett. B126 (1983) 398.
UA2 Collaboration, P. Bagnaia et al., Phys. Lett. B129 (1983) 130.

[13] A. Sirlin, Phys. Rev. D22 (1980) 971.

[14] P.W. Higgs, Phys. Lett. 12 (1964) 132; Phys. Lett. 13 (1964) 508; Phys. Rev. 145 (1966) 1156.

[15] D0 Design Report, The D0 Collaboration (1983, revised 1984, 1985) unpublished.

[16] Figure courtesy of A. Spadafora.

[17] P.D. Grannis, "The D0 Detector at the Fermilab Collider", D0 internal note D0-558 (May 20, 1987).

[18] P.D. Grannis, "Specifications for the D0 Detector", D0 internal note D0-560 (May 22, 1987).

[19] A. Zylberstein, "The Transition Radiation Detector for the D0 Experiment", Proceeding of the $\bar{p}p$ Workshop at Fermilab, 1988.

[20] A.R. Clark et al., "A High Precision Drift Chamber for D0", Nucl. Instr. Meth. A261 (1987) 420.

[21] B. Gobbi et al., D0 notes D0-265, D0-266, D0-267 (June - August, 1985).

[22] T. Behnke, "The Central Drift Chamber for the D0 Experiment: Design, Construction, and Test", Ph.D. Thesis, State University of New York at Stony Brook, Stony Brook, New York (August, 1989).

[23] C. Leroy, Y. Sirois, and R. Wigmans, Nucl. Instr. and Meth. A252 (1986) 4.

[24] R.C. Fernow, Introduction to Experimental Particle Physics, Cambridge University Press, 1986.

[25] W. Heitler, The Quantum Theory of Radiation, 3rd ed., Oxford: Clarendon Press, 1953.

[26] R. Wigmans, "Energy Loss of Particles in Dense Matter - Calorimetry", Lecture notes from the ICFA School of Instrumentation in Elementary Particle Physics, Trieste, Italy (June 8-19, 1987); Preprint from National Instituut Voor Kernfysica en Hoge-Energiefysica, NIKHEF-H/87-12 (August, 1987).

[27] R. Wigmans, "On the Energy Resolution of Uranium and Other Hadron Calorimeters", CERN preprint, CERN/EF 86-18 (September 26, 1986).

[28] G. Barbellini, "Calorimetry in Particle Physics", CERN preprint, CERN-EP/86-203 (November 28, 1986).

[29] M. Abolins, et al., "Hadron and Electron Response of Uranium/Liquid Argon Calorimeter Modules for the D0 Detector", Nucl. Instr. Meth. A280 (1989) 36-44.

[30] C. Fabjan, "Calorimetry in High Energy Physics", in T. Ferbel (ed.), Experimental Techniques in High Energy Phvsics, Addison-Wesley Publishing Company, Inc., 1987.

[31] B. Anders, U. Behrens, and H. Bruckmann, "On the Calculation of the Energy Loss of Muons in Sampling Calorimeters", Nucl. Instr. Meth. A270 (1988) 140-145.

[32] E. Bernardi et al., Nucl. Instr. Meth. A262 (1987) 229-42.

[33] C.W. Fabjan and R. Wigmans, Rep. Prog. Phys. 52 (1989) 1519.

[34] S. Hayakawa, Cosmic Ray Physics, John Wiley & Sons, Inc., 1969.

[35] M.S. Longair, High Energy Astrophysics, Cambridge University Press, 1981.

[36] N. Bohr, Philos. Mag 25 (1913) 10.
N. Bohr, Philos. Mag 30 (1915) 251.
N. Bohr, Phys. Rev. 59 270.
N. Bohr, Kgl. Danske Videnskab. Selskab. Mat-fys. Medd., XVIII, No. 8 (1948).
N. Bohr, Kgl. Danske Videnskab. Selskab. Mat-fys. Medd., XXIV, No. 19 (1948).

[37] H. Bethe, Ann. Physik 5, 325 (1930).
H. Bethe, Z. Phys. 76, 293 (1932).
H. Bethe, and J. Ashkin, in Experimental Nuclear Physics 1. ed. by E. Segre, Wiley, New York (1953).

[38] E. Fermi, Phys Rev. 57, 485 (1940).

[39] L. Landau, J. Phys USSR 8, 201 (1944).

[40] F. Bloch, Ann. Phys. (Leipzig) 16, 285 (1933).
F. Bloch, Z. Phys. 81, 363 (1933).

[41] J.D. Jackson, Classical Electrodynamics, 2nd ed., John Wiley & Sons, 1975.

[42] B. Rossi, High Energy Particles, Englewood Cliffs: Prentice-Hall, 1952.

[43] U. Fano, "Penetration of Protons, Alpha Particles, and Mesons", Ann. Rev. Nucl. Part. Sci. 13 (1963) 1-66.

[44] S. Ahlen, "Theoretical and Experimental Aspects of the Energy Loss of Relativistic Heavily Ionizing Particles", Rev. Mod. Phys. 52 (1980) 121-73.

[45] K. Symon, "Fluctuations in Energy Loss by High Energy Charged Particles in Passing Through Matter", Ph.D. thesis, Harvard University, Cambridge, Mass. (1948).

[46] R. Sternheimer, Phys. Rev. 88 (1952) 851-9.
R. Sternheimer, Phys. Rev. 103 (1956) 511.
R. Sternheimer, M.J. Berger, and S.M. Seltzer, Atomic Data and Nuclear Data Tables 30 (1984) 261-71.

[47] W. Lohmann, R. Kopp and R. Voss, "Energy Loss of Muons in the Energy Range 1-10000 GeV", CERN preprint, CERN 85-03 (March 21, 1985).

[48] R. Sternheimer, S.M. Seltzer, and M.J. Berger, Phys. Rev. B26 (1982) 6067-76; erratum, B27 (1983) 6971.

[49] P.V. Vavilov, Zh. Eksp. Teor. Fiz. 32, 920 [Sov. - Phys. JETP 5 (1957) 749].

[50] C. Tschalar, Ph.D. Thesis, University of Southern California, Los Angeles, California (1967).
C. Tschalar. Nucl. Instr. Methods 61 (1968) 141.
C. Tschalar, Nucl. Instr. Methods 64 (1968) 237.

[51] R. Talman, Nucl. Instr. Methods A59 (1979) 189-211.

[52] H. Maccabee and D. Papworth, "Correction to Landau's Energy Loss Formula", Phys. Lett. A30 (1969) 241-2.

[53] Peter M. Joseph, "Range Energy Tables for High Energy Muons", Cornell University Note CLNS-52 (May, 1969).

[54] A.H. Walenta et al., Nucl. Instr. Meth. 161 (1979) 45-58.

[55] P. Franzini, "Performance of the D0 Uranium-Liquid Argon Calorimeter Modules", Nucl. Instr. Meth. A289 (1990) 438-445.

[56] P. Franzini, "Estimate of the Uranium Noise in the D0 Calorimeter", D0 internal note D0-217 (1985).

[57] P. Franzini, "Noise and Pileup in Sampling Calorimeters", D0 internal note D0-263 (September 28, 1987).

[58] J. Sculli, Transparencies from Talk on 5000 Channel Test, D0 Collaboration Meeting (February, 1990), D0 internal note D0-937 (February 16, 1990).

[59] K. Kleinknecht, Detectors for Particle Radiation, Cambridge University Press, 1986.

[60] T. Doke, "Fundamental Properties of Liquid Argon, Krypton, and Xenon as Radiation Detector Media", in T. Ferbel (ed.), Experimental Techniques in High Energy Physics, Addison-Wesley Publishing Company, Inc., 1987.

[61] W.J. Willis and V. Radeka, "Liquid-Argon Ionization Chambers as Total Absorption Detectors", Nucl. Instr. Meth. 120 (1974) 221-236.

[62] P. Franzini, "Considerations Concerning Coherent and Random Noise in the D0 Calorimeter", D0 internal note D0-471 (October 24, 1986).

[63] D. Norman, "Cosmic Muons in the D0 Detector: Flux Calculations Through Various Fiducial Volumes", D0 internal note D0-856 (June 12, 1989).

[64] Figure courtesy of M. Fatyga

[65] Figure courtesy of S. Feher.

[66] W. Hoffmann et al., Nucl. Instr. Meth 135 (1976) 151-156.

[67] G.C. Blazey, private communication.

[68] A. Dar, "Cosmic Ray Muons at Ground Level and Deep Underground", Preprint from Technion-Israel Institute of Technology, TECHNION-PHYS-84-41.

[69] J. Kourlas and J. Sculli, "Comparison of Pulser and Calibration Signals in the D0 Electronics", D0 internal note D0-936 (February 26, 1990).

[70] Particle Properties Data Booklet, April 1986.

[71] Thomas K. Gaisser, Cosmic Rays and Particle Physics, Cambridge University Press, 1990.

DATE
FILMED
5/16/94
END